The
University
Of
Sheffield.

Structure-property relations in Sodium-Bismuth Titanate related materials

by

Emilio Pradal Velázquez

A thesis submitted for the degree of
Doctor of Philosophy

Supervisors: Prof. Derek C. Sinclair
Prof. Ian M. Reaney

The University of Sheffield
Faculty of Engineering
Department of Materials Science and Engineering

April 2019

Acknowledgements

I wish to express my gratitude:

To Professor Derek Sinclair for his admirable kindness, guidance, teaching and dedication.

To Dr. Fan Yang for her endless patience, friendliness, support and advice.

To Dr. Patrick Wu and Dr. Linhao Li for the valuable input, discussions and humour.

To Professor Ian Reaney for his astonishing insight into the structure of these materials.

To Mr. Andrew Mould for his advice and training.

To the functional materials and devices group for the warm and welcoming ambience, the help when needed and the beers (needed or not).

A mis amigos, cuyo alentador interés y proclividad a hacerme pensar en otros temas me ayudan a disfrutar lo que hago.

A mi familia, con todo cariño, por todo lo que me han enseñado y apoyado para tener y alcanzar sueños.

I also wish to thank CONACYT for the scholarship (Becas CONACYT al extranjero registro 327115) that allowed me to take on my postgraduate studies.

Experiments at the ISIS Neutron and Muon Source were supported by beamtime allocations RB1720168 (DOI: 10.5286/ISIS.E.RB1720168) and RB1800099 (DOI: 10.5286/ISIS.E.RB1800099) from the Science and Technology Facilities Council.

Abstract

The electrical properties of the ferroelectric perovskite $Na_{0.5}Bi_{0.5}TiO_3$ (NBT) are sensitive to low levels of Na and Bi non-stoichiometry. Previous work established that NBT can possess high oxide-ion conduction which makes it a potential electrolyte for solid oxide fuel cells or it can be electrically insulating making it useful as a dielectric material for high temperature capacitor or Pb-free piezoelectric applications. Although acceptor-doping on the A- or B-site can create oxygen deficiency in the NBT lattice, the increase in oxide-ion conductivity has been modest. The limited solid solutions for single dopants and structural complexity of NBT have hindered the understanding of the origin of its high ionic conductivity. As a consequence, the study of NBT with other perovskites, which have shown higher solid solution limits with NBT, is of interest to obtain more information on the behaviour of this challenging system.

In this work, solid solutions of NBT with $BiMg_{2/3}Nb_{1/3}O_3$ (BMN), $BiZn_{2/3}Nb_{1/3}O_3$ (BZN) and $NaNbO_3$ (NN) are explored. In both the NBT-BMN and NBT-BZN cases there is little effect on the permittivity profiles and a gradual decrease in bulk (oxide-ion) conductivity until the system becomes insulating at ~ 6 mol% BMN and 4 mol% BZN. NBT-BMN has a solid solution limit between 7 and 8 mol% and the conductivity behaviour is similar to that reported in the literature for NBT-$BiAlO_3$ and explained as trapping of oxygen vacancies by the B-site dopant. For the NBT-BZN system, the solid solution limit is below 4 mol%, making it inconclusive whether the same trapping mechanism occurs in NBT-BZN.

NBT-NN forms an extensive solid solution with the limit exceeding 30 mol% NN. Laboratory XRD and variable temperature neutron diffraction results indicate stabilisation of the orthorhombic polymorph to lower temperatures with increasing NN content. Similar to NBT, the bulk conductivity of NBT-NN compositions display a strong dependence on small variations in the nominal Na and Bi content in the starting composition. It has previously been reported that this system produces permittivity-temperature profiles with remarkable stability. In this work, data extracted from impedance spectroscopy are compared against data from fixed frequency permittivity measurements and demonstrate that the attractive flattening of the permittivity profiles at 1 MHz involves a mixed response from more than one electro-active element. Powder and ceramic processing conditions are shown to have a strong influence on the electrical properties, impacting upon the reproducibility of these materials and raising concerns about their applicability. The electrical heterogeneity in these samples is sensitive to sample history and in conductive samples can dominate the conductivity at high

temperatures (>600 °C), leading to unreliable measurements of oxide-ion transport numbers normally associated with a bulk response.

Finally, a previously reported but relatively unstudied Sodium-Bismuth Titanate Pyrochlore solid solution (Pss) is explored; however, it forms via an entirely different mechanism from that originally reported. In both cases, A-site vacancies are involved, similar to that reported for undoped Bismuth Titanate Pyrochlore. In contrast to Bismuth Titanate Pyrochlore, this Pss can be prepared and ceramics sintered using conventional methods; however, the processing remains challenging. Although many processing issues are addressed here and a method developed to obtain dense and phase-pure Pss ceramics, other potential issues occur such as redox activity which makes control of the pO_2 an important processing parameter when preparing and characterising Pss materials. This cubic Pss has low electrical conductivity (and does not exhibit any evidence of oxide-ion conduction), a broad permittivity maximum of ~100 near room temperature and exhibits relaxor ferroelectric behaviour. Variable temperature neutron diffraction data does not provide any conclusive evidence for a phase transition in the Pss between 4.2 and 873.2 K.

Contents

List of Figures

List of Tables

Chapter 1

Introduction

The $Na_{0.5}Bi_{0.5}TiO_3$ perovskite (NBT), mainly as a parent compound in solid solutions, is of technological interest due to its potential application as a lead-free piezoelectric or high temperature dielectric [1, 2, 3]. It is also of interest due to its unusual polymorphism involving phase coexistence and its complex disordered structure consisting of various local octahedral tilting schemes [4, 5]. Furthermore it can present remarkably high oxide-ion conductivity that is extremely sensitive to small changes in composition and occurs with a very low nominal concentration of oxygen vacancies ($0.1 \sim 0.5\%$ of the available sites), which implies a very high mobility [6, 7]. If the origin of the high mobility of oxide ions in NBT can be understood, it will be valuable knowledge to optimise the properties of this and other materials as well as help guide the design of new oxide ion conductors.

The complex structure and polymorphism of NBT have strongly hindered acquiring a fundamental understanding of its high oxide-ion conduction [8]. Several acceptors (i.e. Sr^{2+}, Mg^{2+}, Zn^{2+}, Ga^{3+}) have been doped into NBT seeking to optimise its ionic conductivity but this has resulted in relatively small improvements at best [7, 9]. NBT tolerates small amounts of most single acceptor dopants (< 5at%), although solid solutions with other perovskites such as $BaTiO_3$, $NaNbO_3$ and $BiZn_{0.5}Ti_{0.5}O_3$ have been reported with higher solid solution limits in the literature focused on its potential applications as a ferroelectric [1, 10, 11, 12, 13]. To date, there is limited information in the literature on the ionic conduction of these systems. It is of particular interest to explore those where the Na/Bi ratio changes as it has been found to impact the electrical behaviour of NBT [14].

This work aims to provide more information on how the oxide-ion conduction behaves in NBT to help understand it. To achieve this, the structure and electrical properties (including the bulk conductivity obtained from impedance spectroscopy) of NBT-based solid solutions with two Bi-based perovskites and with $NaNbO_3$ are studied. Additionally, in order to compare with a similar composition but different structure, a pyrochlore solid solution in the $Na_2O{\cdot}Bi_2O_3{\cdot}TiO_2$ system is characterised.

Chapters 2 and 3 provide the background for this work, Chapter 2 consists of a review of the literature on NBT and its potential applications and Chapter 3 briefly describes the techniques used in this work. In Chapter 4 the electrical properties of solid solutions between NBT and $BiMg_{2/3}Nb_{1/3}O_3$ or $BiZn_{2/3}Nb_{1/3}O_3$ are explored. Similarly, Chapter 5 deals with the effect of $NaNbO_3$ on NBT, considering the options of solid solutions based on stoichiometric, Bi-deficient or Bi-rich NBT. The electrical properties of a pyrochlore solid solution that had been previously reported to exist but not studied further are investigated in Chapter 6. Finally, Chapter 7 presents conclusions to this work and discusses future work to complement what is presented here.

Chapter 2

Literature review

2.1 The $Na_{0.5}Bi_{0.5}TiO_3$ (NBT) perovskite

The $Na_{0.5}Bi_{0.5}TiO_3$ perovskite (NBT) is a ferroelectric material that has been intensely studied as a promising lead-free piezoelectric and high temperature dielectric. This perovskite was first reported in 1960 by Smolenskii *et al.* [15] but interest in it has increased recently due to the legislative restrictions arising from health and environmental concerns about the use of lead in piezoelectrics. An ideal cubic perovskite is represented in Figure 2.1. This structure consists of a *fcc* arrangement of AX_3 close-packed layers with the B ions sitting in the octahedral sites that are not adjacent to an A ion. NBT is an oxide with titanium ions occupying the B-sites and sodium and bismuth ions sharing the A-sites with an essentially random distribution [5].

Using Rietveld refinements of neutron diffraction data collected from calcined powders, Jones and Thomas report that NBT is cubic ($Pm\bar{3}m$) at temperatures higher than 540 °C, tetragonal ($P4bm$) from 540 to 400 °C, with tetragonal and rhombohedral ($R3c$) structures coexisting between 400 and 255 °C and the rhombohedral polymorph being the stable low temperature structure [4]. Dorcet *et al.* used electron diffraction and imaging on a transmission electron microscope (TEM) to explore the polymorphism of NBT and concluded that the rhombohedral ($R3c$) phase destabilises from 200 °C when sheets of an orthorhombic ($Pnma$) phase appear as twin boundaries between the $R3c$ blocks giving rise to a modulated phase. The fraction of orthorhombic sheets increases with temperature until all the material becomes orthorhombic around 280 °C. Heating the orthorhombic phase decreases the displacement of the A-site ions and the magnitude of antiphase tilting leading to a phase transformation around 320 °C to a tetragonal ($P4/mbm$) polymorph. They remark that they can detect nanodomains of A-site ordered $P4_2/mnm$ above 400 °C. Finally, the tetragonal phase becomes cubic around 520 °C although it might retain small regions of the tetragonal phase [17, 18]. It is unclear if the low temperature polymorph is rhombohedral ($R3c$) or monoclinic (Cc), although most recent studies tend to support the monoclinic (Cc) structure [19], even if just as an ”average best fit”

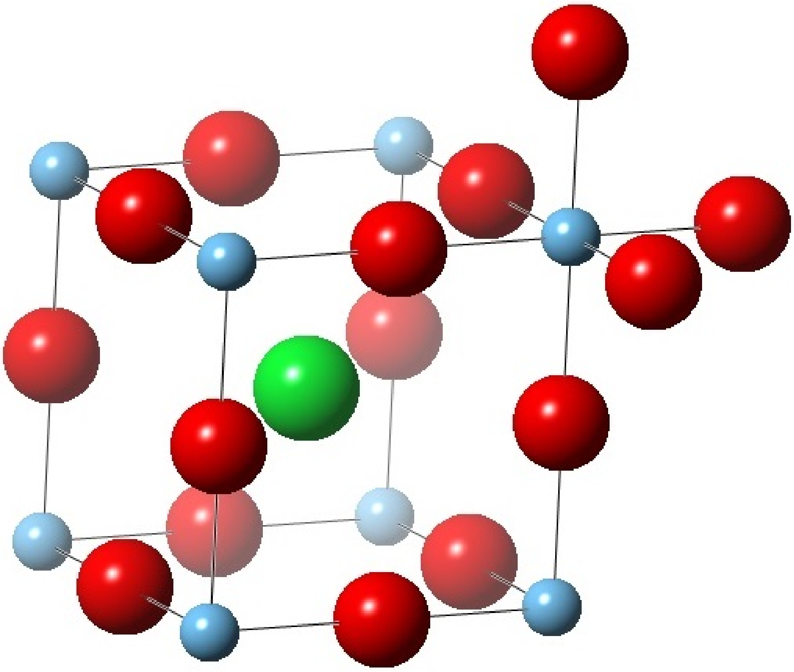

Figure 2.1: Ideal cubic perovskite ABX_3. A cations in green, B cations in blue and X anions in red.

since the local structure is remarkably complex [5]. The titanium ions are displaced from the centre of the octahedra, and because of the lone pair effect the bismuth ions are displaced on the A-sites [20]. This gives rise to the ferroelectricity observed in this material. The octahedral tiltings observed for NBT are complex; at room temperature, along one of the orthogonal axes the tilting is in-phase ($a^-a^-c^+$) for a few cells, but at long range an average anti-phase tiliting ($a^-a^-c^-$) is observed [5]. It is considered that the disordered tilting leads to the existence of polar nanoregions responsible for the relaxor behaviour of the material [21]. For NBT a permittivity peak is observed near 320 °C with a relative permittivity of $\sim$ 2800 to 3200 [22]. This makes it promising for high temperature dielectric applications such as capacitors operating near engines.

Ferroelectricity arises from the long range alignment of permanent electric dipoles in the same direction. The direction of these dipoles can be switched if a strong enough field is applied and will remain aligned in the direction the field was applied even after it is removed. This leads to a remnant polarisation that can be observed macroscopically. The possibility of switching the direction of the dipoles also provides ferroelectric materials with extremely high dielectric constants (two or three orders of magnitude higher than ”normal” dielectrics). Another remarkable feature of the permittivity in ferroelectrics is its strong temperature dependence: it increases dramatically around a specific temperature T_C for the material (its Curie temperature) at which a phase transition occurs between a high temperature centrosymmetric structure where all the dipoles are disordered (paraelectric state) and a low temperature non-centrosymmetric structure where the dipoles can order and align (ferroelectric state). Other peaks in permittivity may also occur below T_C (associated with other polymorphic transformations at lower temperatures), although they are not as large. In ”ordinary” ferroelectrics the alignment of the dipoles can span hundreds of unit cells within a grain, forming ferroelectric domains (regions where the dipoles are aligned in the same direction) and the paraelectric to ferroelectric phase transition is characterised by a sharp peak in the temperature profile of the permittivity.

There exist several materials, known as relaxor ferroelectrics or relaxors, where local differences in structure prevent the alignment of dipoles to be long ranged and lead to slightly different electrical behaviour from different regions. In these cases the alignment spans a few cells and forms polar nanoregions which, as the name indicates, are small compared to ferroelectric domains. Unlike ”ordinary” ferroelectrics, relaxors exhibit (as a result of the local differences in structure) broad peaks in the permittivity as a function of temperature and dependence of the dielectric response with the frequency of the alternating voltage. In these materials the permittivity drops with increasing frequency and the dielectric loss increases whereas the temperature at which the peak(s) occur shifts with frequency. The broadening of the permittivity peak provides temperature stability, making relaxor ferroelectrics of significant interest for capacitors [23].

2.2 Bi_2O_3-Na_2O-TiO_2 Phase diagram

Currently only a partial phase diagram for the Bi_2O_3-Na_2O-TiO_2 system has been reported. The work (Reference [24]) was done in 1978 by Uchida and Kikuchi, who studied the sub-solidus equilibria in the TiO_2-rich area, Figure 2.2 reproduces their diagram. A pyrochlore solid solution ($x\mathrm{Na_2O} \bullet 25\,\mathrm{Bi_2O_3} \bullet (75-x)\mathrm{TiO_2}$ with $2.50 < x < 3.75$) and two ternary compounds, $Na_{0.5}Bi_{8.5}Ti_7O_{27}$ and $NaBiTi_6O_{14}$, were first reported in that work, $NaBiTi_6O_{14}$ lies along the NBT-TiO_2 tie line and was found to decompose at 1100 °C. On the $Bi_2O_3-TiO_2$ phase diagram, more binary compounds have been reported than those considered by Uchida and Kikuchi as seen in Figure 2.3 [25], which shows a $Bi_2Ti_2O_7$ pyrochlore with a composition within the region studied by Uchida and Kikuchi, and Bi_8TiO_{14} at the Bi_2O_3-rich end.

The $Bi_2O_3-TiO_2$ system has been widely and intensely studied because bismuth titanates exhibit useful optical and electrical properties. There has been strong debate on the number and exact compositions of many bismuth titanates since Speranskaya *et al.* made the first comprehensive investigation of the system in 1965. After a careful review of the literature and some additional experiments Kargin *et al.* conclude that of nearly ten different compounds that have been reported, only four have been undoubtedly determined to exist and to be equilibrium phases: $Bi_2Ti_4O_{11}$, $Bi_4Ti_3O_{12}$, $Bi_2Ti_2O_7$ and $Bi_{12}TiO_{20}$. The actual compositions of the last two are still subject to discussion [26], the corrected phase diagram is reproduced in Figure 2.4. Some of the other bismuth titanates, for example Bi_8TiO_{14}, are commonly accepted to exist as metastable phases and have been paid less attention.

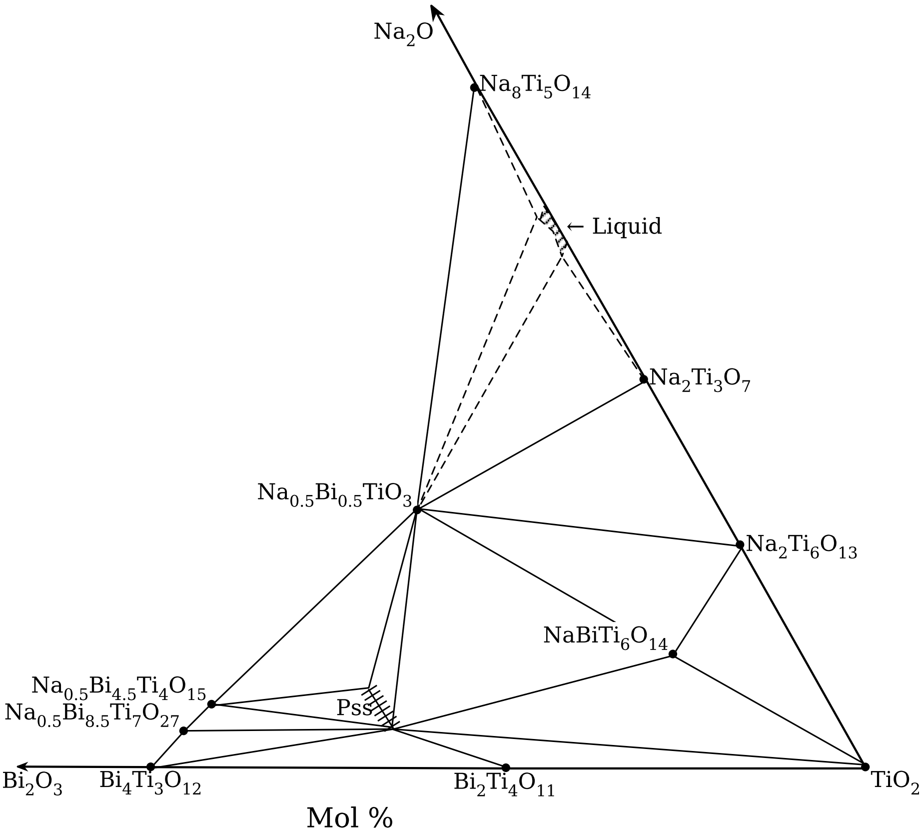

Figure 2.2: $Na_2O-Bi_2O_3-TiO_2$ Equilibrium relations at 1000°C. *Pss* stands for Pyrochlore solid solution. Adapted from Uchida and Kikuchi, *Subsolidus Phase Equilibria in the System Na_2O-Bi_2O_3-TiO_2 at 1000* °C, J. Am. Ceram. Soc., **61**, 58 (1978) with permission from John Wiley and Sons.

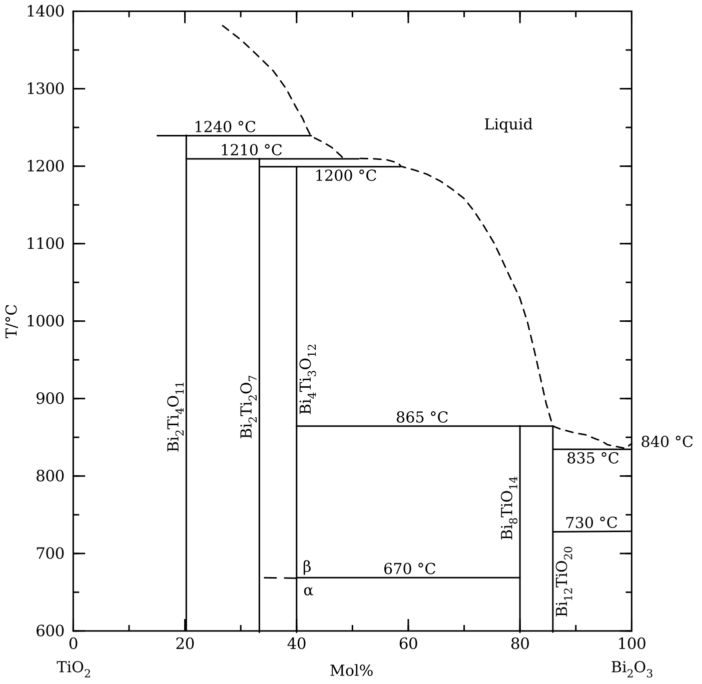

Figure 2.3: $Bi_2O_3-TiO_2$ phase diagram reported by Masuda *et al.* [25]. Reproduced with permission. © (1992) The Physical Society of Japan and The Japan Society of Applied Physics

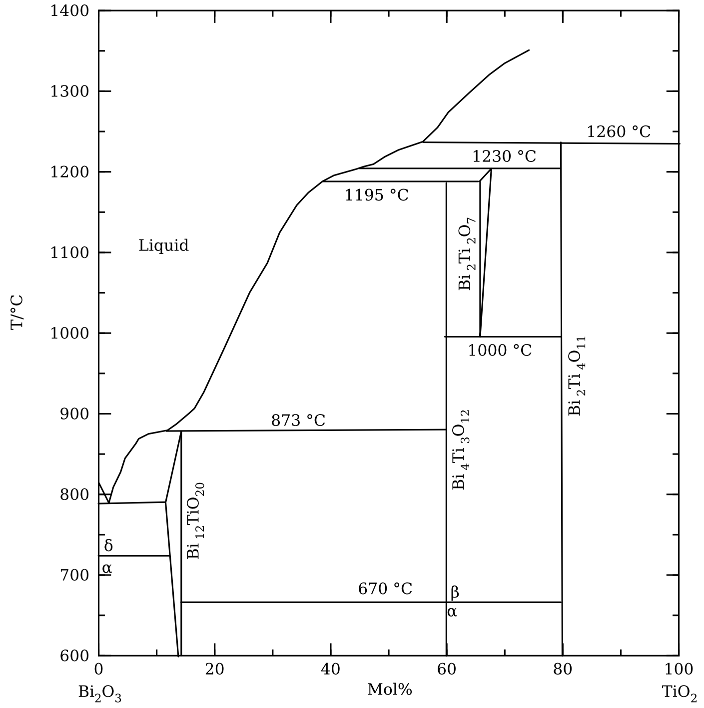

Figure 2.4: $Bi_2O_3-TiO_2$ phase diagram reported by Kargin *et al.*. Reprinted by permission from Springer Nature: Russian Journal of Inorganic Chemistry, 2015, **60** [5], 619625, *Phase Relations in the $Bi_2O_3TiO_2$ System*, Kargin *et al.*), © Pleiades Publishing, Ltd., 2015.

2.3 NBT based ferroelectrics and dielectrics

Several solid solutions of NBT with other perovskites such as $BaTiO_3$, $KNbO_3$, $K_{1/2}Bi_{1/2}TiO_3$, $NaNbO_3$ and $BiZn_{1/2}Ti_{1/2}O_3$ have received wide attention for their dielectric as well as piezoelectric properties since some of these systems exhibit a morphotropic phase boundary [1, 10, 11, 12, 13]. Undoped NBT piezoelectrics have a d_{33} piezoelectric coefficient close to 100 $\mathrm{pC/N}$ [2], however they present high coercive fields that make the poling process difficult for applications. Additionally, NBT shows high leakage (i.e. $tan\delta > 0.05$) further limiting its applicability [27]. For NBT-based solid solutions, piezoelectric coefficients between 150 and 200 $\mathrm{pC/N}$ [1] have been achieved, the best so far are solid solutions with $BaTiO_3$.

To date, the performance of NBT piezoelectrics remains far inferior to that of commercially used materials based on lead zirconate-titanate (PZT) which typically have d_{33} values close to 500 $\mathrm{pC/N}$ [2]. Despite their inferior performance, NBT piezoelectrics receive intense research efforts due to the environmental and health concerns that surround the use of PbO, especially during manufacture and at the end of life of the devices, which are driving regulatory organisations to impose limits on the use of PbO, making the improvement of lead-free piezoelectrics an essential technological issue [1, 2]. However, life cycle analysis has shown that although the fabrication of NBT piezoelectrics is predicted to have lower environmental impact than that of PZT piezoelectrics, the extraction and refinement of Bi_2O_3 consume more energy than those of PbO, it should also be taken into account that most of the Bi_2O_3 is currently produced as a by-product of PbO and bismuth-based ceramics are more difficult to recycle [28]. Another attractive feature of NBT-based piezoelecrics is that NBT has a significantly higher fracture toughness than most other ferroelectrics, which allows for longer lifetimes of devices such as actuators [29].

Solid solutions with NBT are amongst the main options considered for high temperature capacitor applications (>200 °C) due to wide temperature ranges of stable relative permittivity up to $\sim$2000, but they tend to have narrower windows with a suitable dielectric loss ($tan\delta \leq 0.02$) [3]. Jo *et al.* studied an NBT-6 mol% $BaTiO_3$ composition and concluded, from X-ray and electron diffraction, that at room temperature the material consists of a cubic matrix with $R3c$ and $P4bm$ polar nanoregions. They also suggested the dielectric response consists of two anomalies (see Figure 2.5), the one at lower temperatures corresponding to the relaxor contribution of both $R3c$ and $P4bm$ polar nanoregions (which they can estimate with phenomenological models) and the one at higher temperatures which they deconvolute into two contributions: one they attribute to an $R3c$-$P4bm$ phase transition and another associated with $P4bm$ polar nanoregions [30]. The properties of NBT show very high sensitivity to small deviations in stoichiometry, which implies the processing history is critical for these materials, which has

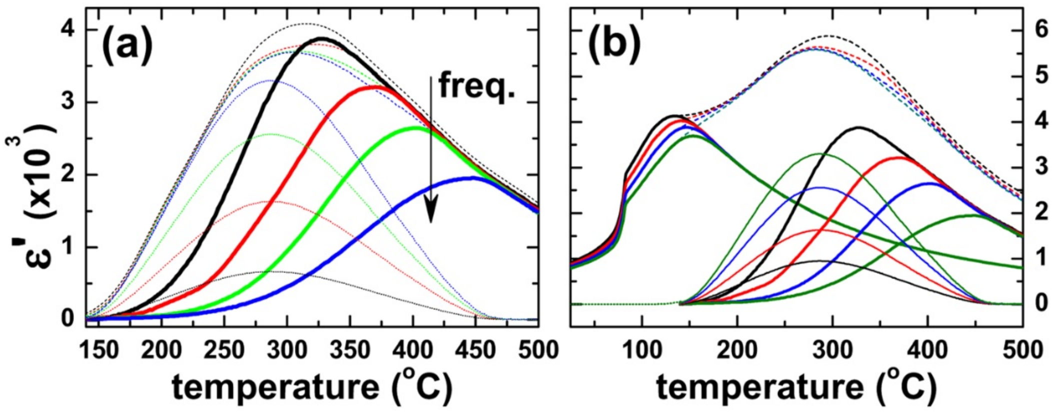

Figure 2.5: Deconvolution of the permittivity-temperature profile (total response ploted as dashed lines) of NBT-6 mol% $BaTiO_3$ suggested by Jo *et al.* (a) Deconvolution of the high temperature anomaly into the contribution from the $R3c$-$P4bm$ phase transition (fine dotted lines) and the frequency dispersive contribution from the $P4bm$ polar nanoregions (solid lines). (b) Summary of the deconvolution for poled NBT-6 mol% $BaTiO_3$. Reprinted from Jo *et al.*, J. Appl. Phys. **110**, 074106 (2011), with the permission of AIP Publishing. © 2011 American Institute of Physics.

in turn hindered their application as ferroelectrics [31, 32]. One of the clearest problems is the volatilisation of Bi_2O_3 during sintering, which results in the presence of oxygen vacancies (Equation 2.1) that are mobile and may pin domain walls giving rise to the high coercive fields and leakage currents that hinder the application of NBT as a piezoelectric or dielectric.

$$2\,\mathrm{Bi}_{\mathrm{Bi}}^{\times} + 3\,\mathrm{O}_{\mathrm{O}}^{\times} \longrightarrow 2\,\mathrm{V}_{\mathrm{Bi}}^{'''} + 3\,\mathrm{V}_{\mathrm{O}}^{\bullet\bullet} + \mathrm{Bi_2O_3}\uparrow \qquad (2.1)$$

Soft processing routes (e.g. wet chemical synthesis) have been shown to produce better NBT piezoelectrics than those made through conventional solid state reactions [33, 34]. This can be expected since the soft processing enables sintering at lower temperatures and a finer control of the composition. Using solid state synthesis, better piezoelectrics have been obtained by adding excess Bi_2O_3 or doping with a donor on the titanium site. These samples can be poled easily and present low dielectric losses [31]. An excess of Bi_2O_3 compensates for the losses during processing, and donor-doping fills in the oxygen vacancies that are generated.

NBT tolerates A-site non-stoichiometry, which can dramatically alter its electrical behaviour; Na_2O deficiency can be assumed to introduce oxygen vacancies and be detrimental for the piezoelectric and dielectric performance. However, the observed behaviour is the opposite. Sodium-deficient compositions show better performance as piezoelectrics and dielectrics, a possible explanation offered by Sung *et al.* is that sodium vacancies and oxygen vacancies may gather and concentrate at the grain boundaries forming neutral clusters that do not impede the motion of domain walls [37]; on the other hand, for bismuth-deficient compositions such neutral clusters would be composed of five defects $(2\,V_{Bi}''' + 3\,V_{O}^{\bullet\bullet})^{\times}$, which is much less likely to occur and the vacancies remain mobile [32].

2.4 Oxide ion conduction in NBT

Although several authors had determined that the volatilisation of Bi_2O_3 is responsible for the presence of mobile oxygen vacancies in NBT samples with lower resistivities [31, 32, 38], they did not investigate in depth the potential of long range migration of the oxide ions as the cause of the high conductivity. NBT has been found to be a remarkably efficient electrolyte; the high polarisability of the bismuth ions and the weak Bi−O bonds are thought to be key aspects allowing such efficient diffusion through the lattice [39]. In the work by Li *et al.* it is confirmed that donor doping and bismuth-rich compositions produce insulating samples with better dielectric and piezoelectric performance [6] (see Figures 2.6 and 2.7). Scanning electron microscopy (SEM) enabled the observation of small amounts of $Na_2Ti_6O_{13}$ in $Na_{0.5}Bi_{0.49}TiO_{2.985}$ (NB49T) as would be expected from the phase diagram; for $Na_{0.5}Bi_{0.51}TiO_{3+\delta}$ (NB51T) small amounts of Bi_2O_3 were detected, although the phase diagram would predict a bismuth titanate.

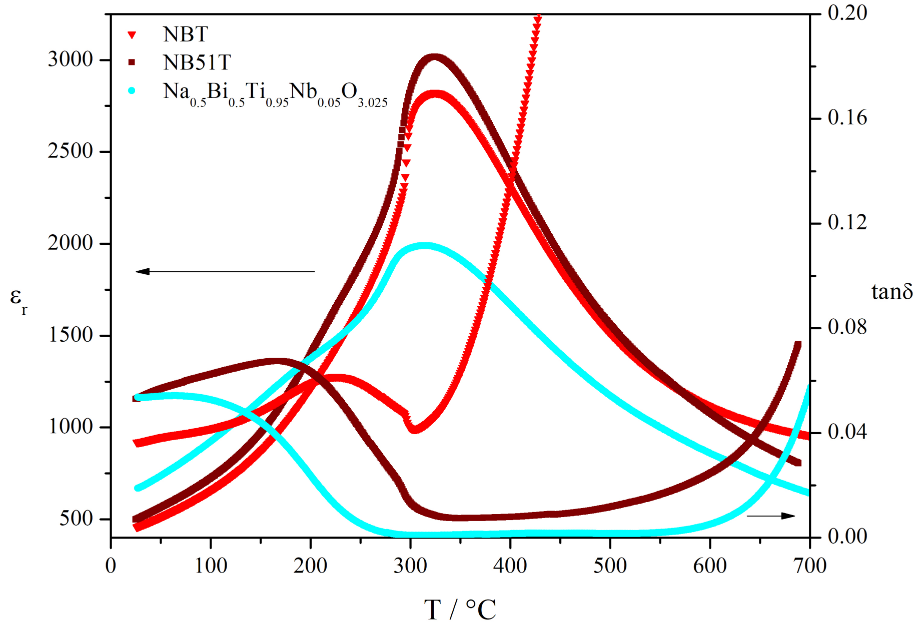

Figure 2.6: Temperature profiles of permittivity and dielectric loss at 1MHz of three NBT-based compositions. After L. Li [8].

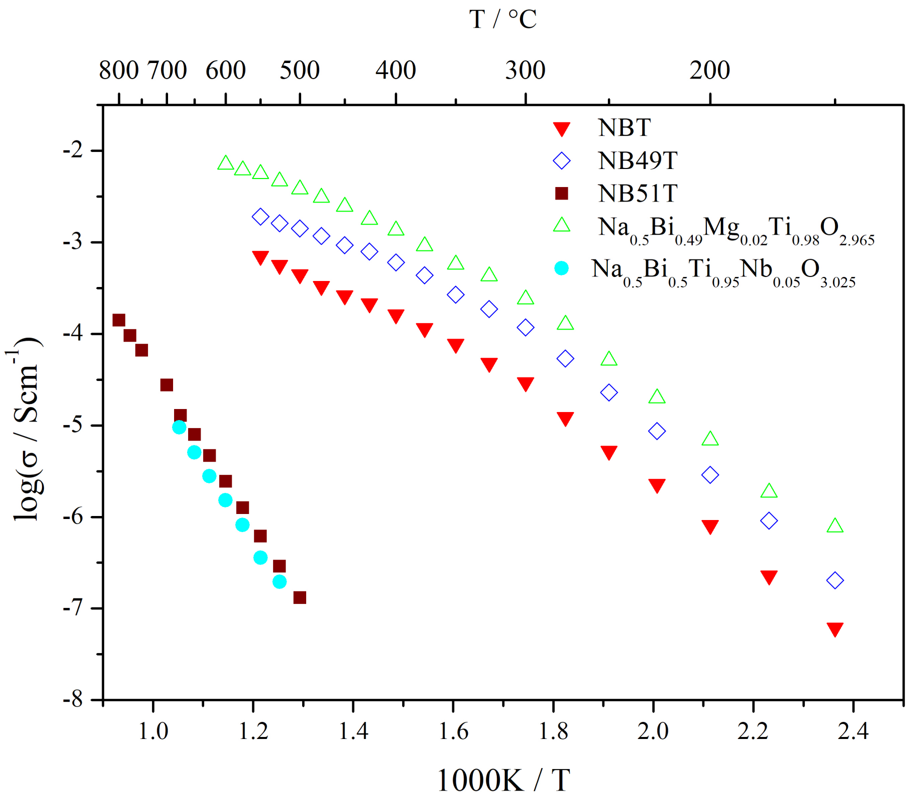

Figure 2.7: Arrhenius plot of bulk conductivity for five different NBT-based compositions. After M. Li *et al.* [6] and L. Li *et al.* [40].

Further investigations by Li *et al.* on the effect of sodium non-stoichiometry on the conductivity of NBT confirm that Na-rich nominal compositions form conductive samples and Na_2O deficiency results in insulating samples. In contrast to the effect of Bi non-stoichiometry which is understood from Equation 2.1, the effects of Na non-stoichiometry seem counterintuitive under the same logic. The experimental observations regarding sodium excess and deficiency become clear when small amounts of secondary phases detectable in SEM are taken into account, giving a more satisfying explanation than the one provided by Sung *et al.* [37]. Excess Na_2O results in a Na-rich secondary phase (Uchida and Kikuchi's phase diagram predicts $Na_8Ti_5O_{14}$) that leaves a Bi-deficient NBT as the main phase; for nominally Na-deficient compositions the secondary phase is TiO_2, therefore the perovskite will be nearly stoichiometric and insulating. The authors advise that the Bi/Na ratio in the starting composition will determine the electrical behaviour of the material: if the ratio is larger than one, insulating NBT will be obtained, while conducting NBT results from starting ratios equal to or less than one [39].

Since the charge carriers in NBT are predominantly oxygen vacancies, increasing the concentration of vacancies should improve the conductivity; substitution of the Ti^{4+} ions by Mg^{2+} increases the conductivity and expands the electrolyte domain to more reducing environments

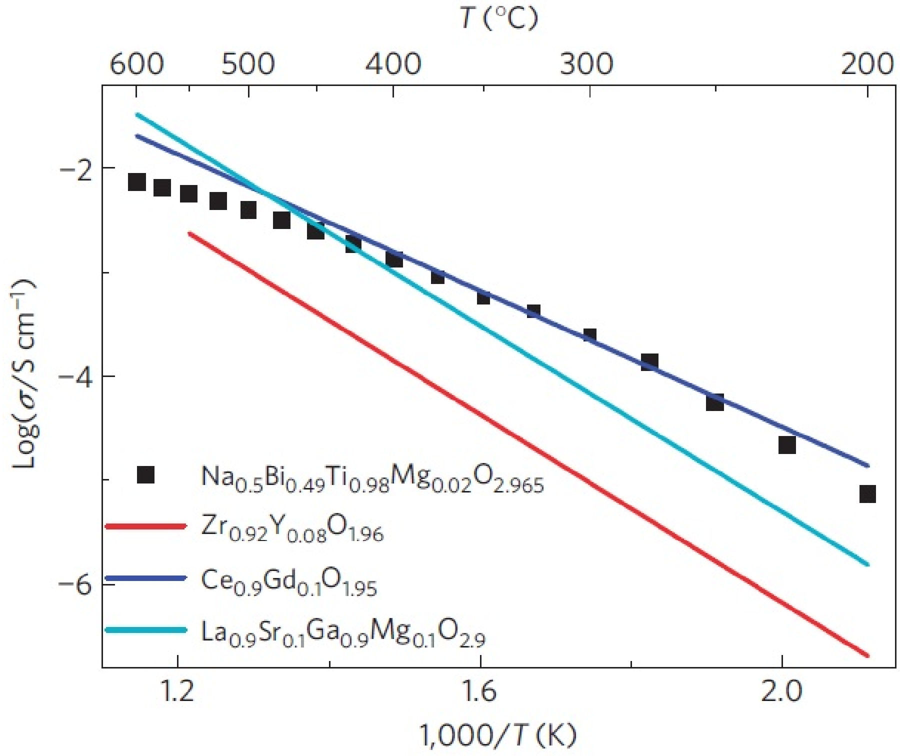

Figure 2.8: Comparison of the bulk conductivity of nominal composition $Na_{0.5}Bi_{0.49}Mg_{0.02}Ti_{0.98}O_{2.965}$ against well known oxide ion conductors between 200 and 600 °C. Reprinted by permission from Springer Nature: Nature Materials, **13**, 3135 (2014), *A family of oxide ion conductors based on the ferroelectric perovskite* $Na_{0.5}Bi_{0.5}TiO_3$, Li *et al.*, © Macmillan Publishers Limited, 2013.

[6]. In contrast, donor-doping as presented in Equation 2.2 can fill the oxygen vacancies as Li *et al.* show is the case with Nb-doping on the B-site which requires around 2 at% Nb to turn the system into an insulator [40]. As shown in Equation 2.3 acceptor-doping NBT increases the concentration of oxygen vacancies and is a sensible strategy to optimise its ionic conductivity and could lead to new applications for this material. Figure 2.7 shows the bulk conductivities of nominally stoichiometric NBT, NB51T and NB49T, as well as Mg-doped NB49T and Nb-doped NBT. In Figure 2.8 it can be appreciated that the oxide ion conduction in Mg-doped NBT is comparable (even superior at low temperatures) to some of the most used oxide ion conductors like yttria-stabilised zirconia (YSZ) [6].

$$2\,Ti_{Ti}^{\times} + V_{O}^{\bullet\bullet} + 4\,O_{O}^{\times} + Nb_2O_5 \longrightarrow 2\,Nb_{Ti}^{\bullet} + 5\,O_{O}^{\times} + 2\,TiO_2 \tag{2.2}$$

$$Ti_{Ti}^{\times} + 2\,O_{O}^{\times} + MgO \longrightarrow Mg_{Ti}'' + O_{O}^{\times} + V_{O}^{\bullet\bullet} + TiO_2 \tag{2.3}$$

He and Mo [42] studied the conduction in NBT through density functional theory (DFT) calculations. First they explored the A-site disorder of the material and obtained results that support the experimental observations. Later they analyse the possibility of long range oxide diffusion in $Na_{0.5}Bi_{0.5}Mg_{0.04}Ti_{0.96}O_{2.96}$ with molecular dynamics simulations within the frame of DFT, and also obtained results in good agreement with the experiments shown by Li *et al.* [6]. More interestingly they show the importance of the local environment for the migration of the oxide ions; as shown by Saiful Islam [43] oxide ions in perovskites migrate to an adjacent vacant site following the edge of the BX_6 octahedra (see Figure 2.9), the configuration of maximum energy along this path (a saddle point in the potential energy surface) corresponds to the point where the oxide ion is in the plane of an A-A-B triangle. He and Mo determined there are dramatic differences in the activation energy for different configurations of NBT. The Bi-Bi-Ti planes have the lowest barriers (0.22 eV), the Na-Bi-Ti planes give barriers of 0.6 to 0.85 eV and the Na-Na-Ti path has a barrier between 1.0 and 1.3 eV. This trend is to be expected given the high polarisability of the bismuth ions. Their simulations show oxide ions passing only through the Bi-Bi-Ti and the Na-Bi-Ti triangles, which means that passage through Na-Bi-Ti saddle points is the rate limiting step for ionic conduction.

He and Mo also studied several ”possible” acceptors to dope on the A-site or B-site and improve the ionic conductivity of NBT. Some of these ”possible” dopants seem unfeasible like V^{2+} (which is an uncommon oxidation state for vanadium in solid oxides), a few would be highly undesirable to handle experimentally and would certainly not be used for any real application of the material (Hg^{2+}, Cd^{2+}, Tl^{+}). Others like Ti^{3+}, Mn^{3+}, Mn^{2+} would almost certainly introduce electronic conduction depending on the processing conditions, which can be expected from analysing their diagrams for the density of states (DOS) where it can be appreciated that the conduction band is dominated by states from the titanium ions.

A review on the defect chemistry of NBT by Yang *et al.* shows that isovalent dopants, for example zirconium, can decrease the bulk conductivity by decreasing the mobility of the charge carriers due to their stronger bonds with oxygen [7]. This review also discussed how experimental results agree with the calculations of He and Mo [42] about B-site acceptors trapping oxygen vacancies based on the fact that A-site acceptors increase the conductivity noticeably more than B-site acceptors even if the amounts of vacancies they introduce are comparable. It is interesting that, amongst B-site dopants in that review, only magnesium increases the conductivity in a similar manner to A-site dopants and some of the other B-site dopants (i.e. zinc) decrease the conductivity compared against undoped NB49T. Based on their previous work and

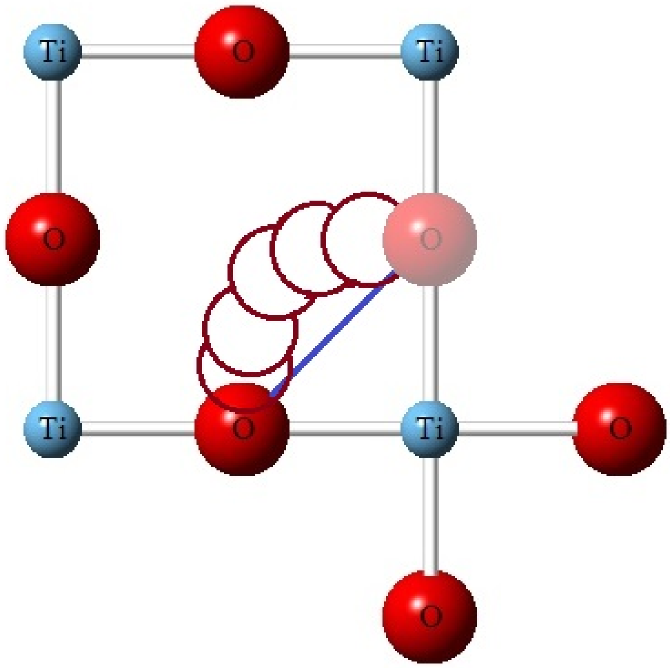

Figure 2.9: Migration path for O^{2-} in a $ATiO_3$ perovskite. After Saiful Islam [43].

a possible physical limit for oxide ion diffusivity in perovskites considered by De Souza [44], Yang *et al.* suggest that the oxide ion conduction in NBT is optimised by magnesium, calcium or strontium doping of NB49T since their bulk conductivities are close to the conductivity that can be predicted from the limit in diffusivity estimated by De Souza.

Trapping of the oxygen vacancies by other point defects (particularly acceptor dopants) is a known effect in oxides such as YSZ, $SrTiO_3$ and $LaGaO_3$ [45, 46, 47]. Bogicevic and Wolverton studied trapping of oxygen vacancies in YSZ and scandia stabilised zirconia (ScSZ) through DFT and concluded that the size mismatch between dopant and zirconium introduces an elastic term for the association of vacancies with the cations. This term is minimised when the vacancy is closer to the smallest cation, and its preference to associate or not with the cations is determined by the combination of the elastic term and an electronic term dominated by the electrostatic interaction of the effective charges for the defects [48]. Norberg *et al.* studied defect association in YSZ and ScSZ through the analysis of pair distribution functions obtained from neutron diffraction and observed in YSZ a tendency for the oxygen vacancies to associate with zirconium ions but no preference for either cation in ScSZ [49], although the main source of trapping in both systems seems to be an intrinsic tendency in the lattice for the clustering of oxygen vacancies [50]. In the case of acceptor-doped $LaGaO_3$, Saiful Islam and Davies reported, based on simulations from molecular dynamics, that the the occupancy of the cation sites and the size difference between the host and the dopant determine how strong the trapping will be. The weakest binding occurs when the dopant is closest in size to the host [51].

Yang *et al.* explored the effect of Sr-doping on the A-site of NBT and showed it provides a small improvement over Mg-doping at an equivalent level (nominally introducing the same level of oxygen vacancies). They also show that the change in activation energy for the bulk conductivity can be predicted by treating the system as a composite of the tetragonal and low symmetry phases using extrapolated conductivities from high and low temperature data in a Maxwell model [52].

Meyer and Albe [53] performed an in-depth study of the change in activation energy for oxide ion conduction in NBT through DFT calculations. They observe energy profiles along some migration paths that could permit long range migration but they highlight the strong effect that local ordering and symmetry have on the migration barriers and conclude that the change in activation energy arises from the differing ease for defect association and vacancy migration in the different phases (i.e. for the rhombohedral phase the activation energy contains a term for migration and a term for defect association, whereas for the tetragonal phase the migration term alone is enough to account for the experimental activation energy). Koch *et al.* made a detailed study of the change in activation energy of doped NBT relying on an analytical model with migration energies from Meyer and Albe's DFT calculations and considering different kinetics for the defect association in different phases. This lead to a temperature dependent concentration of free vacancies being obtained from the law of mass action alongside the thermally activated migration [54]. Their results highlight the strong effect that phase coexistence and the different behaviour of the oxygen vacancies in each phase have towards the temperature dependence of the bulk conductivity.

Also in Reference [52] the $Na_{0.5}Sr_{0.02}Bi_{0.47}TiO_{2.975}$ composition is reported to have the highest bulk conductivity amongst NBT-based materials (about half an order of magnitude higher than NB49T). This composition also has a significantly more stable conductivity with time compared against doped $\delta-\mathrm{Bi_2O_3}$ and improved resistance to reducing atmospheres (it can withstand up to 550 °C in 5% H_2-95% N_2) compared against undoped NBT. A conductivity of $\sim 10^{-3}\ \mathrm{S\,cm^{-2}}$, value suitable for a $1\,\mathrm{\mu m}$ thick electrolyte in a solid oxide fuel cell (SOFC) [55], is achieved around 350 °C. In terms of conductivity this material seems promising for constructing low temperature SOFCs. To determine its viability the stability under more reducing atmospheres (as fuels), finding compatible electrode materials and studying the performance of cells are aspects that should still be explored. Lu *et al.* reported a SOFC based on 2%Mg-NB49T (with the anode being a composite of NiO and the electrolyte material and the cathode a composite with Ag) at 600 and 650 $^\circ\mathrm{C}$ producing peak power densities of 2.3 and 6.0 $\mathrm{mW\,cm^{-2}}$ [56], which are far inferior to those of the order of $\mathrm{W\,cm^{-1}}$ observed in the most advanced cells based on YSZ, LSGM or Gd-doped CeO_2 [55]. Lu *et al.* attribute the poor performance to partial reduction of the electrolyte under the low p_{O_2} turning it into a mixed ionic-electronic conductor.

Chapter 3

Methods

3.1 Solid state processing

The most straightforward technique for preparing ceramics is solid state synthesis, also called the conventional ceramic method. In this method, simple reactants (i.e. oxides, carbonates, nitrates) are mixed and treated at high temperature to ease the diffusion of ions in the solids and allow the reaction to proceed at an appreciable rate. Often the reaction takes place at the interface of the reactants, but as the product forms between the grains of reactants the reaction becomes slower since the ions must diffuse through the product. This method therefore requires high temperatures and it is common practice to have intermediate milling steps to promote contact of the still unreacted surfaces. In order to obtain higher surface contact between the reactants, small particle sizes are highly desirable, therefore the mixing of the reactants is usually done by milling them together. For some elements, like alkali and alkaline earths, whose oxides are highly hygroscopic it is preferable to use oxysalts such as carbonates or oxalates that decompose into the oxide when heated. To obtain samples for which the electrical properties can be measured the powders are pressed into pellets which are then sintered to produce mechanically stable, dense pellets which ideally have no interconnected porosity.

Most samples in this work were prepared through conventional solid state synthesis. The starting materials used were Na_2CO_3, Bi_2O_3, TiO_2, MgO, ZnO, and Nb_2O_5. The supplier, purity and drying conditions for the starting materials used are shown in Table 3.1. For all samples, the dry reactants were weighed in appropriate amounts and ball milled together using yttria stabilised zirconia media in isopropanol for six hours. For sintering, pellets of 10 mm diameter were uniaxially pressed and then subjected to cold isostatic pressing at 30000 psi. Alumina crucibles were used for all heat treatments. The green pellets of all materials in this work were placed on sacrificial powder and covered with more powder to minimise the loss of volatiles during sintering.

Table 3.1: Supplier, purity and drying conditions for each reagent used in this work.

Reagent	Supplier	Purity (%)	Drying temperature (°C)	Drying time (h)
Na_2CO_3	Fisher	99.5	300	12
Bi_2O_3	Acros Organics	99.9	300	12
TiO_2	Sigma Aldrich	99.9	900	6
MgO	Honeywell	99	900	12
ZnO	Sigma Aldrich	99.9	600	12
Nb_2O_5	Sigma Aldrich	99.99	900	12

3.2 Powder X-ray diffraction

X-rays encompass wavelengths of similar magnitude to the spacings between crystal planes and can therefore be diffracted by them. The periodic nature of crystals results in constructive interference occurring at specific angles for different sets of planes, giving rise to discrete diffraction patterns. The position in the diffraction pattern for each peak arising from a given set of planes is predicted by Bragg's law [57] (Equation 3.1) where n is a whole number (usually taken as 1 for simplicity), λ is the wavelength of the incident radiation, d is the interplanar spacing for that set of planes and θ is the angle of the incident beam.

$$n\lambda = 2dsin\theta \tag{3.1}$$

The intensity of the peaks is determined by the identity and position in the unit cell of the atoms or ions that form the crystal. The interaction of the X-rays with the material is through the electronic clouds, therefore elements with higher atomic number scatter X-rays more strongly. The specific position of the atoms or ions in the unit cell can introduce destructive interference at certain angles, affecting the peak intensities. In powdered samples the morphology of the particles can be extremely important, as shapes such as needles or sheets will align themselves in the sample leading to a higher ratio of certain planes satisfying Bragg's law over others. This is known as preferred orientation and it can significantly change the relative intensities of a diffraction pattern, favouring certain groups of planes over others.

The peak positions and intensities of a model system can be predicted quickly, hence a method to solve a materials structure based on its powder diffraction pattern was developed by Rietveld [58, 59]. In the Rietveld method, a diffraction pattern is calculated based on an estimated unit cell (consisting of the space group, lattice parameters and atomic positions) and then used to determine the difference between the experimentally observed pattern and the one predicted from the model. The difference is minimised through a least-squares method by allowing the parameters in the model to vary until convergence is obtained. It is possible to obtain valuable structural information regarding the size and contents of the unit cell from a carefully performed refinement. Sample effects such as preferred orientation can also be included in a Rietveld refinement, although it significantly increases the complexity. The goodness of fit between the modelled and the observed data can be judged through parameters such as R_{wp} (Equation 3.2) and χ^2 (Equation 3.3) [60]:

$$R_{wp}^2 = \frac{\Sigma_i w_i (y_{oi} - y_i)^2}{\Sigma_i y_{oi}} \tag{3.2}$$

where w_i is a weighting factor according to the intensity of point i, y_{oi} is the observed intensity at point i and y_i the calculated intensity at point i.

$$\chi^2 = (\frac{R_{wp}}{R_{exp}})^2 \tag{3.3}$$

With R_{exp} being:

$$R_{exp}^2 = \frac{N - P}{\Sigma_i w_i y_{oi}^2} \tag{3.4}$$

for which N is the number of data points and P the number of refined variables. The lower the R_{wp} value is, the less the predicted pattern deviates from the observed one. For XRD data, R_{wp} values around 10 $\%$ are usually expected from a reasonable refinement [61]. The R_{exp} shown in Equation 3.4 corresponds to the best possible R_{wp} that would be achieved with an ideal model for that number of data points and refined parameters. χ^2 is the quotient of R_{wp} and R_{exp}, therefore the closer this value is to unity, the better the quality of the refinement.

XRD patterns were obtained at ambient conditions on a Bruker D2 Phaser diffractometer with a Cu source ($\lambda = 1.54184$ $\AA$) on powders pressed into a front filled holder, from 10 to $85°$ using 0.02 ° steps with a scanning rate between 0.3 and 0.6 $\mathrm{s/step}$. To identify the phases present in the samples the patterns were compared against entries in the PDF-4+ database. For determination of lattice parameters, crushed pellets were mixed with a silicon standard reference material from NIST (SRM 640e). The mixtures were scanned with 0.2 ° steps and scanning rates of 0.5 to 1 $\mathrm{s/step}$.

To extract the lattice parameters Rietveld refinements were carried out using GSAS [62] and EXPGUI [63]. The general strategy consisted in starting from a published structure (References [64] for Cc and [65] for $Pnma$) or the results of the refinement corresponding to a lower doping level. Initially the phase fractions of the sample and silicon standard alongside the background (as a shifted Chebyschev polinomial with 6 or 8 terms) are refined. Next, the lattice parameters of the sample are refined, followed by the profile terms (type 2 in GSAS), the "shift" term maintaining the silicon cell fixed to its certified value (0.5431179 nm), this accounts for displacement errors in the diffractometer. The Gaussian terms of the profile functions are constrained to be the same for the sample and the internal standard, while the Lorentzian terms and the asymmetry are allowed to differ. The positions and thermal displacement parameters of Na^+ and Bi^{3+} ions are constrained to be the same, as well as the positions and thermal displacement parameters of the B-site ions. The positions of the B-site ions are kept fixed when the space-group is non-centrosymmetric, and the position of the silicon atom in the SRM is naturally kept fixed throughout. After the peak profiles, the atomic positions were refined, starting with the A-site ions, then the B-site ions followed by the oxide ions when possible (in some cases it led to unstable refinements). Finally, the thermal displacement parameters are refined starting with the Si standard and following the same sequence as the positions for the NBT phase. The site occupancies are fixed to correspond to the nominal compositions.

3.3 Neutron diffraction

Neutrons can also present wavelengths of similar magnitude to the interplanar spacings in crystals and be diffracted, however unlike X-rays they interact with the nuclei rather than the electron clouds. The scattering power of the elements is essentially random across the periodic table. This often allows neutrons to provide contrast between neighbouring elements and sensitivity to light elements in the presence of heavy ones. The fact that neutrons interact with nuclei and not electrons also means they are highly penetrating, which makes them a bulk probe and allows for easier implementation of complex sample environments. Unfortunately it also means that larger amounts of sample are required compared to XRD.

Neutron diffraction (ND) data were collected at the ISIS neutron and muon source in the Rutherford-Appleton Laboratory using the POLARIS diffractometer. The powders were placed in vanadium cans. For all samples ND room temperature measurements were done first, followed by measurements in the cryostat cooling down to 4.2 K and then collecting at other temperatures on heating, measurements in a furnace above room temperature were also done on heating. For all three types of measurements (room temperature, low temperatures, high temperatures) the diffractometer tank (and cryostat or furnace when used) was evacuated to $10^{-5} \sim 10^{-4}$ mbar at the start of the experiment. Further details of each experiment will be given in Chapters 5 and 6.

3.4 Impedance spectroscopy

The bulk conductivities of the studied ceramics were extracted from their impedance spectra based on the relaxation times and capacitance values. Impedance spectroscopy (IS) allows us to separate and distinguish the contributions to the electrical response of a ceramic from the bulk, grain boundaries and electrode effects. Impedance spectra are obtained by applying an alternating voltage over a wide range of frequencies and measuring the magnitude of the impedance and the phase shift between the applied voltage and the electrical current. The frequency dependence of the magnitudes of the impedance for a pure resistor, a pure capacitor and a pure inductor are illustrated in Figure 3.1: a resistor has no frequency dependence, the impedance of a capacitor is inversely proportional to the frequency and that of an inductor is directly proportional.

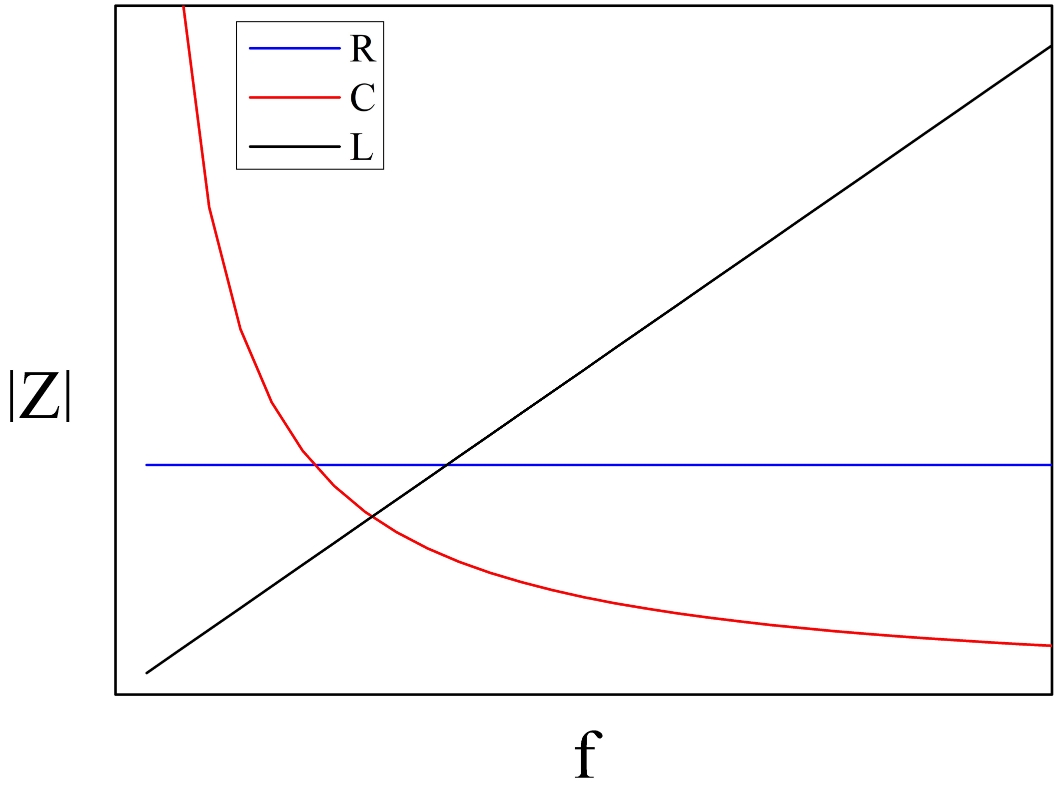

Figure 3.1: Magnitude of the impedance as a function of frequency for a resistor (R), a capacitor (C) and an inductor (L).

Impedance data can be presented in any of four related formalisms, impedance (Z*), admittance (Y*), relative electric modulus (M*) and relative permittivity (ε*). The relations between them are presented in Equations 3.5 to 3.8 where $j^2 = -1$, C_0 is the capacitance of the empty cell and ω the angular frequency ($2\pi f$).

$$Z^* = Z' - jZ'' \tag{3.5}$$

$$Y^* = 1/Z^* = Y' + jY'' \tag{3.6}$$

$$\begin{array}{lcl} M^* & = & j\omega C_0 Z^* = M' + jM'' \\ M' & = & \omega C_0 Z'' \\ M'' & = & \omega C_0 Z' \end{array} \tag{3.7}$$

$$\varepsilon^* = 1/M^* = \varepsilon' - j\varepsilon'' \tag{3.8}$$

In a ceramic sample, each electroactive region can often be modelled as a 'parallel RC element' consisting of a resistor and a capacitor connected in parallel. The total impedance for a single RC element is presented in Equation 3.9.

$$Z^* = \frac{R}{1 + (\omega RC)^2} - jR\frac{\omega RC}{1 + (\omega RC)^2} \tag{3.9}$$

Equation 3.7 allows then to determine the electric modulus:

$$M^* = \omega C_0 R\frac{\omega RC}{1 + (\omega RC)^2} + j\frac{C_0}{C}\frac{\omega RC}{1 + (\omega RC)^2} \tag{3.10}$$

In the impedance spectrum, plotted as the imaginary part of the impedance versus the real (a Z* plot), provided the time constants are different enough (by at least two orders of magnitude) each RC element produces a semicircle with a maximum at a frequency ω_{max} such that $RC\omega_{max} = 1$. The diameter of the semicircle corresponds to the resistance R. Knowing the resistance and the frequency at the maximum of the semicircle, the capacitance C can be calculated. The value of the capacitance allows the feature that generated each arc to be identified. For example, typical capacitances for non-ferroelectric bulk responses are around 10^{-12} F/cm, grain boundaries show between 10^{-11} and 10^{-8} F/cm and the bulk in a ferroelectric material ranges from 10^{-10} to 10^{-9} F/cm [66]. The same information can also be extracted from the spectroscopic M'' plot, where a Debye peak centred at the frequency where $RC\omega_{max} = 1$ appears. Following Equation 3.10, the height of this peak will then be $1/2C$. In a sample where several responses appear, the modulus peak will highlight that with the smallest capacitance, which can reliably be expected to be the bulk response.

In this work the bulk conductivities of the materials were extracted from the M" spectroscopic plots using the extracted C and ω_{max} values to calculate R. The measured pellets had electrodes painted with gold paste fired at 850 °C for 2 hours. Impedance spectra were measured between room temperature and 850 °C under air using an Agilent 4980A precision LCR meter in the frequency range 20 Hz $\sim$ 1 MHz, applying 0.1 V. Lower frequency (10 mHz to 1 MHz) data were collected for some samples under nitrogen, air or oxygen using a Solartron SI 1260 impedance analyser applying 0.1 V.

3.5 Dielectric measurements

A Hewlett-Packard 4284A precision LCR meter was used to measure the capacitance and dielectric loss ($tan\delta$) of sintered pellets at 1, 10, 100, 250 and 1000 kHz. The relative permittivity (ε_r) was calculated from the measured capacitance based on Equation 3.11.

$$\varepsilon_r = \frac{Cd}{\varepsilon_0 A} \tag{3.11}$$

where ε_0 is the permittivity of free space, A the area of the electrodes and d the separation between electrodes. $tan\delta$ is defined as $tan\delta = \varepsilon''/\varepsilon'$, using Equations 3.5 to 3.8. This can also be expressed in terms of the other three formalisms as shown in Equation 3.12.

$$tan\delta = \frac{\varepsilon''}{\varepsilon'} = \frac{M''}{M'} = \frac{Z'}{Z''} = \frac{Y'}{Y''} \tag{3.12}$$

For a single parallel RC element, Equations 3.9 and 3.12 can be used to determine a relation between the dielectric loss and the conductivity shown in Equation 3.13.

$$tan\delta = \frac{1}{\omega RC} = \frac{\sigma}{\omega C} \tag{3.13}$$

3.6 Ionic transport number measurements

More than one conduction mechanism may be simultaneously active in a real material, the quotient between the conductivity arising from a single type of carrier between the total conductivity is the transport number of that carrier. All materials posses some level of electronic conductivity, therefore in the simplest case of an ionic conductor there are two contributions to the total conductivity: one electronic and one ionic. One method to determine how much of the conductivity corresponds to the ionic component relies on Nernst's equation (Equation 3.14), where E is the electromotive force (emf) generated, t_{ion} the ionic transport number, k is Boltzmann's constant, T the temperature, n the number of electrons exchanged in the reaction, e the elemental charge, a_{ox} and a_{red} the activities of the oxidising and reducing species, respectively [8]. For convenience, the thermodynamic activities are often replaced by concentrations or partial pressures.

$$E = E^0 - t_{ion}\frac{kT}{ne}ln\frac{a_{ox}}{a_{red}} \tag{3.14}$$

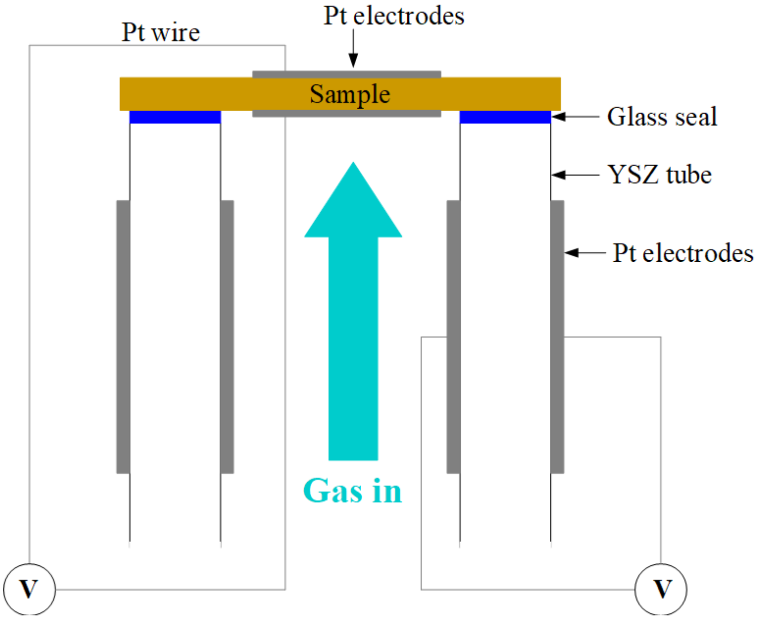

Figure 3.2: Schematic experimental set-up for ionic transport number measurements.

By setting different concentrations of the transported species to either side of a sample an emf is established. As long as no external voltage is applied to the system the emf will be directly proportional to the ionic transport number. An experiment that enables to quickly estimate the ionic transport number [8] consists of using a reference alongside the sample. Since both materials are exposed to the same concentrations on both sides and are at the same temperature, the only source for a difference between the emf measured from each is the ionic transport numbers. The quotient between the emf values will therefore provide the quotient between the ionic transport numbers. In this work an yttria-stabilised zirconia tube was used as a reference for oxide ion conductivity and its ionic transport number assumed to be unity. A sample pellet is placed on top of the YSZ tube and a glass seal made between them. Nitrogen is then flowed inside the tube and the outside is kept in air. Both sample and reference have platinum electrodes; a schematic of the experiment is displayed in Figure 3.2.

3.7 Scanning electron microscopy

High energy electrons have much shorter wavelengths than visible light [67] and according to Rayleigh's resolution limit (Equation 3.15) [68] this allows for a better resolution if used as the radiation in a microscope:

$$r = \frac{0.61\lambda}{n sin\alpha} \tag{3.15}$$

where r is the smallest separation between two objects that can be resolved by passing a beam of wavelength λ in a medium of refractive index n through an aperture of semiangle α to the sample. This limit arises due to the diffraction of the incident beam as it passes through the aperture which should be small to minimise the effect of aberrations on the resolution.

A scanning electron microscope (SEM) impinges an electron beam on a spot of the sample surface and detects the intensity of electrons coming from the sample. The beam is scanned across an area of the sample to build an image. As the beam falls on the sample, the highly energetic electrons can knock out electrons from the atoms in the sample, this produces secondary electrons which originate from the sample. Areas that are more exposed will produce a higher yield of secondary electrons and appear brighter, therefore the secondary electrons provide a topological contrast. A detector for backscattered electrons is also used. This detects electrons that are ”slung” back by the nuclei in the sample. This is much more likely for elements with high atomic numbers than for light elements, hence the backscattered electron image gives chemical contrast, with brighter areas implying the presence of the heavier elements in the sample.

Another consequence of shining an electron beam on the sample that can be exploited is the generation of characteristic X-rays. When the incident electrons knock out core electrons in the sample, other electrons will fall down in energy to occupy the lower energy states, emitting photons with the corresponding energy difference between these levels. Since the energy of the X-rays generated in this manner corresponds to differences between core levels, they are not affected significantly by the chemical environment of the atom in which they originate and are therefore characteristic of the element that produces them. The energy of the X-rays that radiate from the sample can be recorded and compared against the known spectra of the elements to determine which are present in the sample. Furthermore, the intensities can be used to quantify how much of each element is present in that region of the sample. This technique is known as energy dispersive X-ray spectroscopy (EDX or EDS) [69].

SEM is useful for the study of ceramics as the secondary electron images allow to observe microstructural features such as porosity and grain boundaries. Backscattered electrons allow the easy detection of secondary phases if their composition is significantly different and EDX enables quantitative chemical analysis of the grains which can be used to confirm the formation of solid solutions or identify secondary phases.

In this work, powder samples were dispersed in isopropanol and dropped on carbon stickers mounted on an aluminium stub. Pellets were prepared for SEM by mirror polishing a surface, in some cases a piece was then thermally etched at 90% of its sintering temperature (in °C) for one hour. Both polished and etched samples were carbon coated. The microscope used was a Philips XL30 with a field emission gun operating at 20 kV and fitted with an EDX detector from Oxford instruments.

3.8 Thermogravimetric analysis

Thermogravimetric analysis (TGA) consists on monitoring the mass of a sample as the temperature changes at a controlled rate. For ceramic oxides this can provide valuable information about the presence of adsorbed species and the loss or gain of oxygen at variable temperature. For this work a PerkinElmer Pyris TGA 1 was used with $\sim$70mg of powder loaded on alumina pans and heating/cooling rates of 10 $^{\circ}\mathrm{C\,min^{-1}}$.

Chapter 4

$Na_{0.5}Bi_{0.5}TiO_3$-$Bi(M_{2/3}Nb_{1/3})O_3$ solid solutions

4.1 Introduction

As discussed in the Literature review (Chapter 2), He and Mo [42] studied the diffusion of oxide ions in NBT through Density Functional Theory (DFT) and calculated the activation energies for the three possible types of saddle points for the diffusion of an oxide ion from an occupied lattice site to a vacant one. Those corresponding to Na-Na-Ti triangles have very high values between 1.0 and 1.3 eV whereas Bi-Bi-Ti triangles have values of $\sim$0.22 eV and Na-Bi-Ti triangles give barriers of 0.6 to 0.85 eV which are comparable to the values obtained from experiments. They also highlight that acceptor dopants on the B-site (such as Mg) can strongly trap the oxide ions as suggested by a dramatic difference in their calculated activation energies for Na-Bi-Mg triangles of 1.0 to 1.3 eV and for Na-Na-Mg triangles of 2.1 to 2.2 eV. Their calculations suggest that A-site doping is preferable to B-site doping to increase the conductivity of NBT and that an increased proportion of Bi to Na could help obtain higher oxide ion conductivity at lower temperatures.

Several $BiMO_3$ perovskites are known as high pressure phases, for example $BiAlO_3$, $BiMnO_3$, $BiScO_3$, $BiMg_{1/2}Ti_{1/2}O_3$ and $BiZn_{1/2}Ti_{1/2}O_3$ [70, 71, 72, 73]; however, stable solid solutions with other perovskites such as $BaTiO_3$, $SrTiO_3$, $PbTiO_3$ or $KNbO_3$ can be obtained at ambient pressure [74, 75, 76, 77]. Aiming to develop improved lead-free piezoelectrics and high temperature dielectrics, some NBT-$BiMO_3$ solid solutions have been reported in the literature such as NBT-$BiScO_3$, NBT-$BiAlO_3$ and NBT-$BiZn_{0.5}Ti_{0.5}O_3$ [78, 79, 13]. Considering the low activation energy of the oxide ion hopping via Bi-Bi-Ti saddle points discussed above, solid solutions between NBT and $BiMO_3$ perovskites become particularly interesting for exploring their conduction properties. In Reference [14] solid solutions between NBT and $BiAlO_3$ (BA) are studied and a systematic decrease of the conductivity is observed, as shown in Figure 4.1.

Increasing BA content is accompanied by a decrease in ionic transport number (t_{ion}): for undoped NBT $t_{ion} > 0.9$, with 2 % doping t_{ion} drops below 0.85 and above 6 % it is lower than 0.15. As described in that work, the switch in conductivity from predominantly ionic to mixed ionic-electronic and eventually to predominantly electronic as the BA content increases indicates the mobility of the oxygen vacancies is decreasing, which can be attributed to trapping of the vacancies by the aluminium ions acting as traps to form $(\mathrm{Al}'_{\mathrm{Ti}}-\mathrm{V}_{\mathrm{O}}^{\bullet\bullet})^{\bullet}$ complexes.

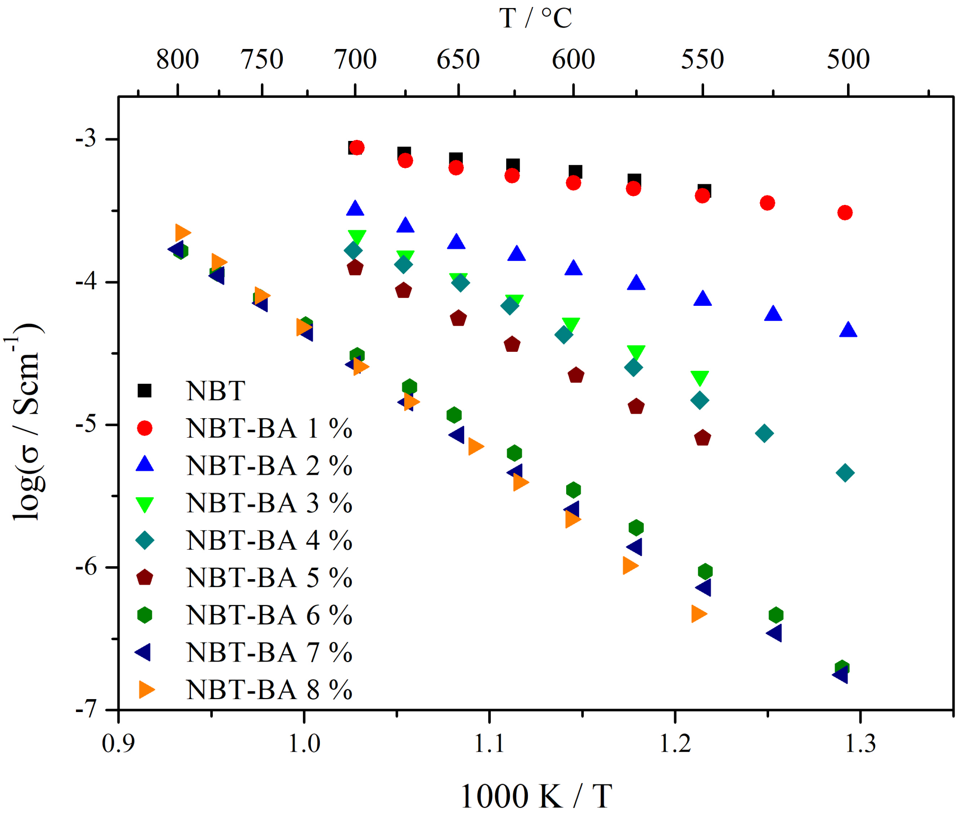

Figure 4.1: Arrhenius plot of bulk conductivites of NBT-BA compositions. After Yang *et al.*, J. Mater. Chem. C, 2017, **5**,7243 (Reference [14]). Published by The Royal Society of Chemistry.

Exploring the behaviour of other NBT-$BiMO_3$ solid solutions is of interest to establish if, as suggested in Reference [14], the acceptors introduced will always act as traps for oxygen vacancies and if so, to determine how the relative trapping strength varies for different acceptors in NBT. In this work, solid solutions between NBT and $BiMg_{2/3}Nb_{1/3}O_3$ (BMN)or $BiZn_{2/3}Nb_{1/3}O_3$ (BZN) have been chosen to study their conductivity and dielectric properties, assuming they will form according to the reaction shown in Equation 4.1, since no report of them was found in the literature.

$$(1{-}\mathrm{x})\,((1/4)\mathrm{Na_2O} + (1/4)\mathrm{Bi_2O_3} + \mathrm{TiO_2})\; + \;\mathrm{x}\,((1/2)\mathrm{Bi_2O_3} + (2/3)\mathrm{MgO} + (1/6)\mathrm{Nb_2O_5}) \longrightarrow \mathrm{Na_{1/2-x/2}Bi_{1/2+x/2}Mg_{2x/3}Nb_{x/3}Ti_{1-x}O_3} \tag{4.1}$$

4.2 Results and discussion

4.2.1 $Na_{0.5}Bi_{0.5}TiO_3$-$BiMg_{2/3}Nb_{1/3}O_3$

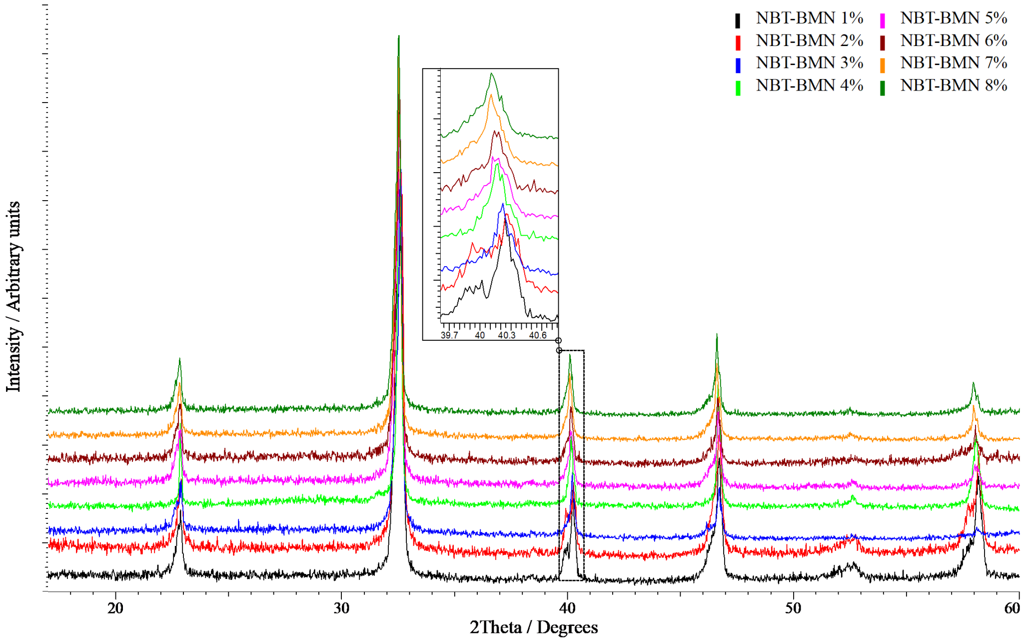

Figure 4.2: XRD patterns for NBT-BMN pellets.

The mixed reactants for (1-x)$Na_{0.5}Bi_{0.5}TiO_3$-x$BiMg_{2/3}Nb_{1/3}O_3$ compositions with x corresponding to 1, 2, 3, 4, 5 , 6, 7 and 8% in this work were calcined twice at 800 °C for two hours with an intermediate milling step and sintered (buried in sacrificial powder) at 1150 °C for two hours, producing pellets with densities $> 93\%$. Figure 4.2 shows XRD patterns of pellets of NBT-BMN solid solutions from 1 to 8 %, where only peaks for the low symmetry polymorph of NBT ($R3c$ or Cc) are observed. A systematic decrease in the diffraction angles (see inset) indicates the unit cell is expanding with increasing BMN concentration as expected from the larger ionic radii of Nb^{5+} (64 pm) and Mg^{2+} (72 pm) compared to Ti^{4+} (60.5 pm). Lattice parameters and cell volumes obtained from Rietveld refinements of XRD data from crushed pellets mixed with a silicon standard (NIST SRM 640e), as described in Chapter 3 (more details are included in Appendix A), are shown in Figures 4.3 and 4.4 to confirm the formation of a solid solution. An apparent discontinuity for the 3% BMN sample is suspected to be due to an error in measurement as it only appears on the c parameter and the volume and its estimated uncertainties are much higher than for the other samples.

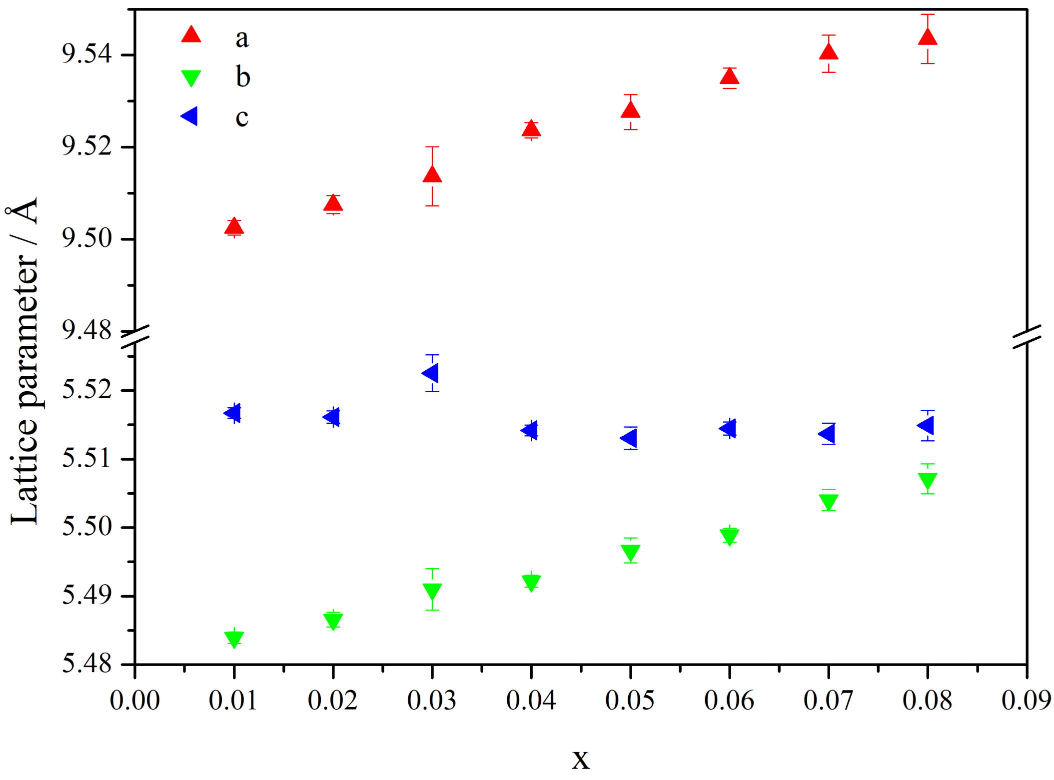

Figure 4.3: Lattice parameters (space group Cc) of NBT-BMN crushed pellets. The error bars shown correspond to 2σ.

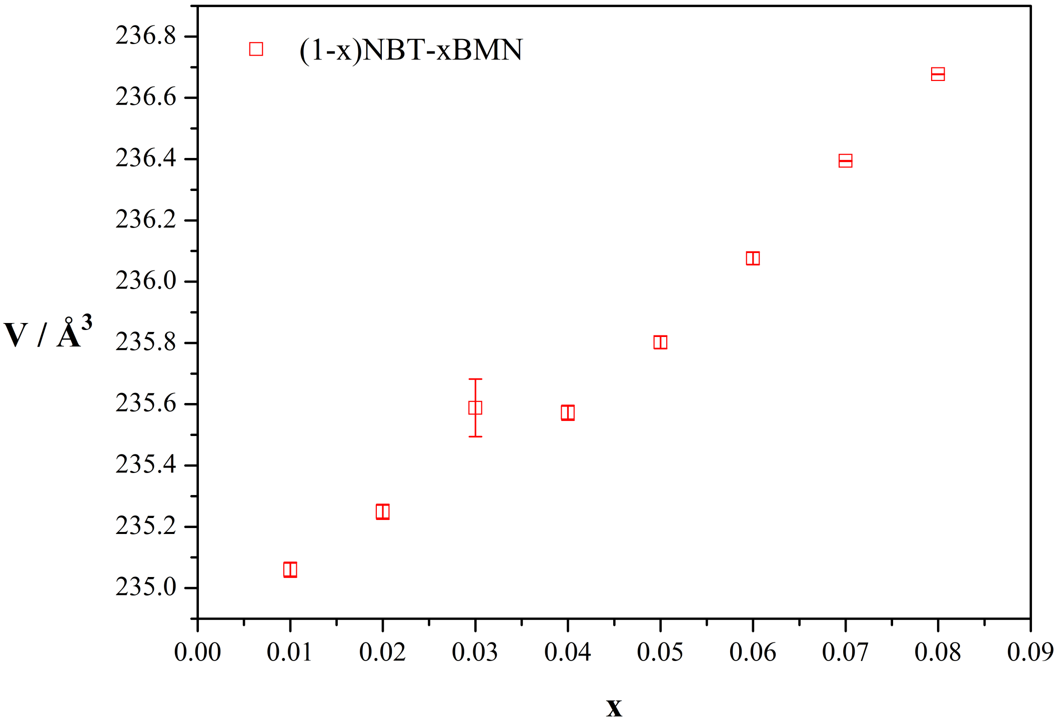

Figure 4.4: Cell volume of NBT-BMN crushed pellets. The error bars shown correspond to 2σ.

Micrographs of polished surfaces for the NBT-BMN pellets with 1, 4 and 7 % BMN are shown in Figure 4.5. The back-scattered electron images show a homogeneous matrix with very small brighter and darker regions at higher BMN concentrations. These are probably bismuth- or niobium-rich and poor regions, respectively, arising from incomplete reactions or insufficient homogenisation of the reactants. EDX spectra were collected from the polished surfaces. The quantification of EDX results in Figure 4.6 show little deviation from the nominal compositions below 6% providing further evidence of formation for the solid solution. The EDX results for the B-site ions, most clearly titanium, suggest the solid solution limit is lower than 7% since the value for the 8% sample shows little change respect to the 7% one, which in turn seems to have a smaller change than what would be expected from the trend up to 6%.

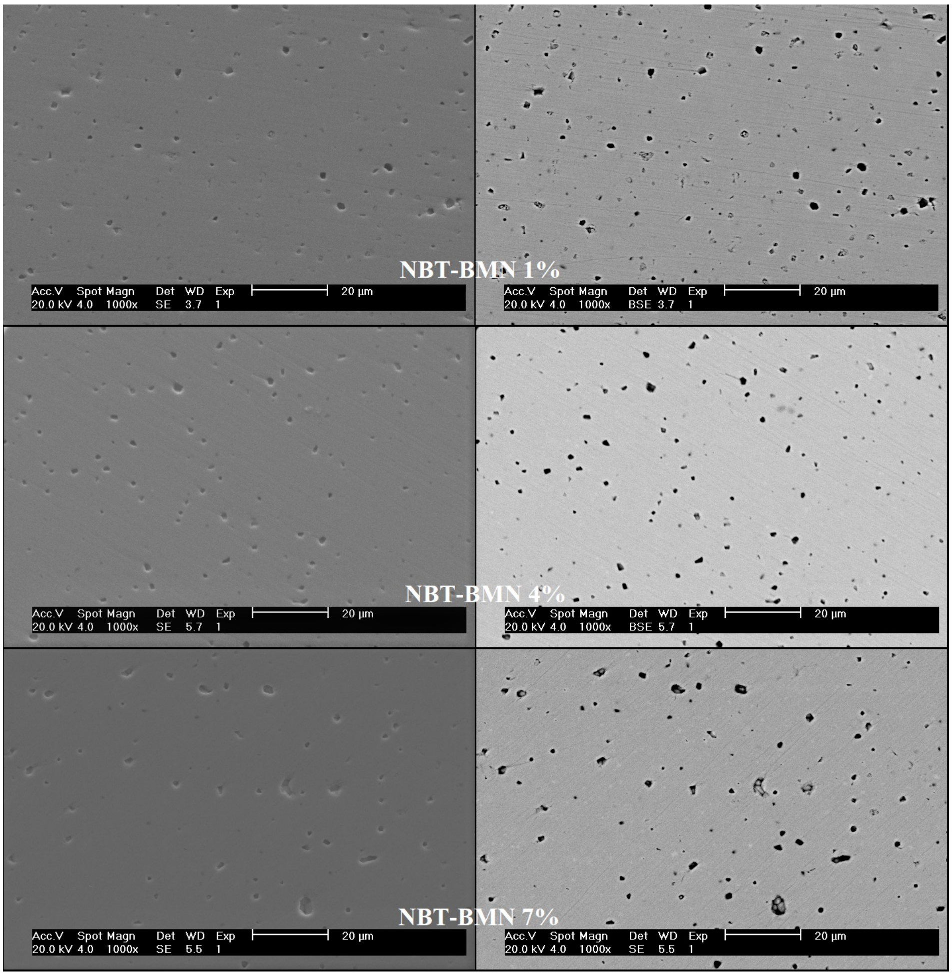

Figure 4.5: Secondary electron (left) and back-scattered electron (right) images of polished pellet surfaces for NBT-BMN 1, 4 and 7 %.

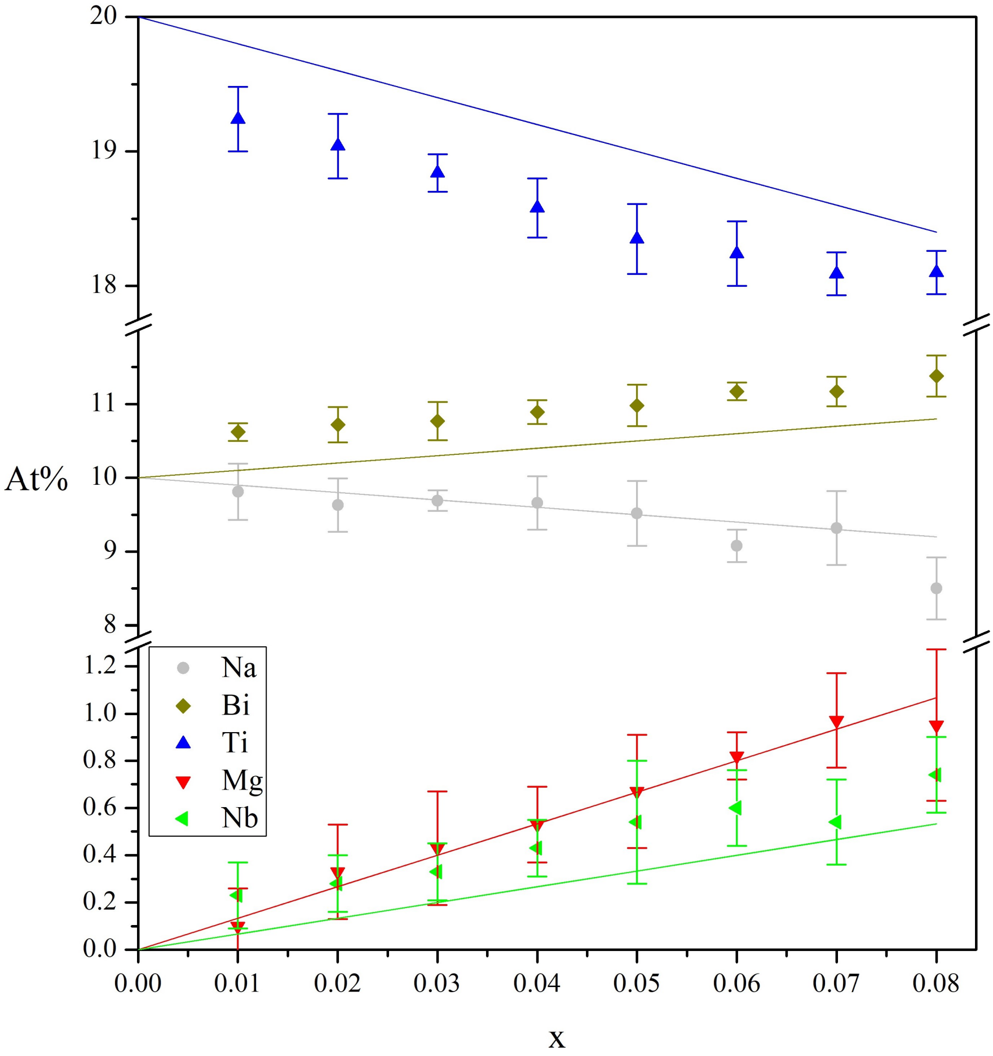

Figure 4.6: Atomic percentages obtained from EDS spectra on polished pellets of NBT-BMN. The solid lines correspond to the amounts expected from the nominal compositions. The error bars shown represent 2 standard deviations.

Figure 4.7 presents the permittivity and dielectric loss temperature profiles obtained from dielectric measurements on heating and cooling for the 1% sample to illustrate the hysteresis observed, which was most noticeable for this sample. Heating data for all NBT-BMN compositions are presented in Figure 4.8. The permittivity decreases slightly with increasing BMN content but the shape of the peak remains the same up to 4%, from 5% the peak becomes slightly broader. In contrast, the dielectric loss decreases dramatically with increasing BMN content and above 5% it remains very low up to 600 °C. This is similar to the case reported by Yang *et al.* [14] for solid solutions between NBT and $BiAlO_3$ (BA) where the increasing amount of acceptor on the B-site associates with the oxygen vacancies and traps them, gradually transforming the system from a good oxide ion conductor to an insulator.

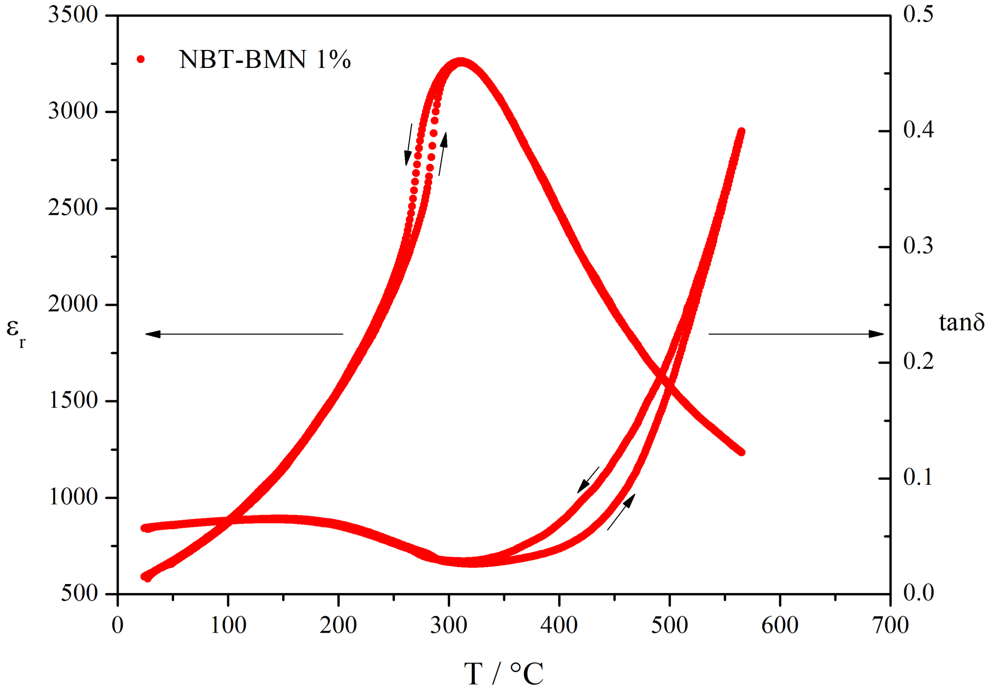

Figure 4.7: Temperature profiles for the permittivity and dielectric loss of NBT-BMN 1% on heating and cooling at 1 MHz.

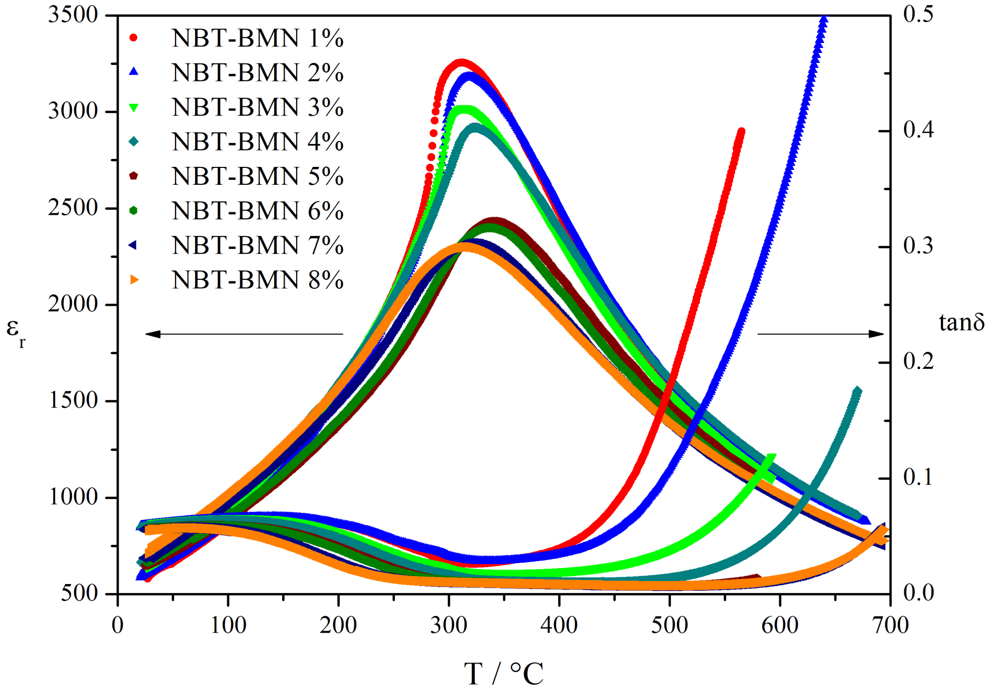

Figure 4.8: Temperature profiles for the permittivity and dielectric loss of NBT-BMN solid solutions on heating at 1 MHz.

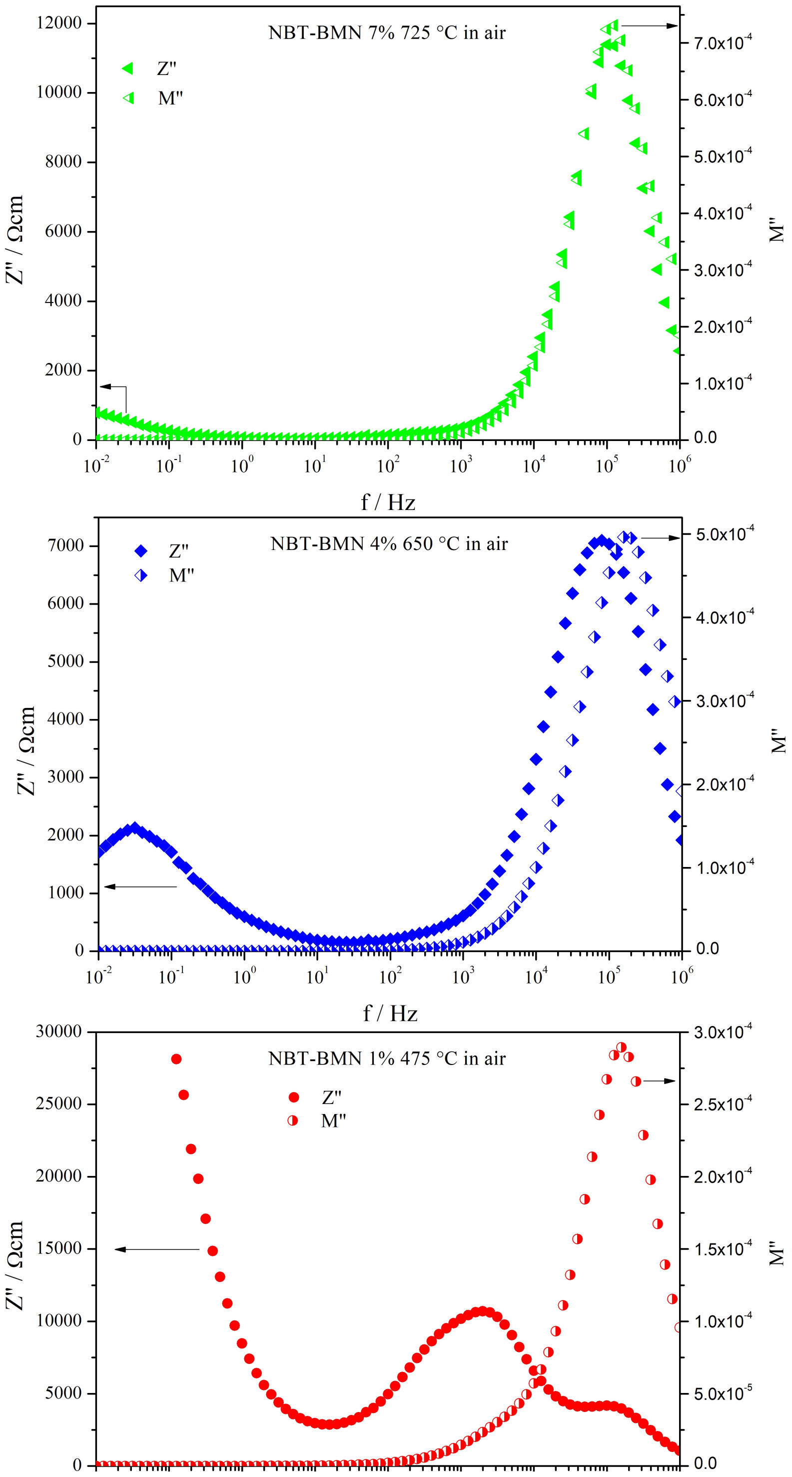

Figure 4.9: Examples of spectroscopic plots of the imaginary components of the impedance and the electric modulus for NBT-BMN 1% (bottom), 4% (middle) and 7% (top).

Selected examples of M” and Z” spectroscopic plots and corresponding complex impedance plots for samples with 1, 4 and 7 % BMN are shown in Figures 4.9 and 4.10, respectively. For the 7% sample a single response in the Z”, M” and Z* plots with a capacitance of the order

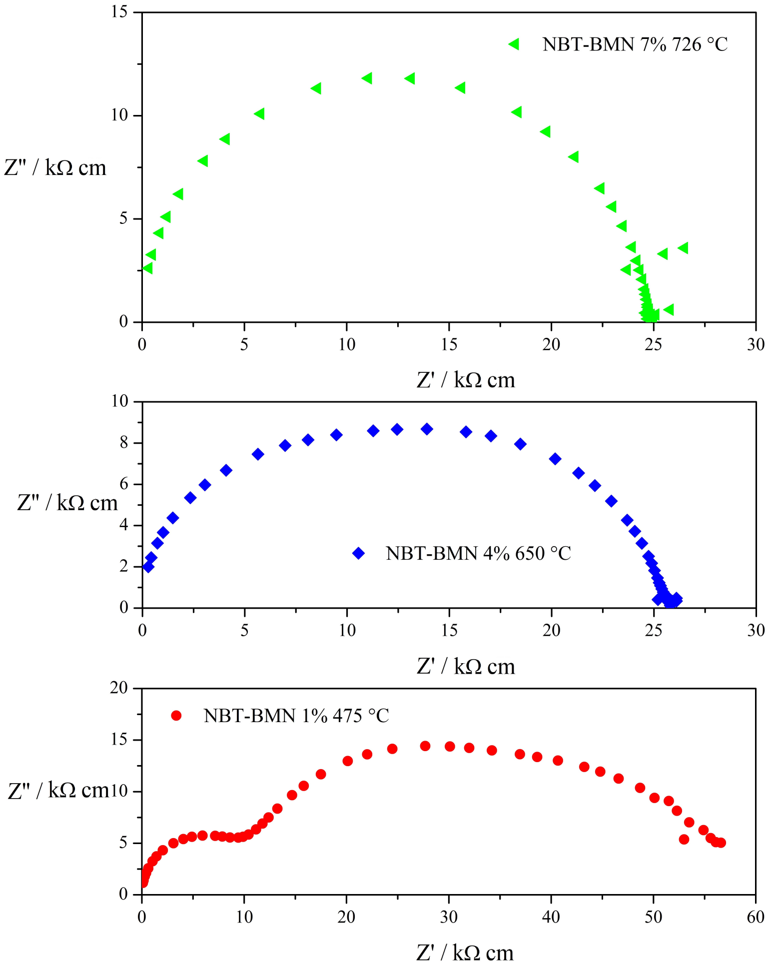

Figure 4.10: Examples of Z* plots for NBT-BMN 1% (bottom), 4% (middle) and 7% (top).

of hundreds of picoFarads per centimetre which is attributed to the bulk is observed within the frequency range. This is also the case for the 6 and 8% samples. The behaviour of the 1 and 2% samples is exemplified with the 1% sample: a high frequency response appears in Z” and M” spectroscopic plots which, based on its capacitance, can be attributed to the bulk and two poorly resolved responses are observed at lower frequencies which could correspond, for example, to grain boundaries or surface layers. The 4% sample is used to illustrate the case of the 3 to 5% samples where the response attributable to the bulk is no longer well resolved from the lower frequency responses. The permittivities extracted from M” spectroscopic plots are plotted in Figure 4.11. Their magnitudes and temperature profiles are reasonable for the bulk of NBT-based ceramics. The bulk conductivities are shown as Arrhenius plots in Figure 4.12. It can be clearly appreciated that the bulk conductivity decreases with increasing BMN content until it becomes nearly as low as NB51T. This behaviour is in agreement with the trend for the dielectric loss and the scenario where the magnesium ions act as traps for the oxygen vacancies.

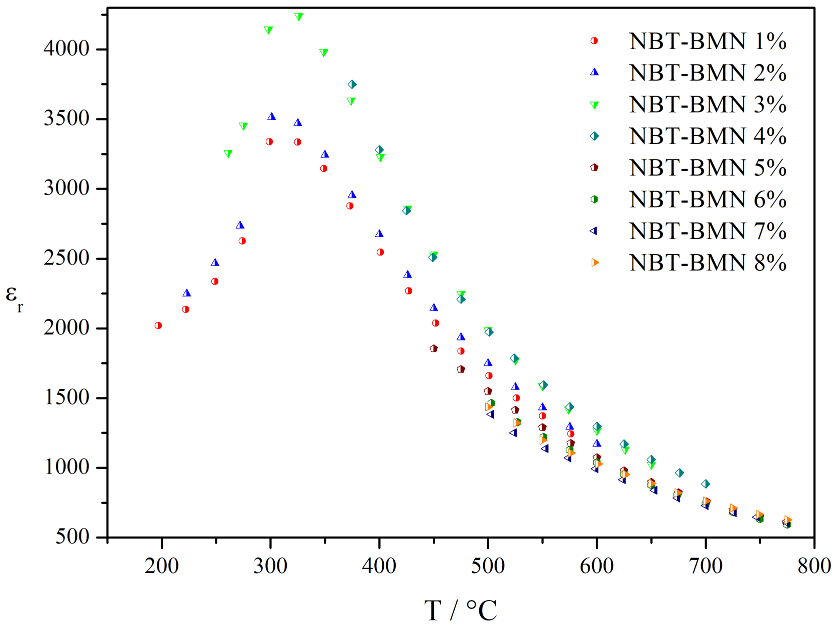

Figure 4.11: Permittivites extracted from impedance spectroscopy for NBT-BMN.

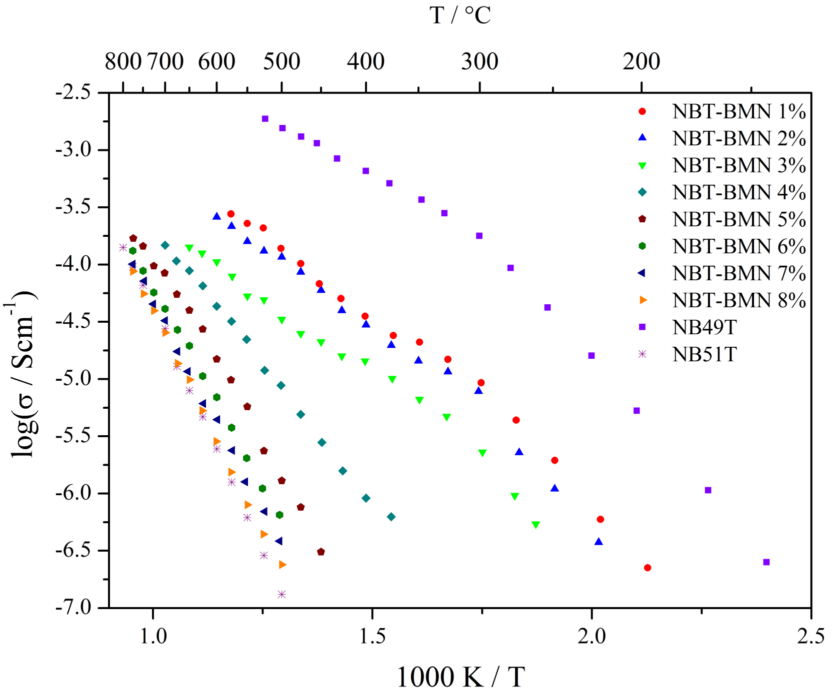

Figure 4.12: Arrhenius plot for bulk conductivities of NBT-BMN.

Figures 4.13 and 4.14 present examples of the atmosphere dependence of the conductivity using M” and Z* plots, respectively. With increasing BMN content the bulk resistance becomes more strongly dependent on the p_{O_2} and the low frequency response is strongly suppressed. For the NBT-BMN 1% example, it can be appreciated that while the bulk response is independent

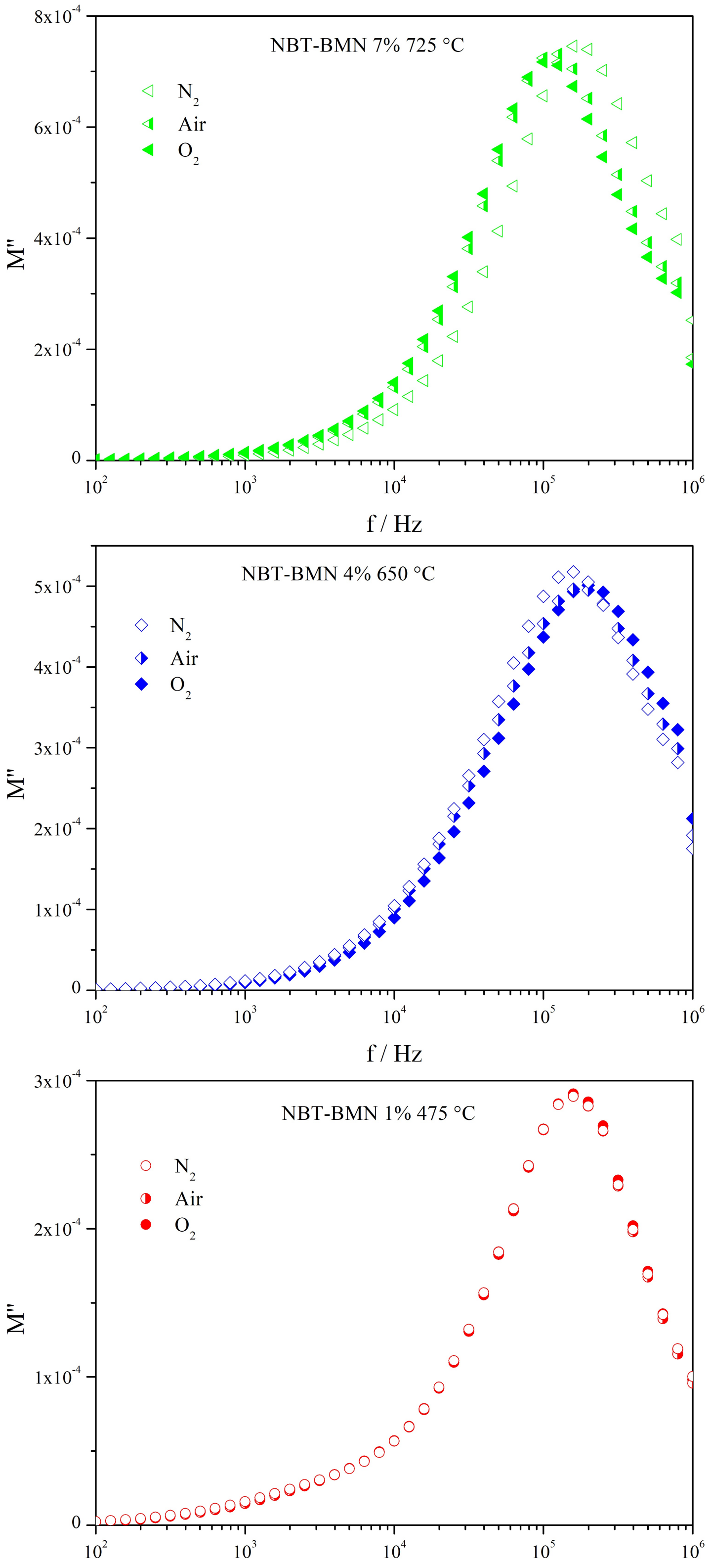

Figure 4.13: Examples of M” spectroscopic plots for NBT-BMN 1% (bottom), 4% (middle) and 7% (top) under O_2, air and N_2.

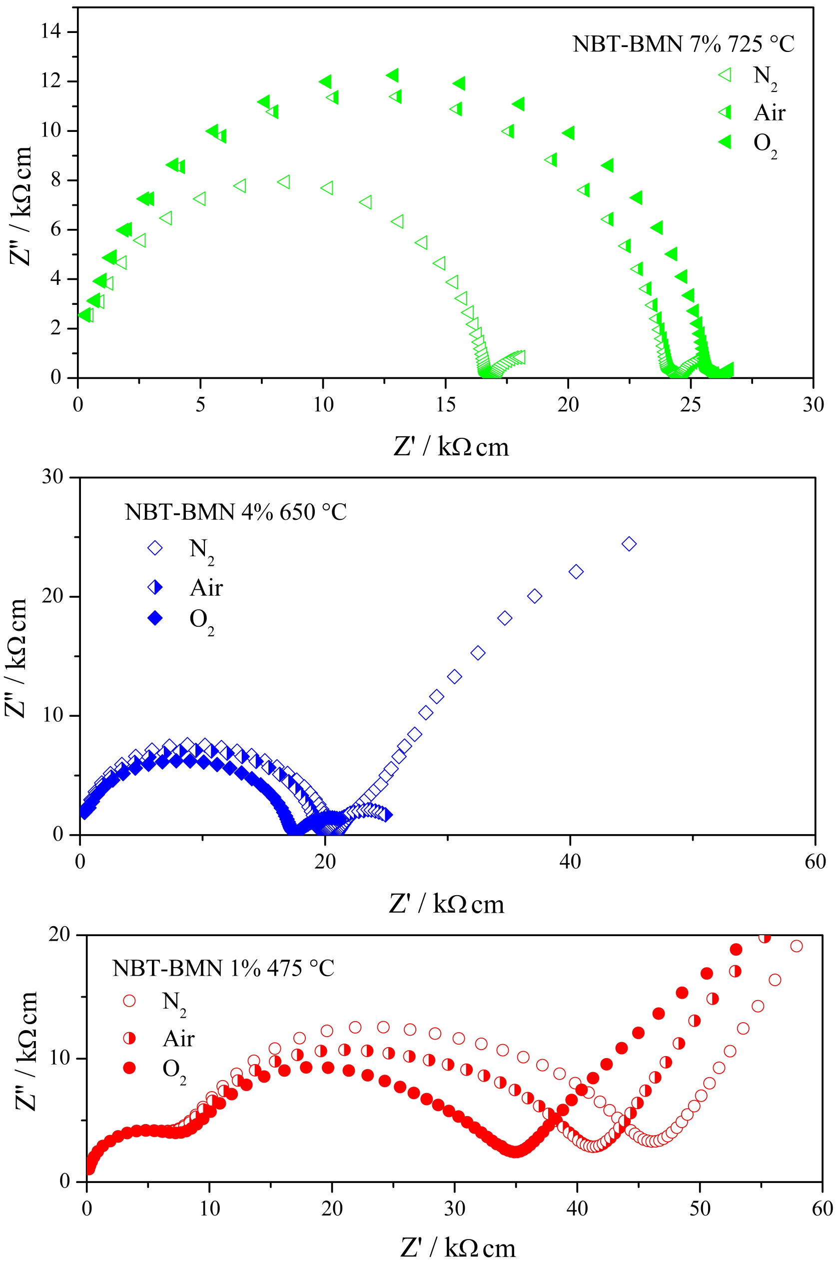

Figure 4.14: Examples of complex impedance plots for NBT-BMN 1% (bottom), 4% (middle) and 7% (top) under O_2, air and N_2.

of the p_{O_2} ($\sim 10\,\mathrm{k\Omega\,cm}$), the poorly resolved responses at lower frequencies become more conductive with increasing p_{O_2} (going from ∼46 to $\sim 35\,\mathrm{k\Omega\,cm}$ under N_2 and O_2, respectively) indicating that at least one of those responses represents p-type electronic conduction. It can also be appreciated that there is clearly a low frequency "spike", which could be due to a double layer capacitor formed from the blocking of mobile ions at the electrodes or the start of a Warburg response. In solid oxides, a Warburg response is associated with the diffusion of molecular oxygen to and from the electrodes as a consequence of oxygen reduction and evo-

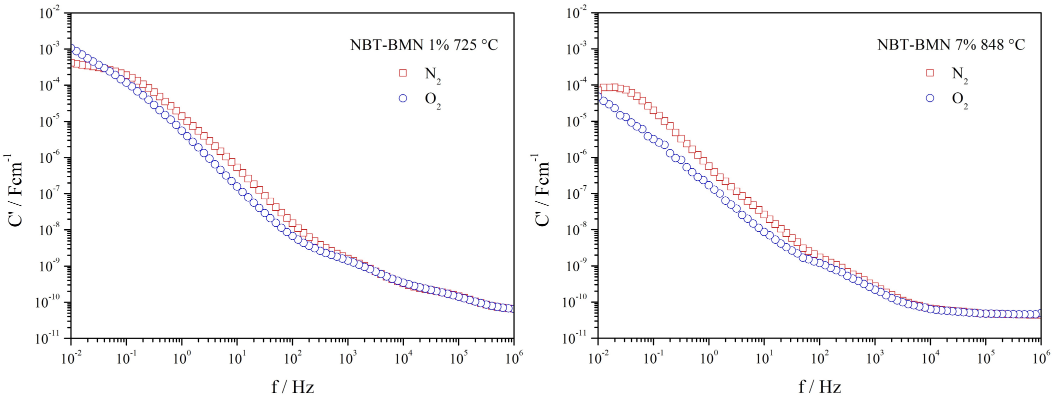

Figure 4.15: C' spectroscopic plots for NBT-BMN 1% at 725 °C (left) and 7% at 848 °C (right) under N_2 (red squares) and O_2 (blue cricles).

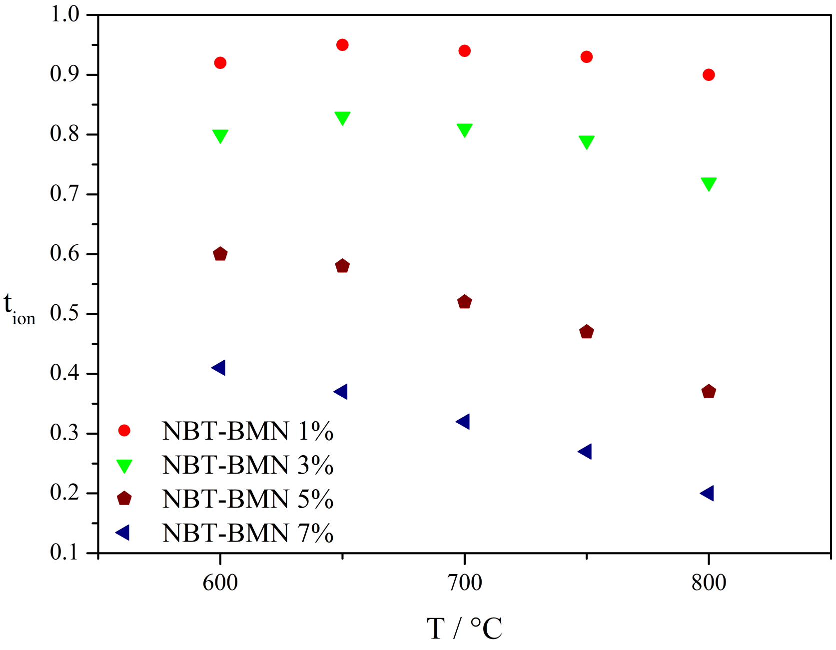

Figure 4.16: Oxide ion transport numbers of NBT-BMN.

lution reactions. On the other hand, for NBT-BMN 7% the bulk becomes less conductive with increasing p_{O_2}(from $\sim$17 $\mathrm{k\Omega\,cm}$ under N_2 to $\sim$26 $\mathrm{k\Omega\,cm}$ under O_2), this shows that the bulk in this sample has an n-type electronic contribution to its conductivity which could be attributed to partial reduction of Ti^{4+} to Ti^{3+} under low p_{O_2}. Figure 4.15 presents the C' spectroscopic plots for the 1 and 7 % samples under O_2 and N_2 at higher temperatures. The capacitance reaches values at low frequencies of the order of hundreds of microFarads per centimetre which indicate a redox process is occurring. In both cases, the C' data under N_2 reaches a plateau at low frequencies which indicates blocking electrodes, therefore there is ionic conduction in these samples. Oxide ion transport numbers estimated through electromotive force measurements under an oxygen concentration gradient for four NBT-BMN compositions are plotted in Figure 4.16. A clear drop of the t_{ion} is observed with increasing BMN concentration. The decrease in the bulk conductivity and its increasing dependence on p_{O_2} discussed above can be connected to the drop of t_{ion}. As the oxygen vacancies become trapped, the conductivity becomes increasingly dominated by the low intrinsic electronic component.

Interestingly, the conductivity decreases faster initially and then slower as the concentration increases compared against the case with BA. This might be related to the fact that the substitutional magnesium ions have twice the effective negative charge of aluminium ions in titanium sites, which might make them more effective traps at lower concentrations. In the literature discussed in Chapter 2 it is concluded that the trapping is stronger the larger the size mismatch between host and dopant [49, 51]. Given the radii [80] of the ions considered here (Ti^{4+}: $60.5\,\mathrm{pm}$, Al^{3+}: $53.5\,\mathrm{pm}$, Mg^{2+}: $72.0\,\mathrm{pm}$, Zn^{2+}: $74.0\,\mathrm{pm}$, Nb^{5+}: $64.0\,\mathrm{pm}$), aluminium would be expected to be the weakest trap since it has the smallest size difference with respect to titanium. However, this is not the case observed from comparing NBT-BA and NBT-BMN. A possible explanation based on the consideration that oxygen vacancies tend to associate with the smallest cation [81, 48] and since Al^{3+} is the only ion in this list smaller than the host, the oxygen vacancies in NBT-BA will be driven towards the acceptor dopant both by the size difference and the effective charges of the defects. Another option is to consider the higher oxygen-aluminium bond strength (see Table 4.1) makes Al^{3+} ions stronger traps.

Table 4.1: Metal-oxygen bond strengths in oxides estimated as described in Reference [82] (See Appendix B for details).

Oxide	$\Delta H_{M-O}(Ionic)$ / CN_O $(kJmol^{-1})$	$\Delta H_{M-O}(Neutral)$ / CN_O $(kJmol^{-1})$
MgO	640	166
ZnO	1007	182
Al_2O_3	1280	257
TiO_2	2004	319
Nb_2O_5	2572	392

4.2.2 $Na_{0.5}Bi_{0.5}TiO_3$-$BiZn_{2/3}Nb_{1/3}O_3$

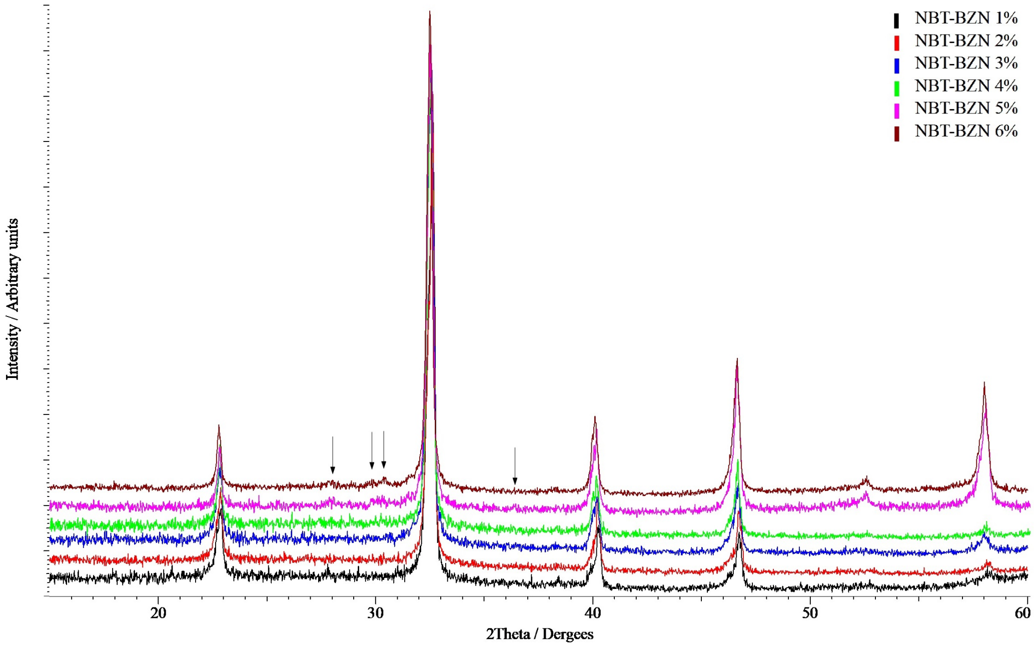

Figure 4.17: XRD patterns for NBT-BZN pellets sintered at 1150 °C for two hours.

(1-x)$Na_{0.5}Bi_{0.5}TiO_3$-x$BiZn_{2/3}Nb_{1/3}O_3$ ceramics were prepared using the same procedure as for NBT-BMN discussed above. XRD patterns for the sintered pellets (which have densities around 94%) of NBT-BZN compositions up to 6% are shown in Figure 4.17, some additional peaks arising from secondary phases can be appreciated. XRD patterns of the calcined powders were used to better identify these phases in Figure 4.18. The $Na_{0.5}Bi_{4.5}Ti_4O_{15}$ Aurivillius phase is detected from 4% BZN alongside small amounts of ZnO. From 5% onwards, the $BiZn_{2/3}Nb_{4/3}O_7$ pyrochlore is observed as well and its peaks become significantly more intense with increasing BZN content. Furthermore, as shown in Figure 4.19, the increase in cell volume (obtained in the same manner as those for NBT-BMN) is lower for the NBT-BZN system than for the NBT-BMN system even though the ionic radius of Zn^{2+} (74 pm) is larger than that of Mg^{2+} (72 pm), suggesting that the zinc is not incorporating into the structure (at least not as much as magnesium does). The solid solution limit for NBT-BZN being low compared against the magnesium analogue might be due to competition with the pyrochlore phase or to the introduction of Zn^{2+} into NBT being unfavourable, which would be expected considering the study made by Urban *et al.* where they find that distortions of the coordination octahedra significantly increase relative energy of the d bands for d^{10} ions in oxides [83].

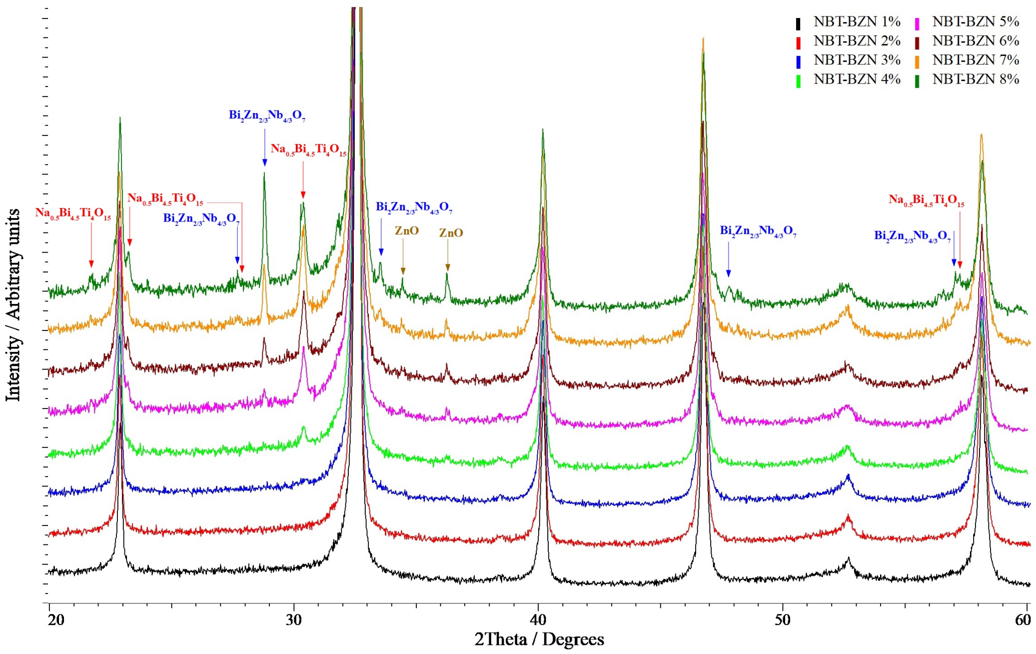

Figure 4.18: XRD patterns for NBT-BZN powders calcined twice at 800 °C for two hours.

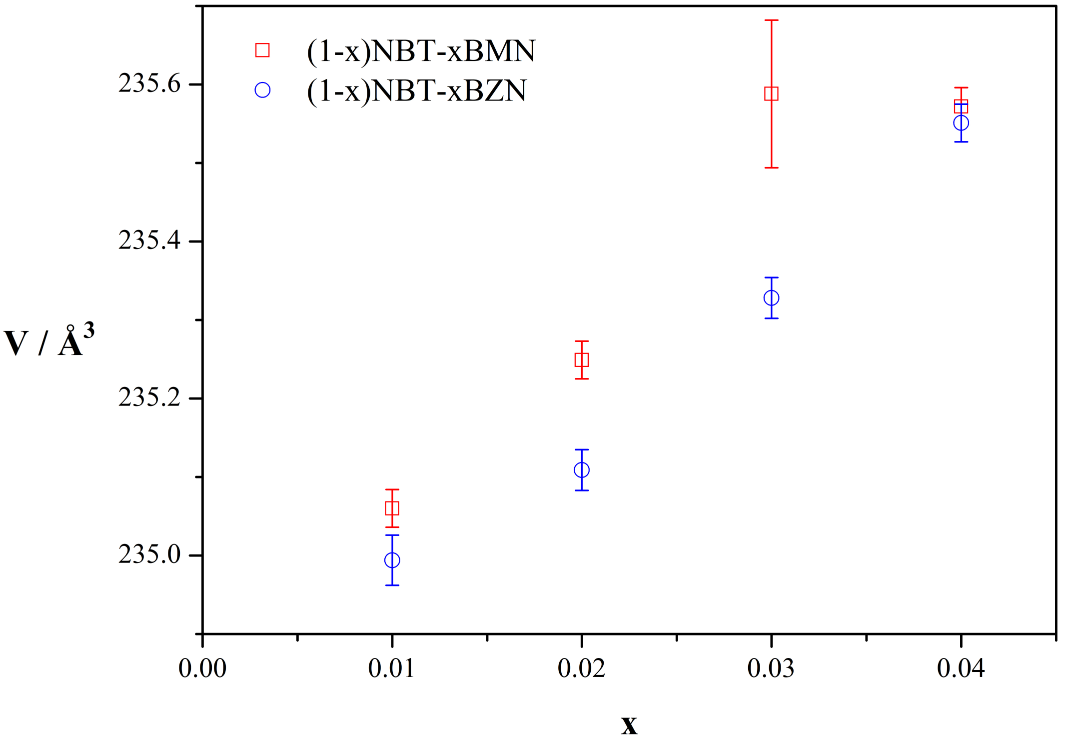

Figure 4.19: Cell volume of NBT-BZN and NBT-BMN crushed pellets. The error bars shown correspond to 2σ.

Figure 4.20 shows secondary and backscattered electron images of the polished surfaces of NBT-BZN pellets. The most noticeable feature is in the backscattered image of the NBT-BZN 4% pellet where a secondary phase can be clearly detected as a brighter region (circled in red),

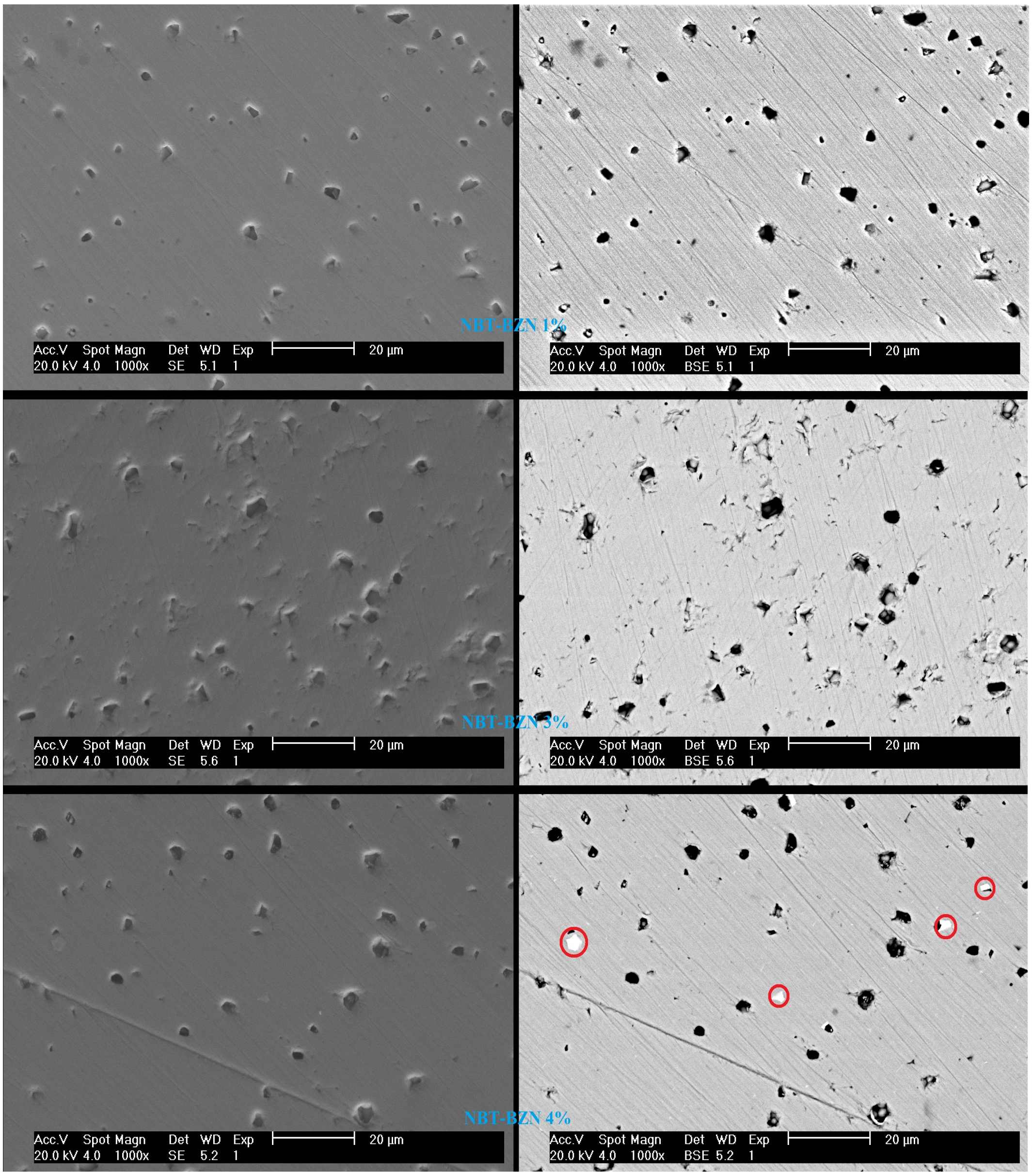

Figure 4.20: Secondary electron (left) and back-scattered electron (right) images of the polished pellet surfaces of NBT-BZN 1, 3 and 4 %.

based on the EDS quantification (normalising the Bi content: $Na_{0.48}Bi_{4.5}Ti_{3.67}Zn_{0.11}Nb_{0.12}O_{14.75}$) these could be attributed to the $Na_{0.5}Bi_{4.5}Ti_4O_{15}$ Aurivillius phase detected in XRD, strongly suggesting that the solid solution limit is below 4% BZN. Figure 4.21 presents the EDS results from the main phase of polished pellets of NBT-BZN. The overlap of the Zn and Nb peaks with those from Na and Bi, respectively, alongside the very low concentrations leads to relatively high uncertainties, which prevent these data from helping establish if the zinc is incorporated into the structure or not. From the XRD data and the SEM images it can be concluded that the system is following a different mechanism than the nominal one. NBT is probably in-

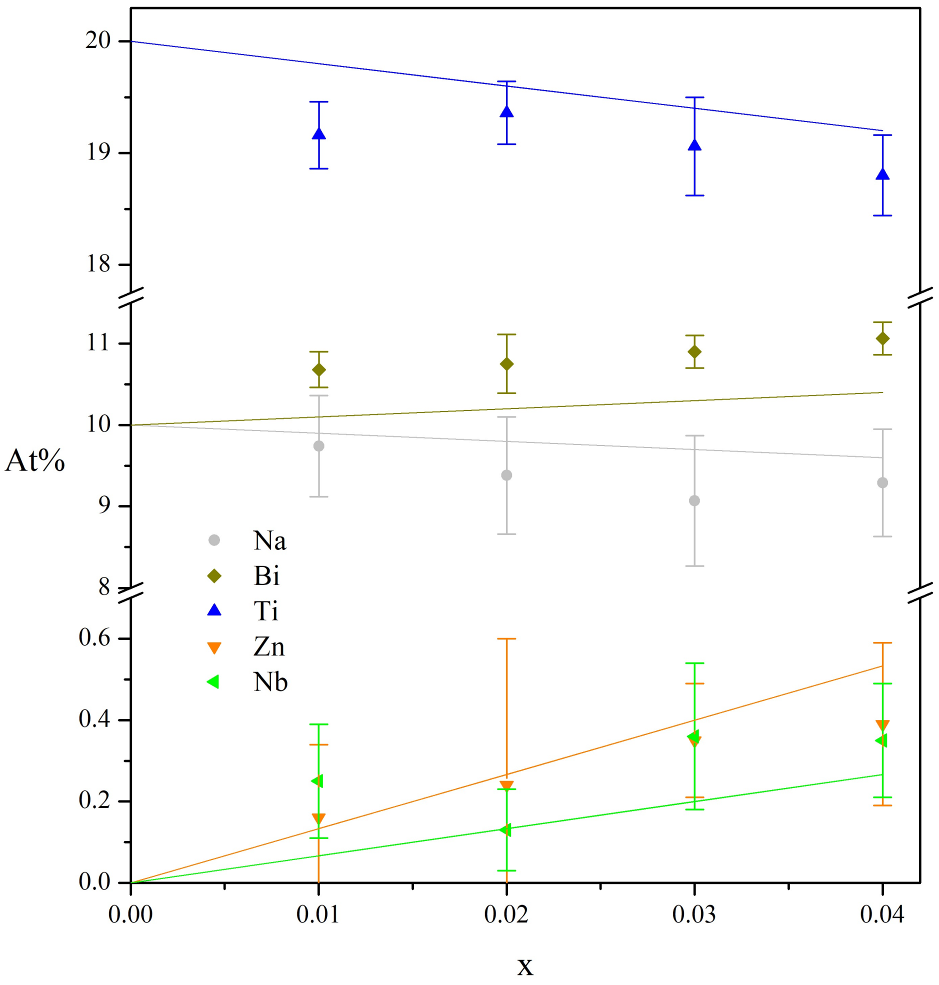

Figure 4.21: Atomic percentages obtained from EDS spectra on polished pellets of NBT-BZN. The solid lines correspond to the amounts expected from the nominal compositions. The error bars shown represent 2 standard deviations.

corporating the niobium preferentially into its structure which accounts for the faster drop in conductivity compared to BMN, and the excess bismuth forms the Aurivillius phase and at higher concentrations the $BiZn_{2/3}Nb_{4/3}O_7$ pyrochlore with the unreacted ZnO.

The temperature profiles for the permittivity and dielectric loss obtained from dielectric measurements are presented in Figure 4.22. Once again there is little change in terms of the permittivity-temperature profile, but the dielectric loss decreases with increasing BZN content in a faster manner than the cases with BMN (see Figure 4.23) or BA discussed earlier. Figure 4.24 shows examples of impedance spectra for this series up to 4%. The 2% BZN composition, where two poorly resolved responses are observed (similarly to the 4% BMN sample in Figure 4.10), is used as an example for the 1 and 2% compositions as well as 3% at low temperatures. The 4% case also exemplifies the 3% sample at higher temperatures where a single

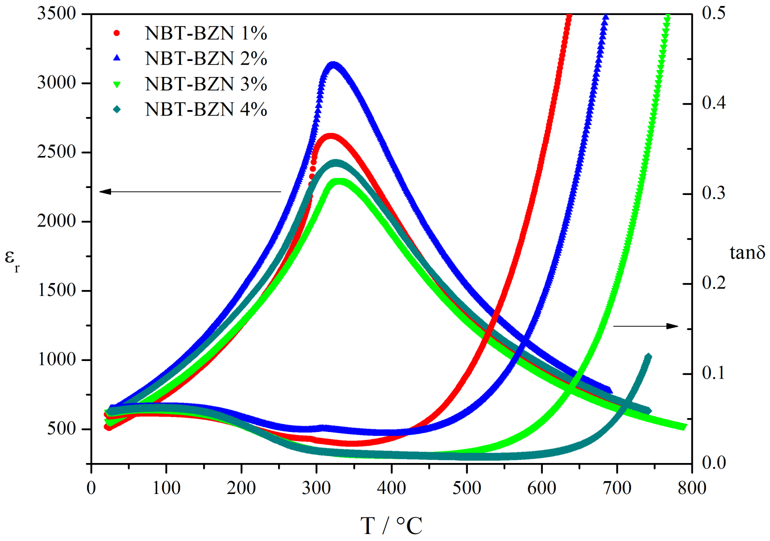

Figure 4.22: Temperature profiles for the permittivity and dielectric loss of NBT-BZN solid solutions on heating at 1 MHz.

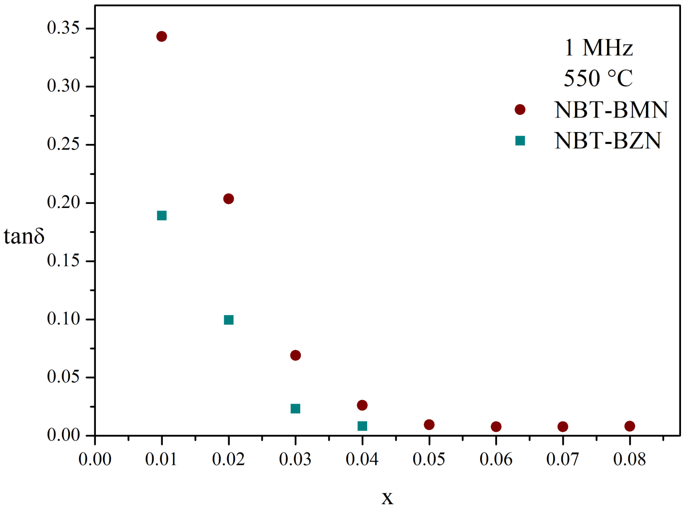

Figure 4.23: Dielectric loss at 1 MHz and 550 °C against doping level for NBT-BMN and NBT-BZN.

arc is obtained, as seen for 7% NBT-BMN in Figure 4.10. Figure 4.25 presents the extracted permittivities for these samples, which are also consistent for bulk NBT. Figure 4.26 plots the corresponding bulk conductivities in the form of an Arrhenius plot. As shown in Figure 4.27, the conductivity in this solid solution decreases much faster than in the NBT-BMN or NBT-BA cases and becomes insulating by 4% BZN which could suggest that zinc is a stronger trap for the oxygen vacancies; however this is already past the solid solution limit. If not all the Zn^{2+} ions are incorporated into the perovskite, then it might be the bismuth excess or the donor character of Nb^{5+} (see Equation 2.2 in Chapter 2) that actually cause the drop in conductivity [40].

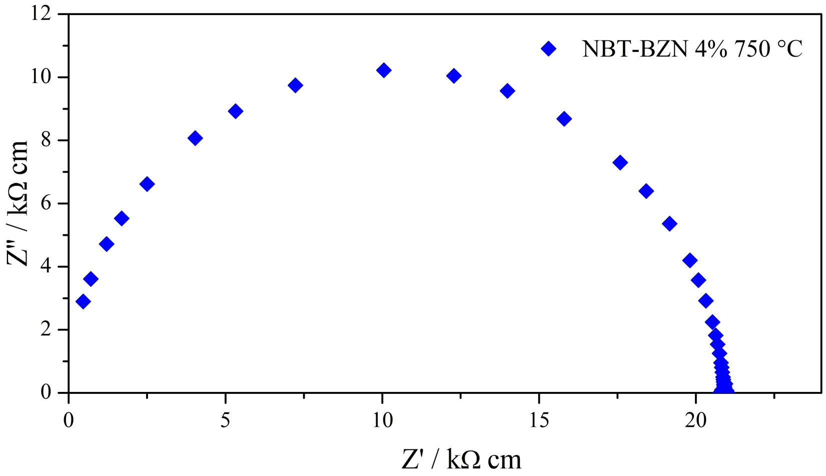

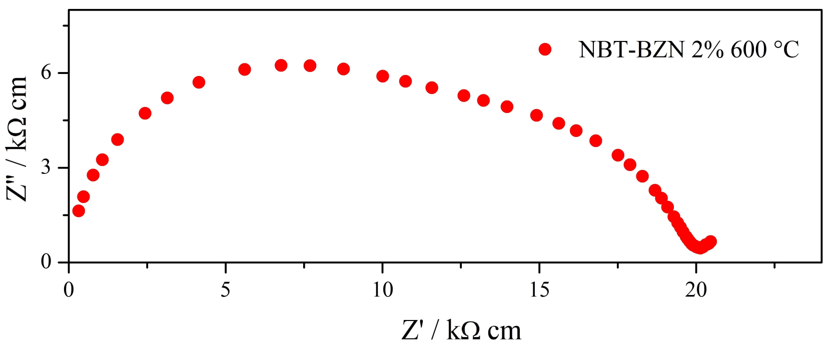

Figure 4.24: Complex impedance plots for NBT-BZN 2% at 600 °C and 4% at 750 °C.

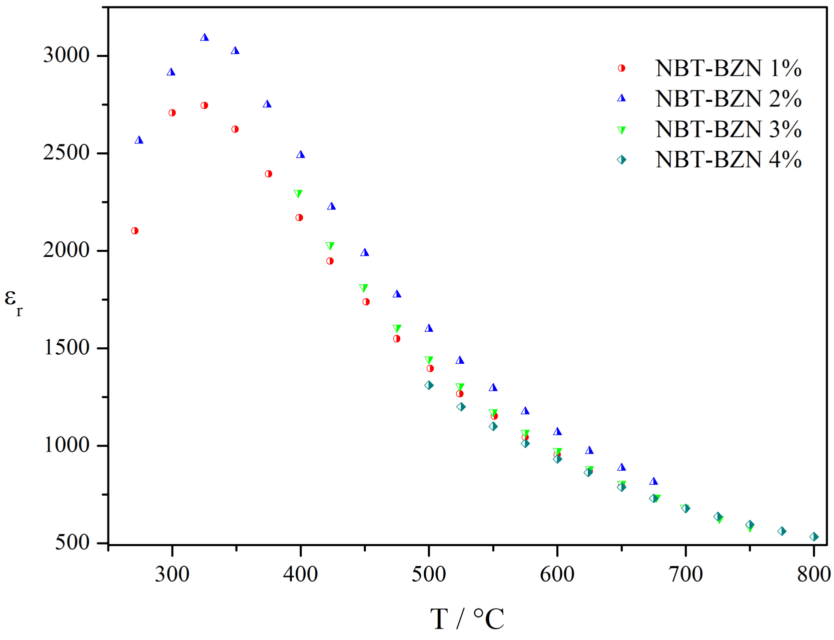

Figure 4.25: Permittivities extracted from M” peaks for NBT-BZN solid solution.

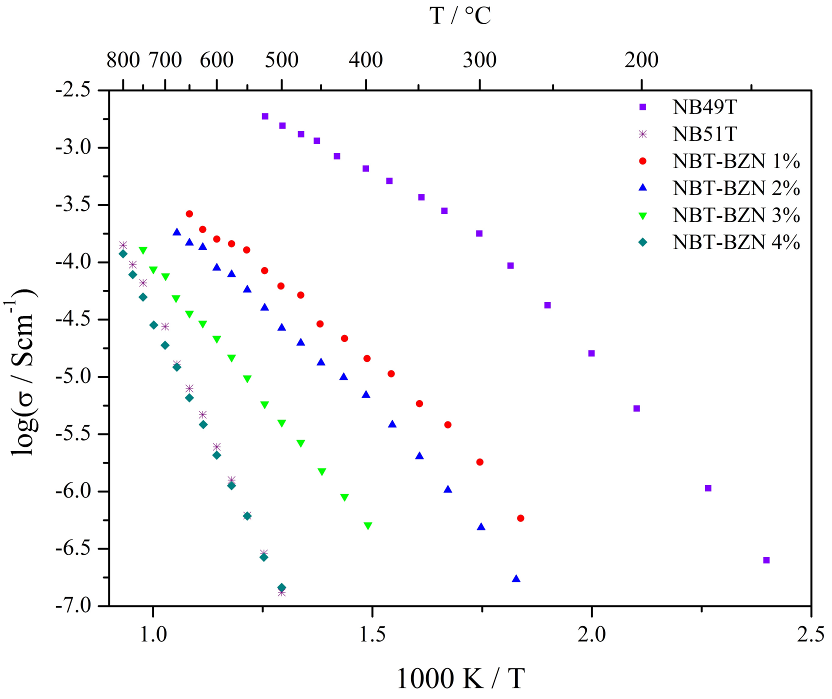

Figure 4.26: Arrhenius plot for bulk conductivities of NBT-BZN compositions from 1 to 4%.

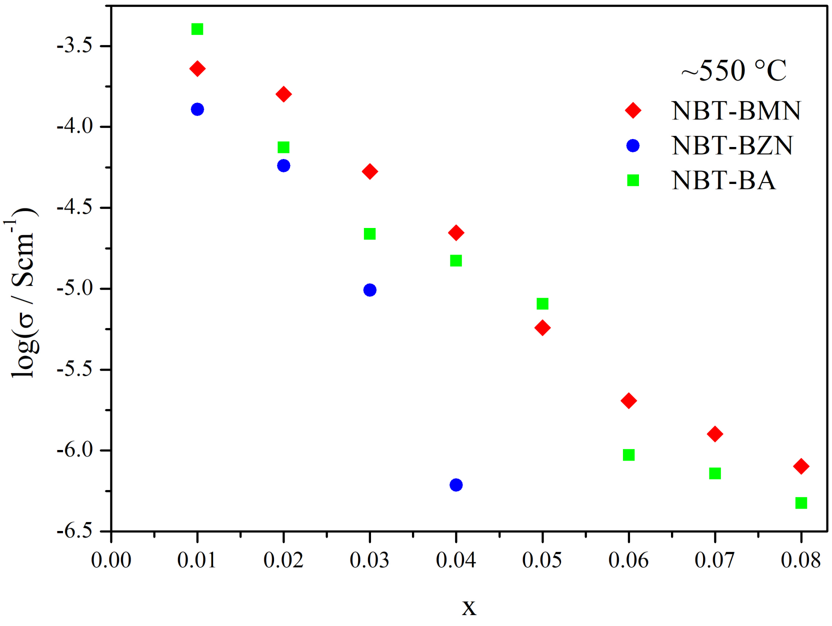

Figure 4.27: Bulk conductivities of NBT-BA (data from Reference [14]), NBT-BMN and NBT-BZN compositions at 550 °C.

4.3 Conclusions

The change in cell volume presented in Figure 4.4 indicates an NBT-BMN solid solution can form. EDX results in Figure 4.6 suggest the solid solution limit is probably between 6 and 7% BMN. Similarly to the solid solution with BA reported in the literature, NBT-BMN exhibits a gradual decrease of the oxide ion conduction evidenced in Figure 4.16 which then leads to the bulk conductivity in Figure 4.12 being lowered with increasing dopant concentration. This has a strong impact on the dielectric loss but very little effect on the permittivity-temperature profiles presented in Figure 4.8. Perhaps due to its higher effective negative charge, magnesium seems to be a more effective trap at low concentrations than aluminium, but at higher concentrations the stronger metal-oxygen bond for aluminium reverses the initial trend. Additionally, the presence of an additional component (MgO and Nb_2O_5 compared against Al_2O_3) makes the NBT-BMN system less appealing for application compared against NBT-BA .

On the other hand, in the case of the NBT-BZN system, the XRD patterns (Figure 4.18) and SEM images (Figure 4.20) indicate a solubility limit below 4% BZN (if the nominal mechanism occurs), resulting in a niobium-doped bulk which causes the dramatic drop in conductivity observed in Figure 4.26. This lower solubility limit (which means the nominal mechanism in Equation 4.1 is unlikely to be the preferred mechanism) is probably related to octahedral distortions (expected in this type of disordered material) being unfavourable for d^{10} ions [83] and competition with the $BiZn_{2/3}Nb_{4/3}O_7$ pyrochlore. $BiZn_{2/3}Nb_{4/3}O_7$ is expected to be more stable than its magnesium analogue since pyrochlores tend to be favoured over perovskites when both A- and B-site ions are less electropositive [84].

More systems would need to be explored in order to draw conclusions about the trapping strengths of acceptors in NBT, as in this work only aluminium and magnesium can be compared. NBT-$BiZn_{0.5}Ti_{0.5}O_3$ and NBT-$BiMg_{0.5}Ti_{0.5}O_3$ solid solutions would be very useful to complete this study.

Chapter 5

$Na_{0.5}Bi_{0.5}TiO_3-NaNbO_3$

5.1 Introduction

$NaNbO_3$ (NN) is an intensely studied perovskite since it is a parent compound in many potential antiferroelectrics for application in energy storage as well as in promising Pb-free piezoelectrics (mainly based on $K_{0.5}Na_{0.5}NbO_3$) [85]. This compound is well known for its remarkably complex polymorphism. Several polymorphs have been reported in the literature (seven are widely accepted to exist) with varying transition temperatures and sequences [86, 87]. The polymorphism of NN has been shown to be dependent on the thermal history, synthesis method and particle size of the sample [88, 89]. The identification of the polymorphs and their structural characterisation has been considered to be challenging and has been tackled with several different techniques (and revisited over the years as the techniques develop further) due to the strong similarities between the polymorphs and the possibility of phase coexistence [90]. It is (usually) an antiferroelectric orthorhombic perovskite at room temperature but it can transform into a ferroelectric polymorph (also orthorhombic) under an electric field. The dielectric constant presents a small peak ($\sim$400) between 90 and 160 °C attributed to the transition between the antiferroelectric and ferroelectric states in some articles and a larger peak ($>$1600) between 300 and 400 °C corresponding to the transition to the paraelectric state [91, 92, 93]. Adding to the complexity of working with undoped NN is the fact that it is difficult to sinter by conventional means. This occurs because surface diffusion is activated at lower temperatures than other mechanisms in NN, resulting in a reduction of the curvature of the necks that lowers the driving force for other mechanisms that would be densifying, therefore grain growth occurs with poor densification [94].

Solid solutions between NBT and NN have been reported as potential lead-free piezoelectrics, where the dielectric losses are lowered with respect to undoped NBT and the piezoelectric properties improved at low NN concentrations [95]. It has also been reported that the Curie temperature decreases with increasing NN content, as well as the remnant polarisation and coercive field until the system is no longer ferroelectric at room temperature [96, 11]. Most of the literature on NBT-NN is focused on the NBT-rich end (under 10% NN), even though a morphotropic phase boundary is reported (based on XRD) at 90-92% NN [95]. This might be because dense ceramics are difficult to make in the NN-rich end of the system.

Xu *et al.* report solid solutions up to 35% NN and, based on Rietveld refinements of XRD patterns, the stabilisation of the tetragonal ($P4bm$) perovskite. They report that with 5% NN the fraction of $P4bm$ polymorph is 60% which increases until it is the only phase detected at room temperature above 25% NN. This is accompanied by a remarkable flattening of the temperature profiles of the permittivity and the transition from a ferroelectric to a paraelectric [11]. In another article [97], Xu *et al.* study the energy storage characteristics of $(1-x)$(0.92NBT-0.08$BaTiO_3$)-xNN ceramics and reported an optimum at 10% NN with an energy density of $0.71\ \mathrm{J\,cm^{-3}}$ at $7\ \mathrm{kV\,mm^{-1}}$ and 10 Hz. They also report good temperature stability up to $150\ ^{\circ}\mathrm{C}$.

The complex polymorphism of NBT is considered partly responsible for the temperature dependence of its conductivity and the Na/Bi ratio has been observed to be relevant for determining the dominating conduction mechanism, $Na_{0.5}Bi_{0.49}TiO_{2.985}$ (NB49T) exhibits high oxide ion conductivity and $Na_{0.5}Bi_{0.51}TiO_{3+\delta}$ (NB51T) has low (predominantly electronic) conductivity. Therefore solid solutions between NBT and NN where the temperature ranges for the stability of each polymorph are changing present an interesting system to study. Furthermore, comparing the electrical behaviour of solid solutions between NBT and bismuth-based perovskites with that of solid solutions with sodium-based perovskites might provide useful information about the role each A-site ion plays.

5.2 Results

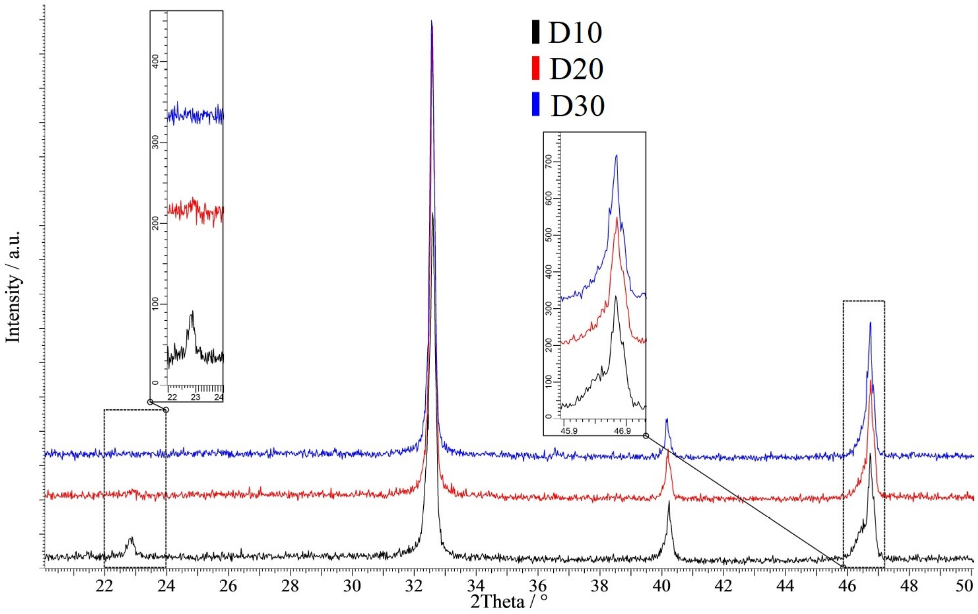

Figure 5.1: XRD patterns for sintered pellets of D10, D20 and D30.

Table 5.1: Prepared NBT-NN compositions.

Series	Sample	Nominal composition
NB49T-NN	D5	$Na_{0.525}Bi_{0.465}Ti_{0.950}Nb_{0.050}O_{2.985}$
	D10	$Na_{0.550}Bi_{0.440}Ti_{0.900}Nb_{0.100}O_{2.985}$
	D15	$Na_{0.575}Bi_{0.415}Ti_{0.850}Nb_{0.150}O_{2.985}$
	D20	$Na_{0.600}Bi_{0.390}Ti_{0.800}Nb_{0.200}O_{2.985}$
	D25	$Na_{0.625}Bi_{0.365}Ti_{0.750}Nb_{0.250}O_{2.985}$
	D30	$Na_{0.650}Bi_{0.340}Ti_{0.700}Nb_{0.300}O_{2.985}$
NBT-NN	S10	$Na_{0.55}Bi_{0.45}Ti_{0.90}Nb_{0.10}O_3$
	S20	$Na_{0.60}Bi_{0.40}Ti_{0.80}Nb_{0.20}O_3$
	S30	$Na_{0.65}Bi_{0.35}Ti_{0.70}Nb_{0.30}O_3$
NB51T-NN	R10	$Na_{0.55}Bi_{0.46}Ti_{0.90}Nb_{0.10}O_{3.015}$
	R20	$Na_{0.60}Bi_{0.41}Ti_{0.80}Nb_{0.20}O_{3.015}$
	R30	$Na_{0.65}Bi_{0.36}Ti_{0.70}Nb_{0.30}O_{3.015}$

The mixed reactants were calcined for two hours at 800 °C in alumina crucibles. The re-milled calcined powders were pressed into pellets, buried in sacrificial powder and sintered at 1170 °C for two hours. Based on their dimensions, the pellets obtained have densities around 94 $\sim$ 97 %. Figure 5.1 shows XRD patterns for three pellets of solid solutions between NBT and NN that are deliberately bismuth deficient (NB49T-NN), the insets highlight areas of interest to identify different polymorphs. Nominally stoichiometric (NBT-NN) and bismuth-excess

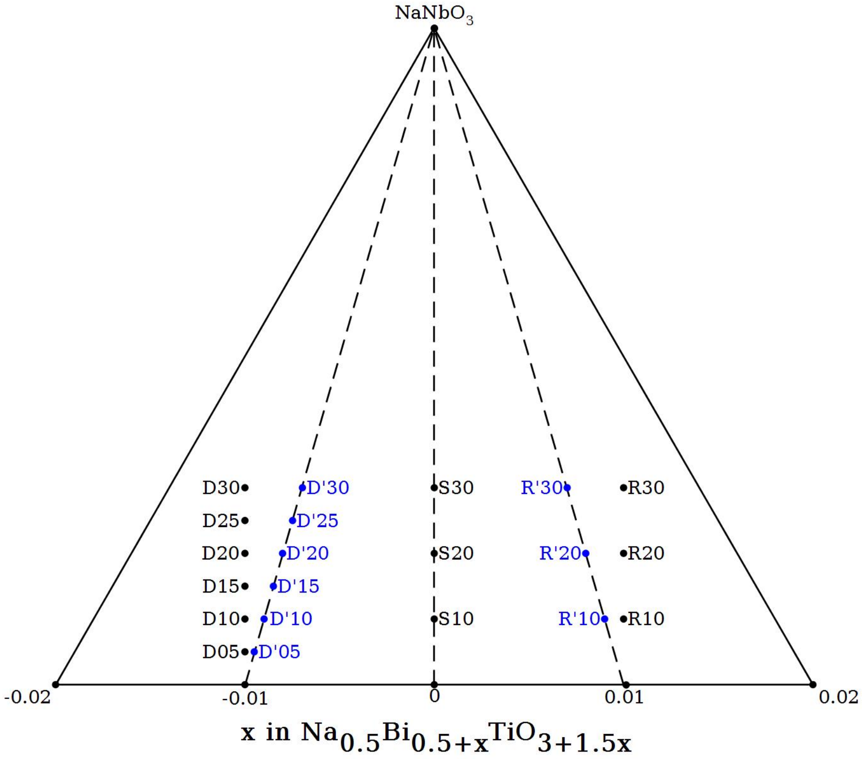

Figure 5.2: Phase diagram illustrating the nominal compositions for the prepared NBT-NN samples (D, S and R series in black dots) and the position of the compositions without an adjustment to Bi_2O_3 content (D' and R' series in blue dots).

(NB51T-NN) series were also prepared. For the NB49T-NN and NB51T-NN series a small adjustment in the bismuth content was made to maintain the same nominal oxygen content (i.e. $Na_{0.5(1+x)}Bi_{0.49-0.5x}Ti_{1-x}Nb_xO_{2.985}$ instead of $Na_{0.5(1+x)}Bi_{0.49(1-x)}Ti_{1-x}Nb_xO_{2.985+0.015x}$). The nominal compositions prepared are illustrated in Figure 5.2 where black dots represent the compositions used (D, S and R series) and blue dots the compositions without the adjustment to the bismuth content (D' and R' series) and listed in Table 5.1. Figure 5.3 presents the change in cell volume with NN content obtained from Rietveld refinements as described in Chapter 3 (Appendix C contains more details) from crushed pellets with an internal silicon standard (NIST SRM 640e) using spacegroup Cc for NN concentrations up to 15 % and $Pnma$ for higher concentrations.

Figure 5.4 presents a closer inspection of higher quality XRD data for D30 (collected on a high resolution STOE STADI-P diffractometer using Cu $K_{\alpha 1}$ radiation and a linear position sensitive detector) where the peak positions predicted for the Cc and $P4bm$ polymorphs are marked. A few peaks that neither polymorph accounts for (marked with arrows) can be observed. Figure 5.5 shows the same data with markers corresponding to the $Pnma$ structure which can account for all peaks.

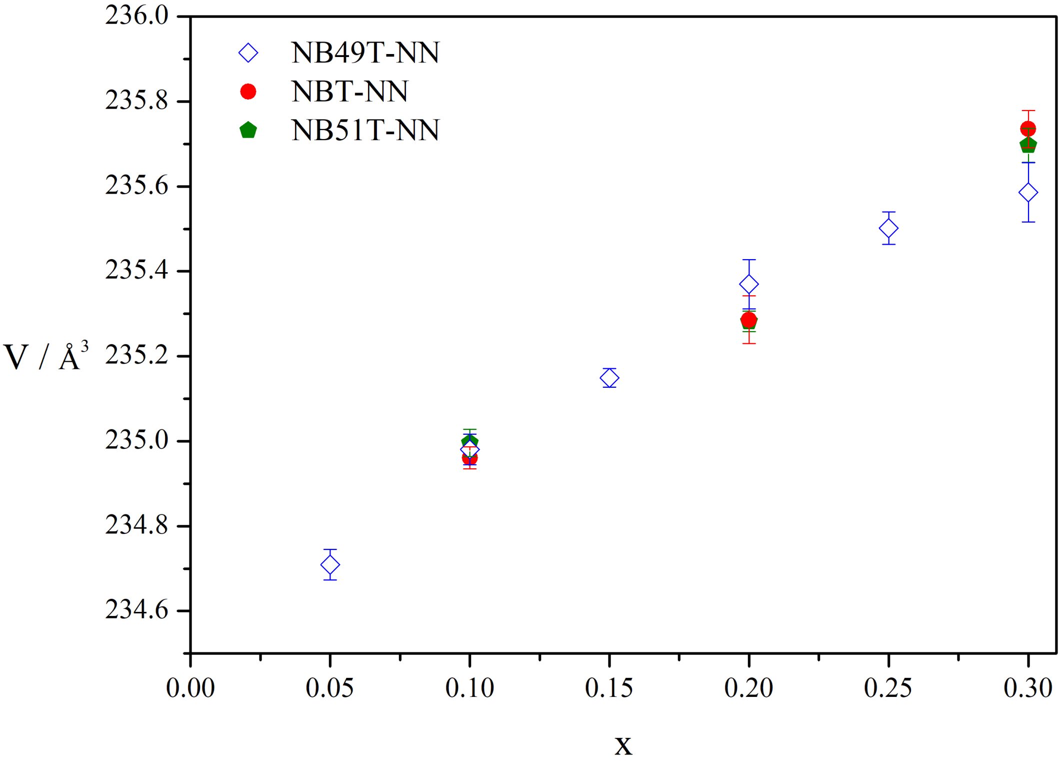

Figure 5.3: Cell volume of NBT-NN crushed pellets. The error bars shown correspond to 2σ.

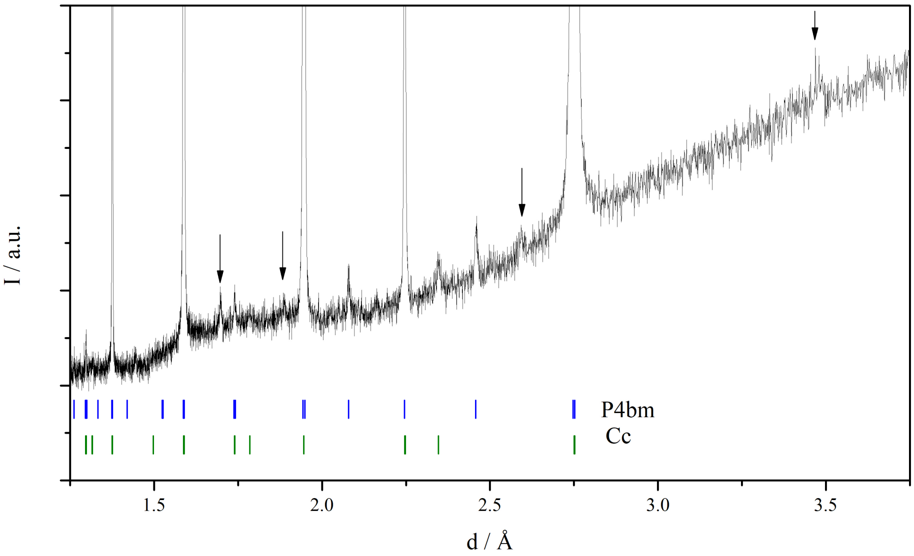

Figure 5.4: XRD pattern for D30. Peaks that can be indexed using space group $P4bm$ have blue markers underneath and green markers correspond to space group Cc.

To better study how the polymorphism changes with increasing NN content, neutron diffraction patterns were collected on POLARIS at ISIS for annealed crushed pellets of R10 and R20 between room temperature and 600 °C with 50 °C intervals from 50 to 650 °C as well as for D30 between 4.2 K and 600 °C with 50 K intervals from 25 to 225 K, 50 °C intervals from 100 to 300 °C and 100 °C intervals from 300 to 600°C with additional measurements at 4.2 K and room temperature. A comparison of the room temperature and 4.2 K data for D30 is shown in Figure 5.6 where no significant change of the relative intensities of the peaks in the patterns is appreciated. Figure 5.7 displays the evolution of the patterns for each sample with increasing temperature, focusing on the peaks labeled with ”M” and ”T”, two main features will be discussed later: the different relative intensities of the ”M” and ”T” peaks at room temperature

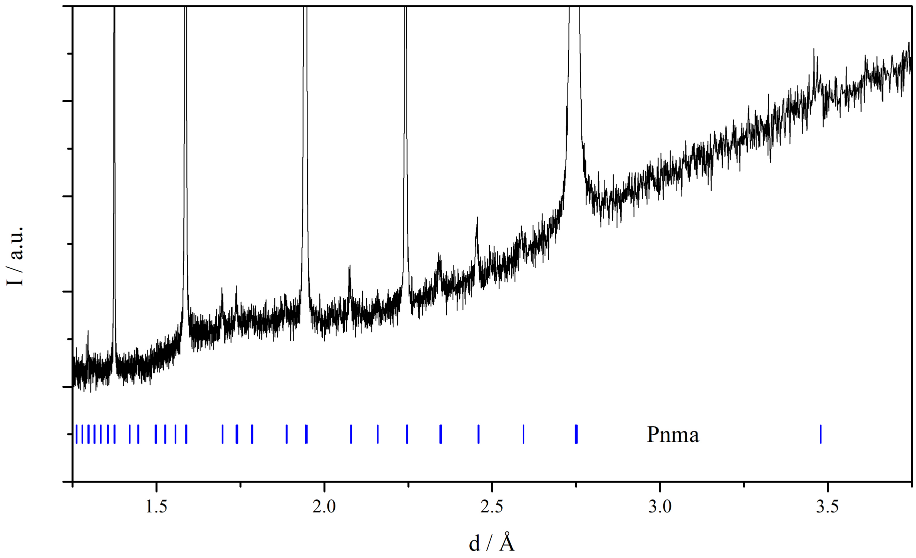

Figure 5.5: XRD pattern for D30. Blue markers indicate peaks that can be indexed using space group $Pnma$.

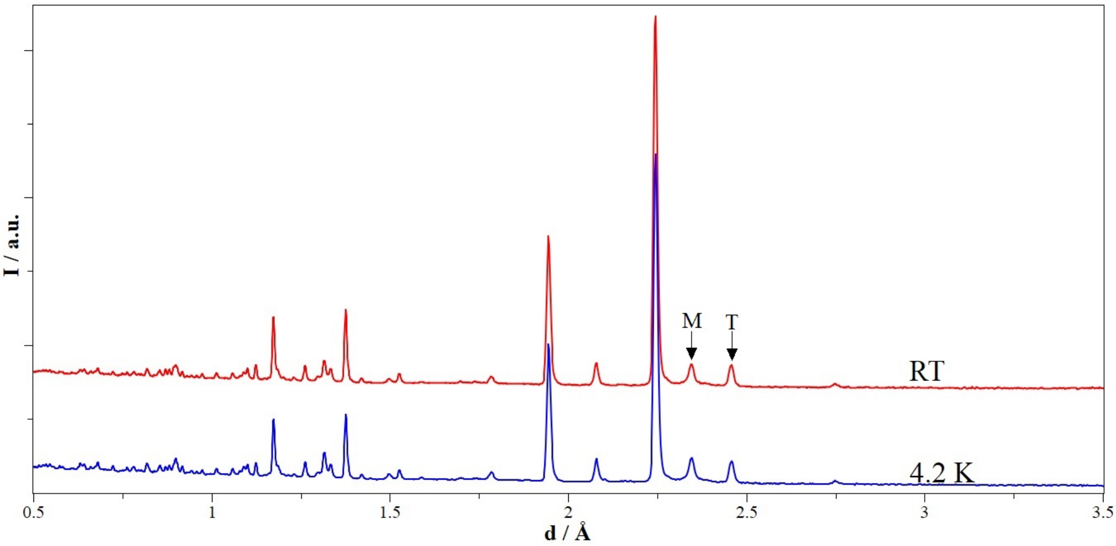

Figure 5.6: ND patterns from the 90 ° detector at RT and 4.2 K for annealed crushed pellets of D30. The ”M” and ”T” labels mark, respectively, a peak attributable to the low symmetry (Cc) and the tetragonal ($P4bm$) phases.

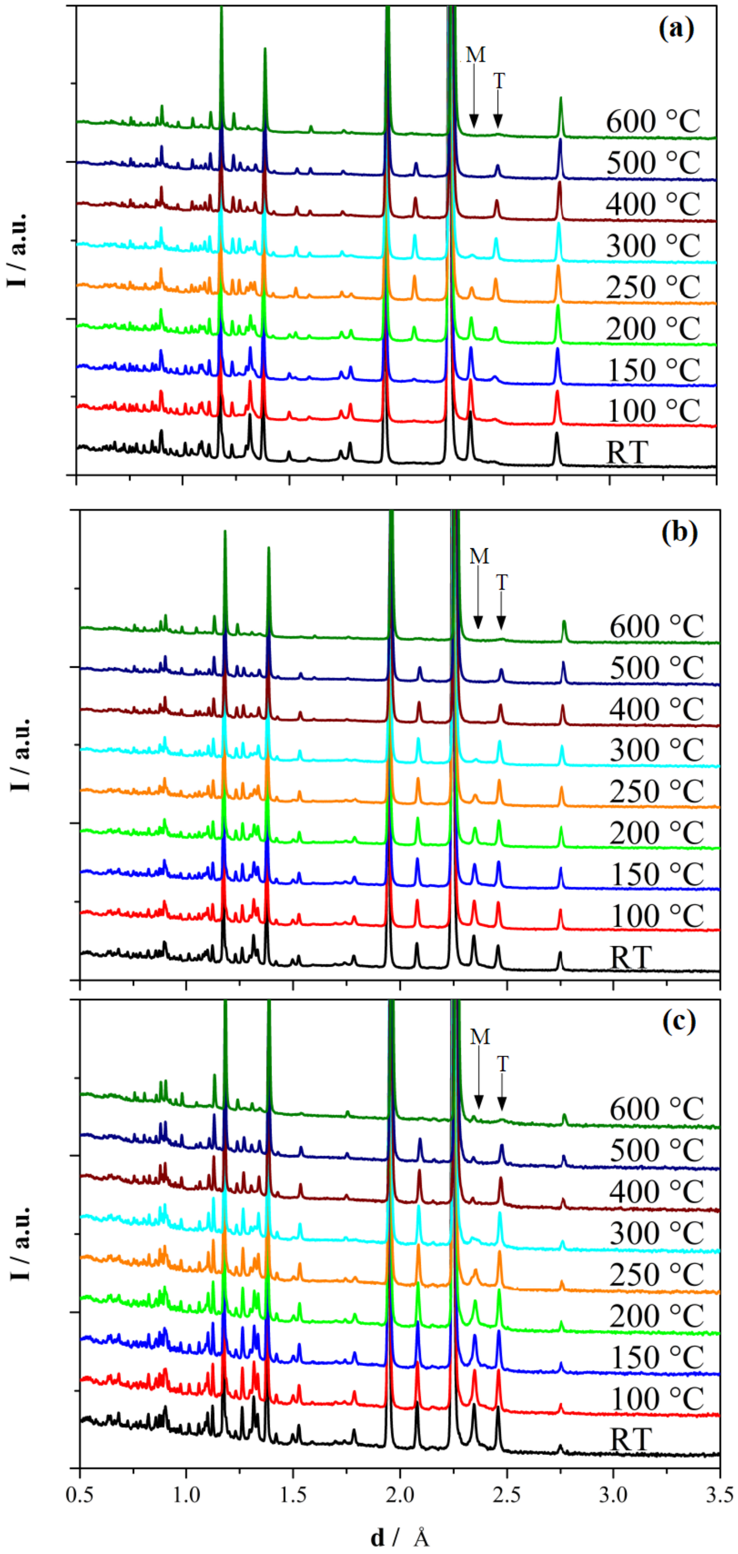

Figure 5.7: ND patterns from the 90 ° detector bank at selected temperatures for annealed crushed pellets of: a) R10 b) R20 c) D30. The "M" and "T" labels mark, respectively, a peak attributable to the low symmetry (Cc) and the tetragonal ($P4bm$) phases.

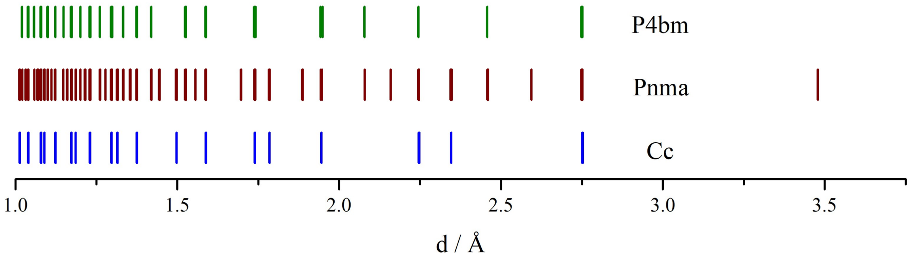

Figure 5.8: Markers for peak positions predicted for space groups Cc, $Pnma$ and $P4bm$.

for each composition and the similar evolution of the patterns from 250 to 600 °C. Figure 5.8 compares predicted peak positions for monoclinic (Cc), orthorhombic ($Pnma$) and tetragonal ($P4bm$) polymorphs of NBT highlighting how peaks from the monoclinic (Cc) and tetragonal ($P4bm$) phases could overlap with peaks from the orthorhombic ($Pnma$) phase complicating the analysis of diffraction data. Unfortunately, Rietveld refinements to obtain phase fractions as a function of temperature could not be made satisfactorily. An example is presented in Appendix D.

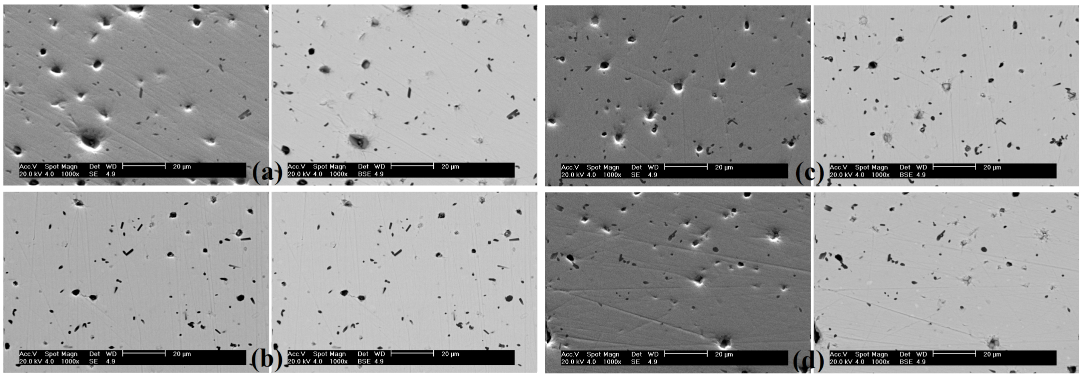

Figure 5.9: Secondary electron (left) and backscattered electron (right) micrographs from the polished surfaces of NB49T-NN pellets: a) D05 b) D10 c) D20 and d) D30.

Figure 5.9 presents micrographs for polished surfaces of some compositions in the NB49T-NN series and Figure 5.10 the quantitative analysis obtained through EDX which shows good agreement with the starting composition. Additionally, Figure 5.11 consists of micrographs from thermally etched pellets of select compositions across the S and D series, showing that grain sizes are similar (roughly 10 ∼ 20 µm) between both series and with changing NN content. The thermal etching seems to have caused a partial decomposition of the surfaces which have more secondary phases than the corresponding polished surfaces, this is the reason why the D15 composition is presented instead of D10 in which the decomposition did not allow to appreciate the grains of the main phase.

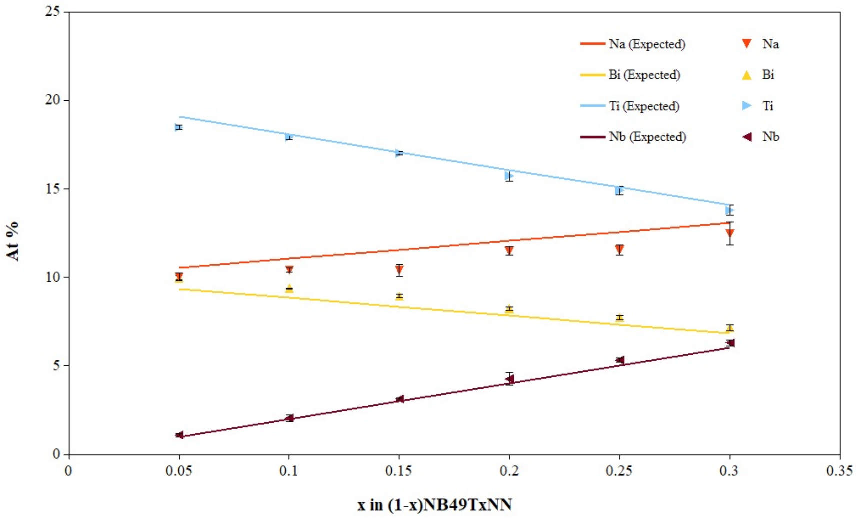

Figure 5.10: Cation contents in NB49T-NN solid solutions obtained from EDX.

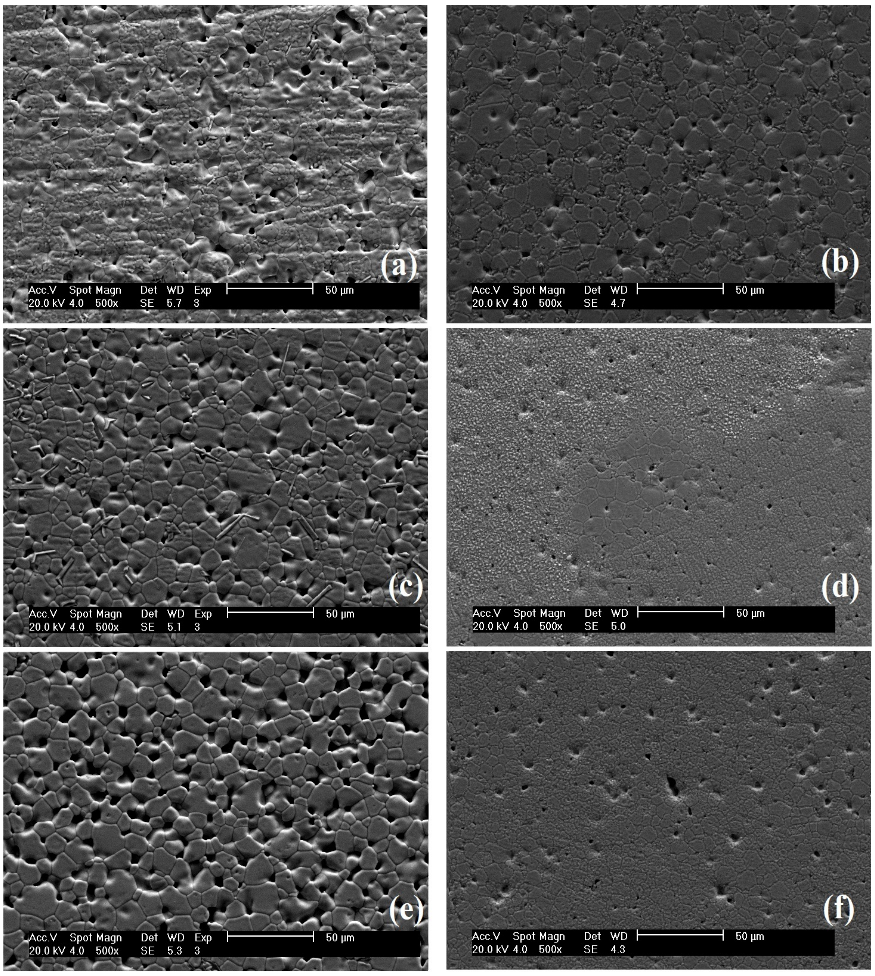

Figure 5.11: Secondary electron micrographs from thermally etched pellets of: a) S10 b) D15 c) S20 d) D20 e) S30 and f) D30.

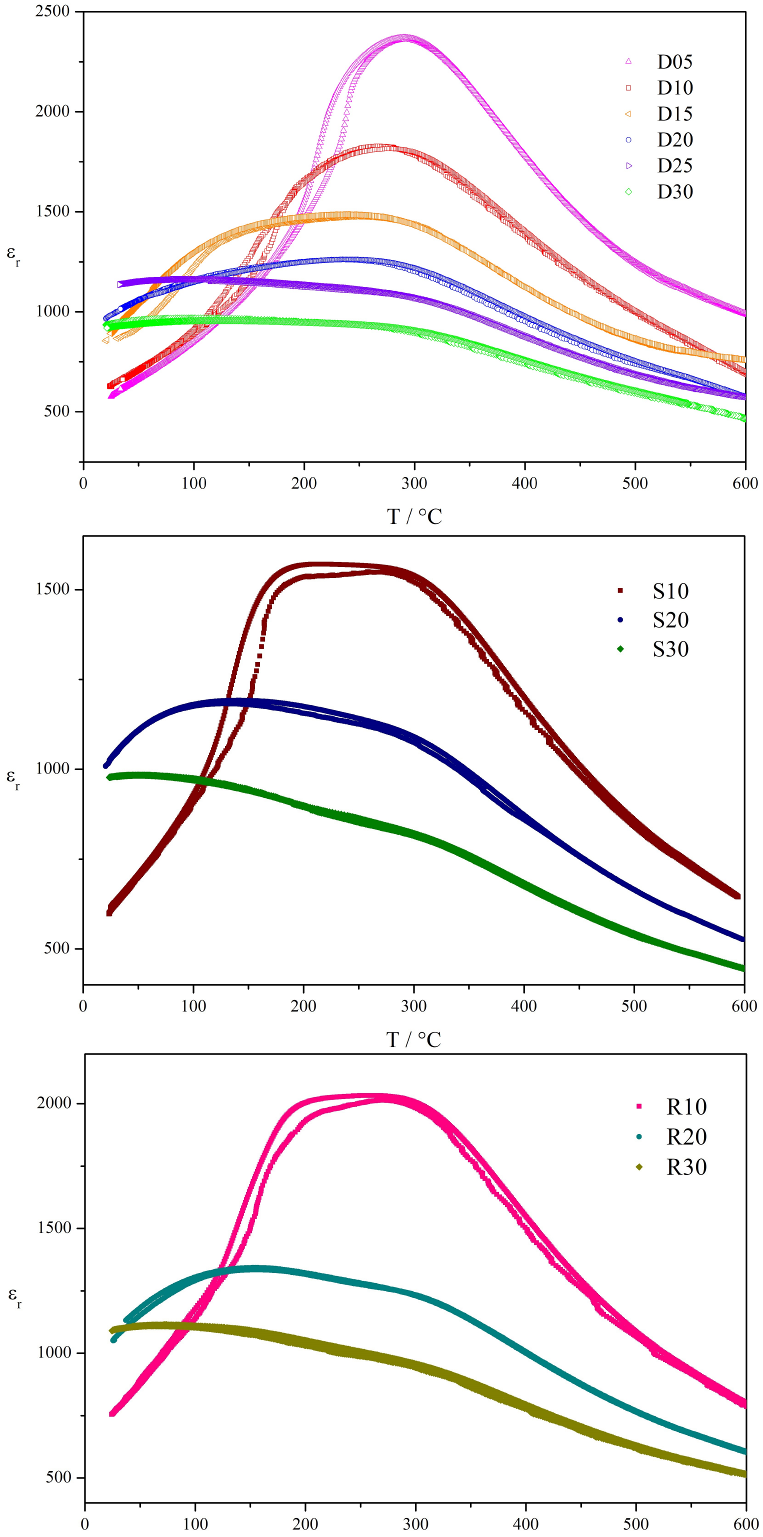

Figure 5.12: Temperature dependence of the permittivity on heating and cooling at 1 MHz for D (top), S (middle) and R (bottom) solid solutions.

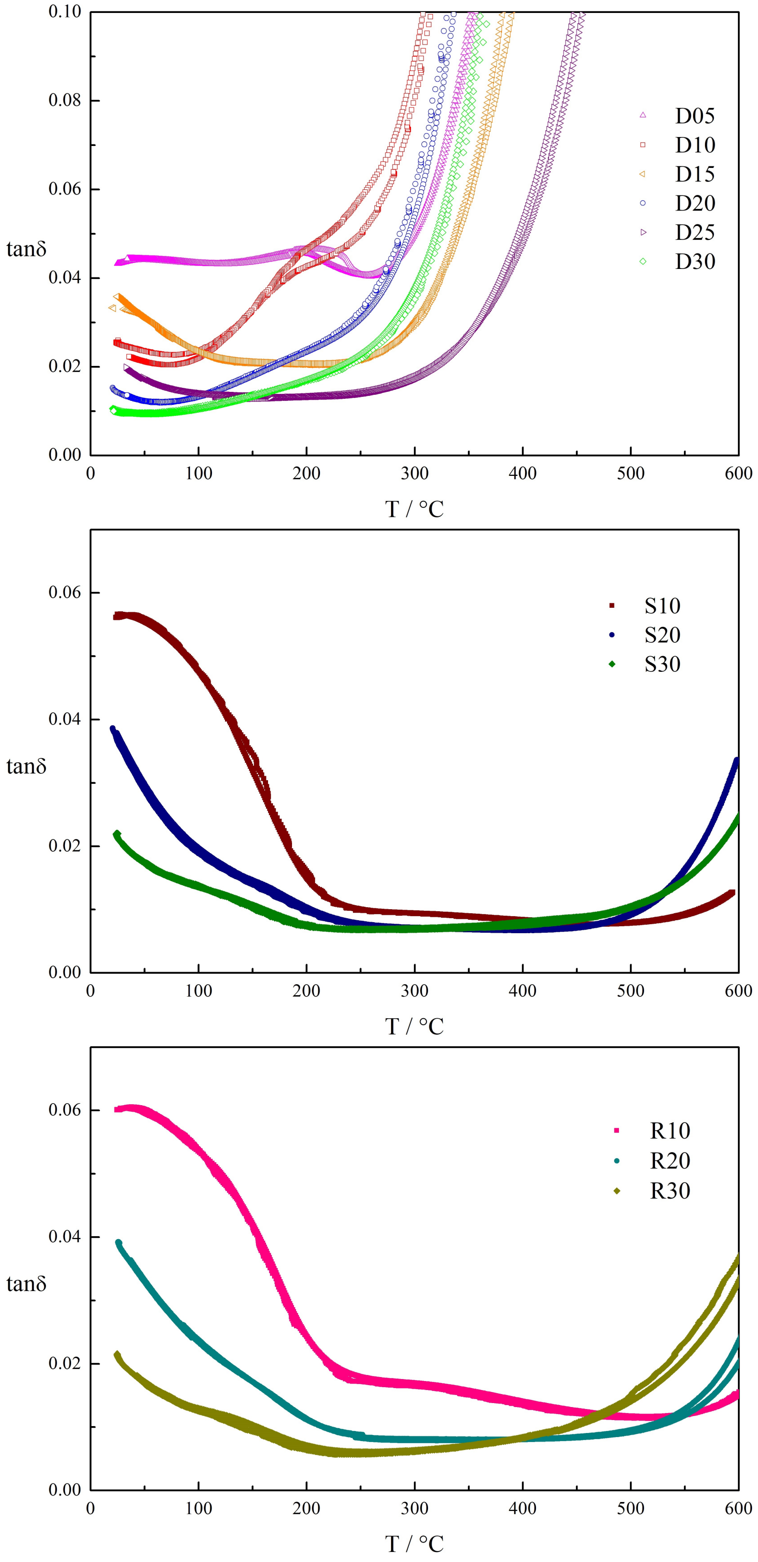

Figure 5.13: Temperature dependence of the dielectric loss on heating and cooling at 1 MHz for D (top), S (middle) and R (bottom) solid solutions.

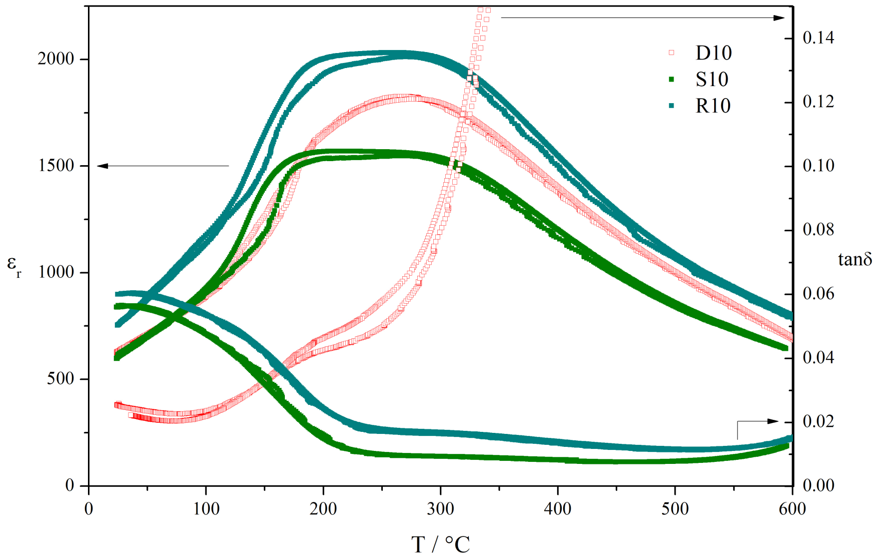

Figure 5.14: Temperature dependence of the permittivity and dielectric loss on heating and cooling at 1 MHz for D10, S10 and R10.

Figures 5.12 and 5.13 present the results of the dielectric measurements of the NBT-NN solid solutions. As reported in the literature the permittivity maxima shift to lower temperatures and a remarkable flattening of the permittivity-temperature profiles is observed with increasing NN content, however there are some differences between the shape and magnitude of the profiles between the three series. This difference is largest for the 10 % samples as highlighted with Figure 5.14. The dielectric loss for the NBT-NN and NB51T-NN series is low over a wide temperature range. For the NB49T-NN series it increases dramatically above 200 to 300 °C suggesting these bismuth-deficient samples are highly conductive.

For S30 the frequency dependence of the dielectric properties, including low temperature data, is shown in Figures 5.15 and 5.16. In the case of the dielectric loss a clear shift of the peak to higher temperatures occurs with increasing frequency. The peak in permittivity which appears near room temperature shifts in the same manner, although it is much more subtle. This frequency dependence indicates relaxor behaviour in the material.

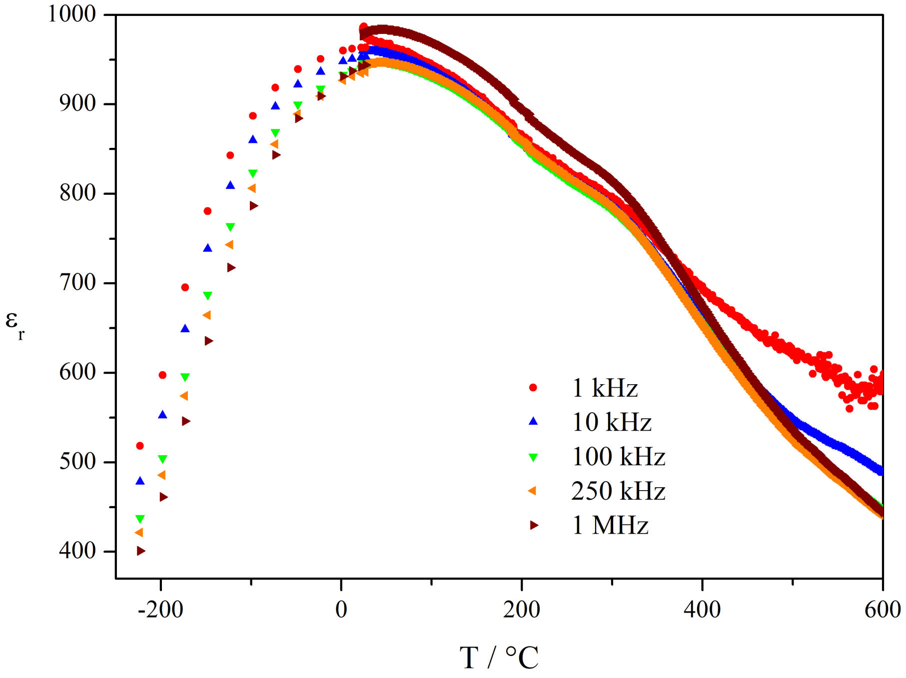

Figure 5.15: Relative permittivity on heating for S30 at low and high temperatures and various frequencies.

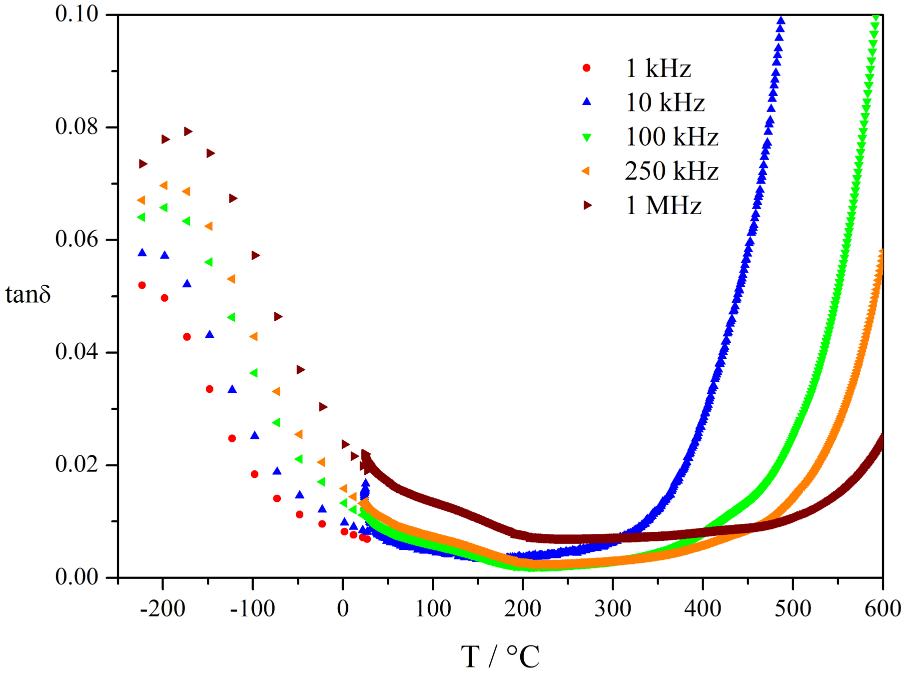

Figure 5.16: Dielectric loss on heating for S30 at low and high temperatures and various frequencies. High temperature data at 1 kHz are excluded for clarity.

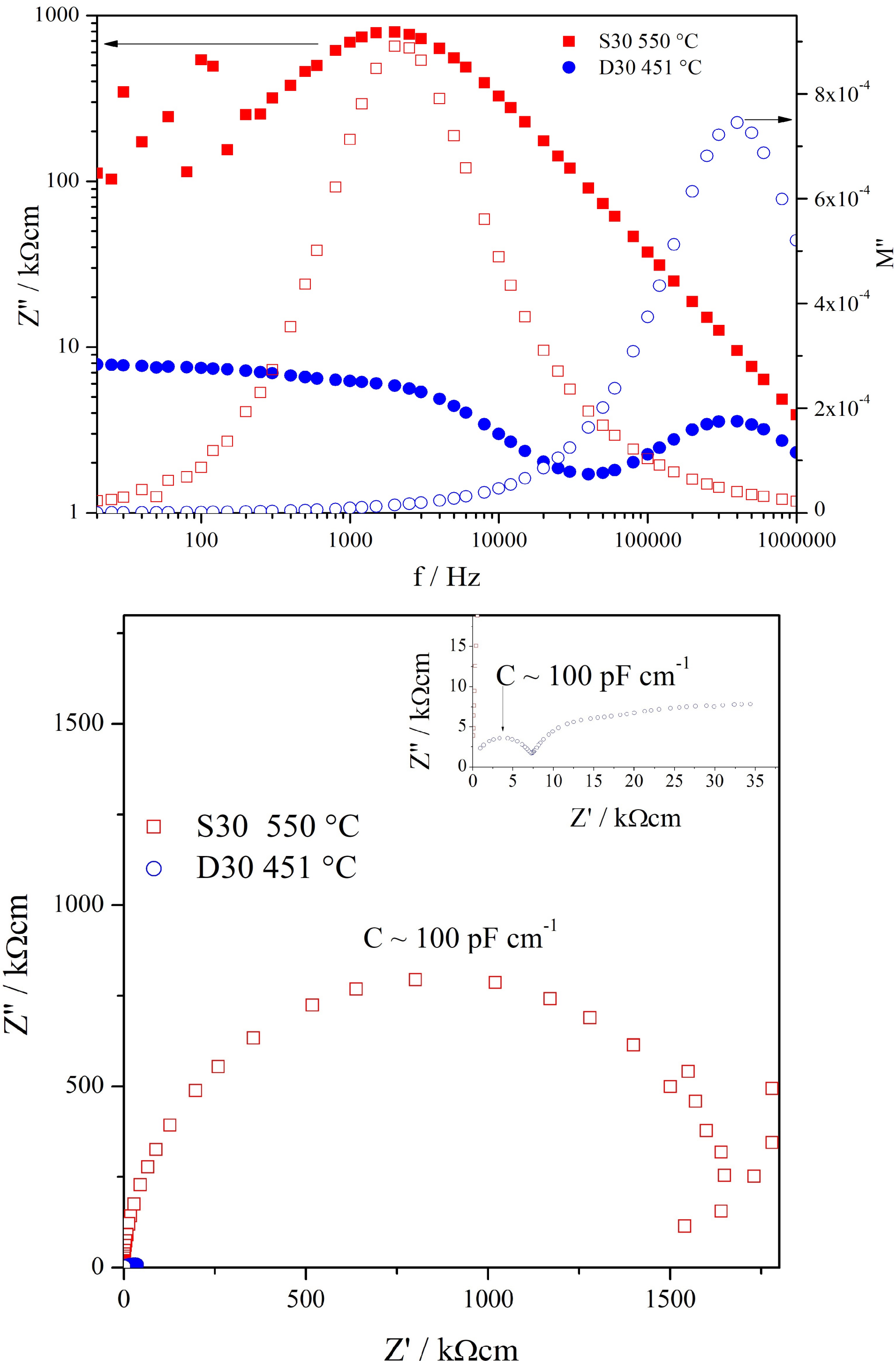

Figure 5.17: Top: Spectroscopic plots of the imaginary components of impedance (filled symbols, logarithmic scale) and electric modulus (open symbols, linear scale) from S30 at 550 °C (red squares) and D30 at 451 °C (blue circles). Bottom: Complex impedance plots for S30 at 550 °C (red squares) and D30 at 451 °C (blue circles).

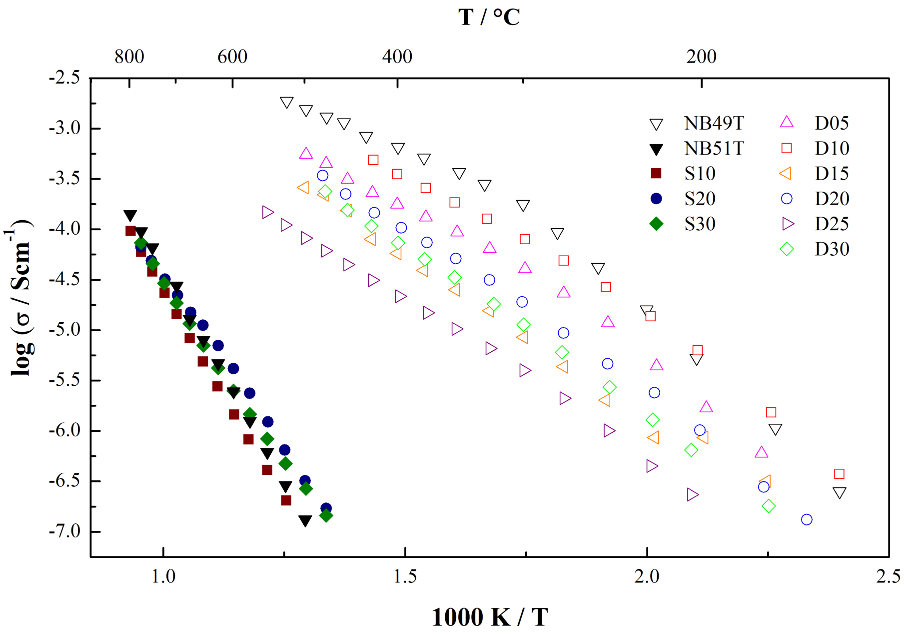

Figure 5.18: Arrhenius plot of bulk conductivities for NB49T-NN (open symbols) and NBT-NN compositions (filled symbols).

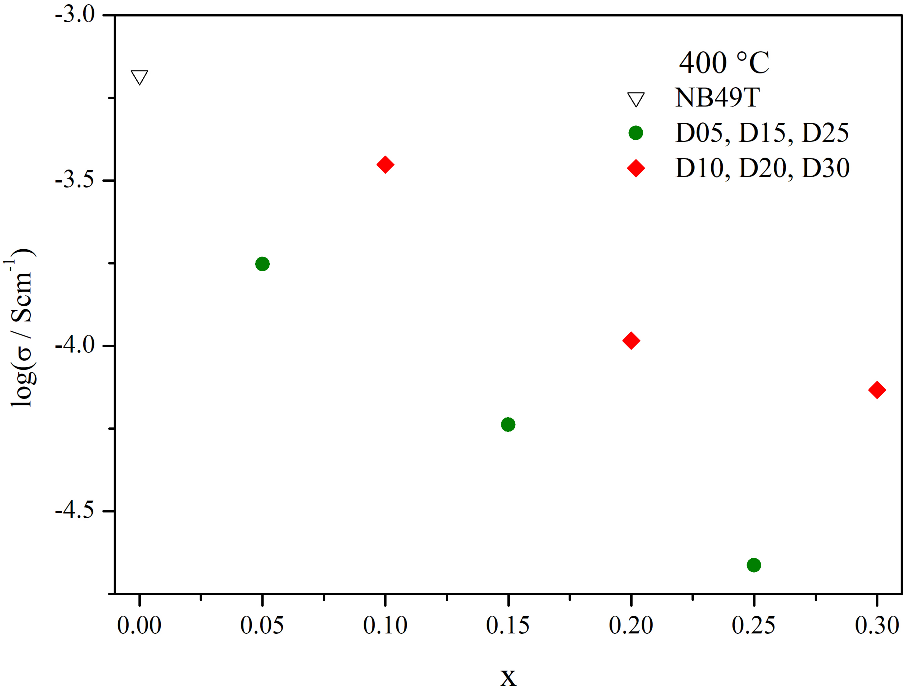

Figure 5.19: Bulk conductivities for NB49T-NN at 400 °C.

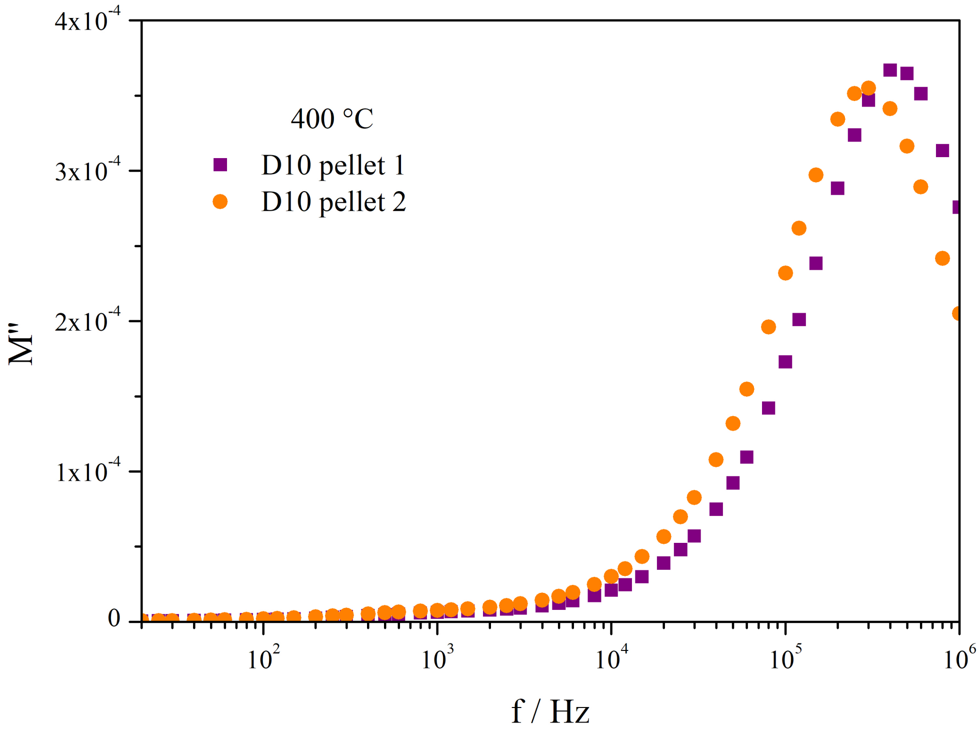

Figure 5.20: M” spectroscopic plots at 400 °C from two pellets of D10 sintered under the same nominal conditions from the same calcined powder.

Examples of impedance spectra for the 30% NN sample in the NB49T (D) and NBT (S) series are presented in Figure 5.17. For the nominally stoichiometric case only one response is observed in Z”, M” spectra and Z* plots and it is attributed to the bulk since it has a capacitance of the order of 100 pF. For the D30 sample, the bulk generates a high frequency response followed by two or three other poorly resolved responses at lower frequencies. Figure 5.18 is an Arrhenius plot of the bulk conductivities extracted from M” peaks for NB49T-NN (open symbols) and NBT-NN (filled symbols) solid solutions. The bismuth-deficient series is conductive, it becomes important to note that it was synthesised and prepared in two batches: one with 10, 20 and 30 %, the other with 5, 15 and 25% NN. It can be appreciated in Figure 5.19 that the D series retains a highly conductive behaviour similar to NB49T and within each batch the conductivity decreases with increasing NN content. However, the trend does not match between both batches as D10 has the highest conductivity (instead of D05) and D25 the lowest (rather than D30). Another set of pellets of the D05 and D10 compositions was sintered under the same nominal conditions, M” spectra for both pellets of D10 are compared in Figure 5.20 and the extracted bulk conductivities for D05 and D10 are shown in Figure 5.21. Although the nominal conditions were the same (even using the same furnace) the second set of pellets has different conductivities compared against the original set. Additionally, Figure 5.22 presents the dielectric measurements for these pellets, where a change in the magnitude of the total capacitance is observed for D05 however the shapes of the curves do not appreciably change much between different pellets of the same composition. This indicates the bulk conductivity in these solid solutions is very process sensitive.

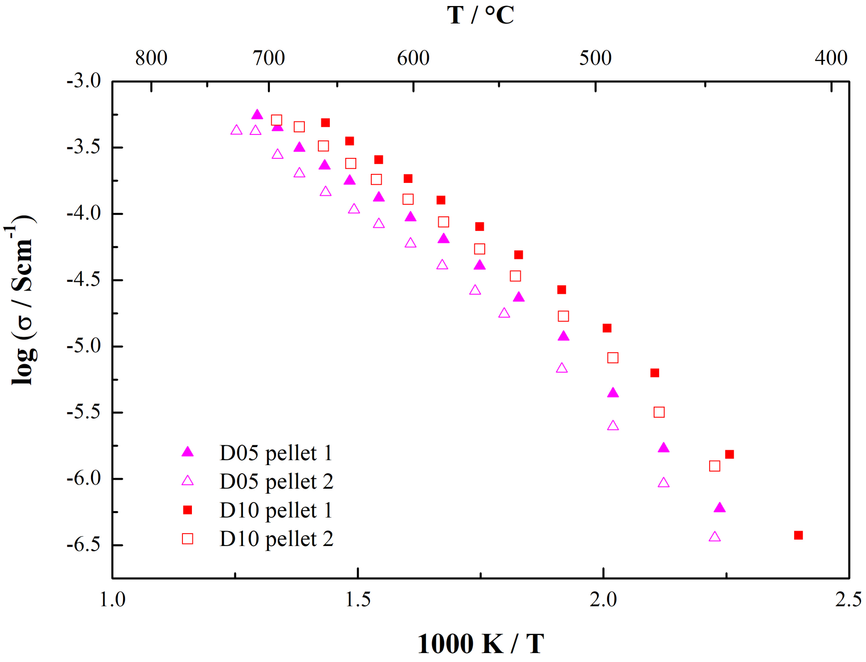

Figure 5.21: Arrhenius plot of bulk conductivities for two sets of D05 and D10 pellets processed under the same nominal conditions from the same calcined powders.

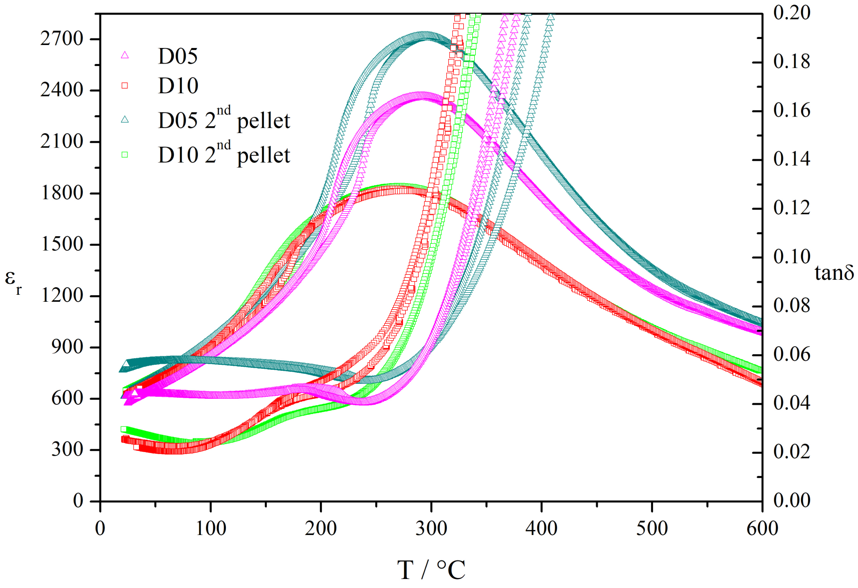

Figure 5.22: Temperature profiles of the dielectric constant and dielectric loss for two sets of D05 and D10 pellets processed under the same nominal conditions from the same calcined powders.

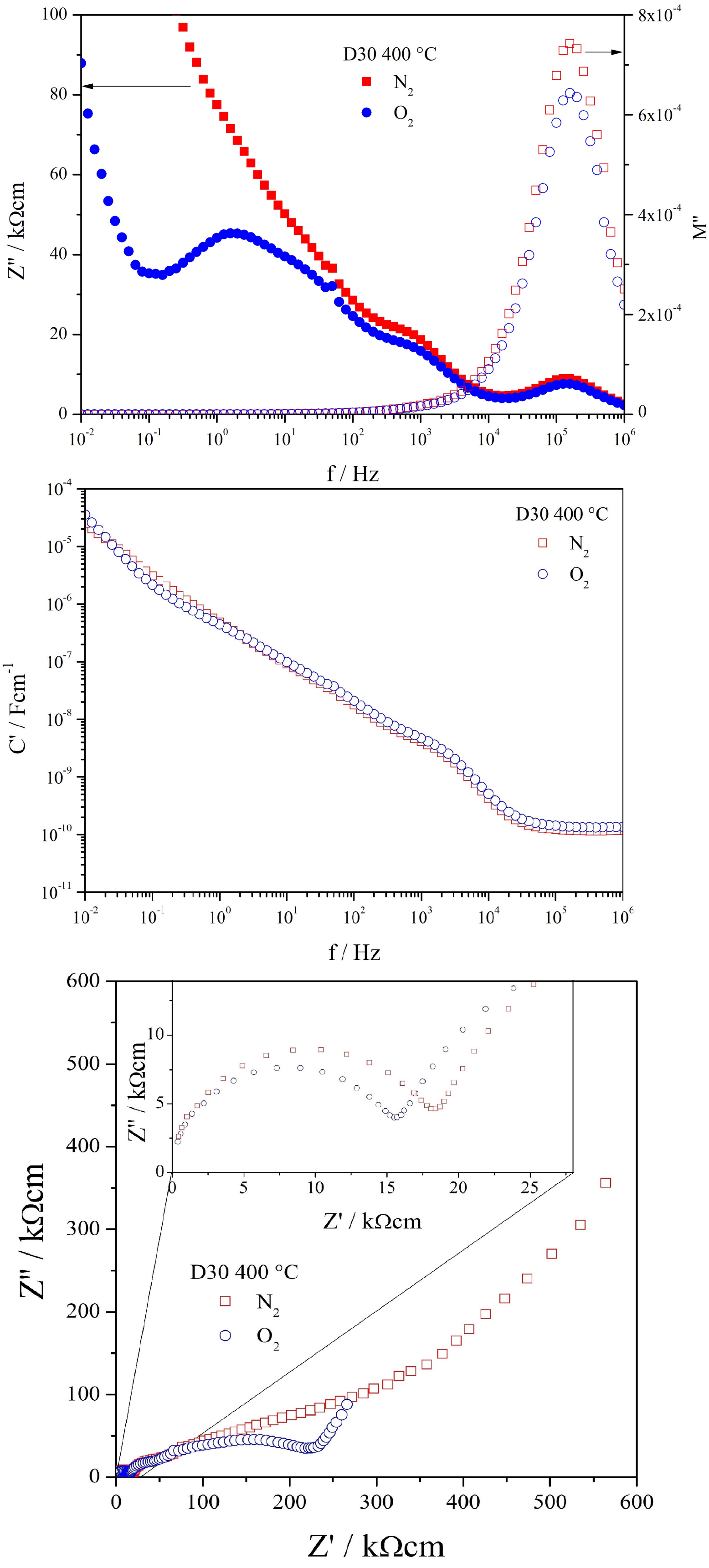

Figure 5.23: Top: Z” (filled symbols) and M” (open symbols) spectroscopic plots. Middle: C’ spectroscopic plots. Bottom: Complex impedance plots. All plots for D30 at 400 °C under O_2 (blue circles) and N_2 (red squares).

The nominally stoichiometric series is insulating with little difference between various NN contents. The NB51T-NN series (not shown) has slightly higher conductivities than the nominally stoichiometric series and also shows little change with the NN concentration. The dramatic shift in behaviour with bismuth content observed between the D and S series is similar to what is observed in un-doped NBT (nominally stoichiometric NBT is conductive, NB51T is insulating). Figure 5.23 shows impedance spectra collected for D30 at 400°C under O_2 and N_2, the bulk becomes slightly more conductive under high p_{O_2}. A low frequency ”spike” (indicative of ionic conduction) can be observed under both atmospheres, although under N_2 it is less resolved with the other responses. In both cases, the low frequency approaches capacitances of the order of 100 microFarads per centimetre.

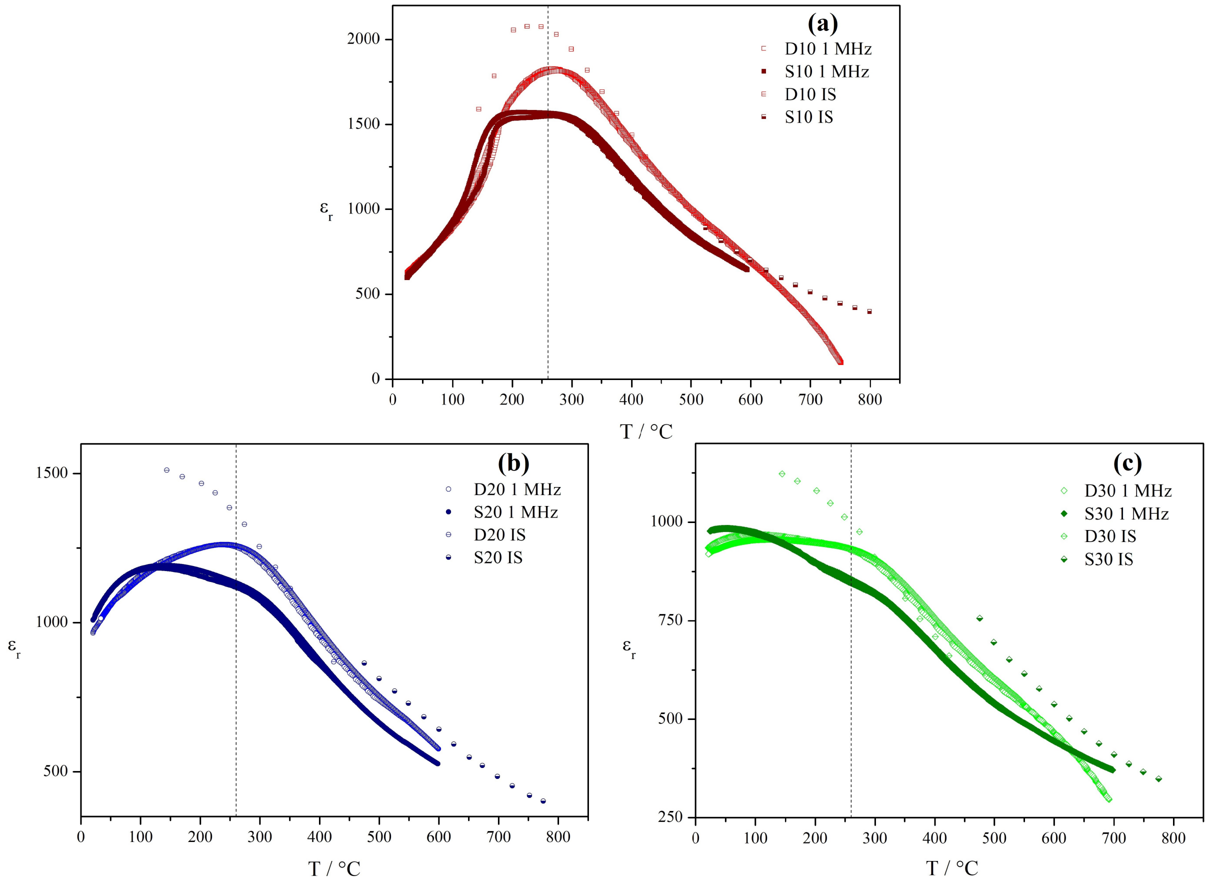

Figure 5.24: Temperature profiles of the relative permittivity for NB49T-NN and NBT-NN solid solutions. Open symbols in brighter/ligther colours correspond to 1 MHz dielectric mesurements of NB49T-NN samples, open symbols in brighter/lighter colours with a horizontal line accross are for data extracted from impedance spectroscopy of NB49T-NN samples; the 1 MHz data of NBT-NN samples are shown with filled symbols in dark colours, and the data from impedance spectroscopy of this series is presented with half-filled symbols in dark colours.

Figure 5.24 compares the permittivity-temperature profiles of NB49T-NN and NBT-NN compositions obtained from dielectric measurements at 1 MHz and extracted from M” peaks from impedance spectroscopy. For each NN content, there is a clear mismatch between the data from fixed-frequency measurements and the data extracted from IS around the permittivity maxima. Figure 5.25 compares the dielectric measurements for S30 against permittivity values extracted from ε' spectroscopic plots at select frequencies and from M” peaks.

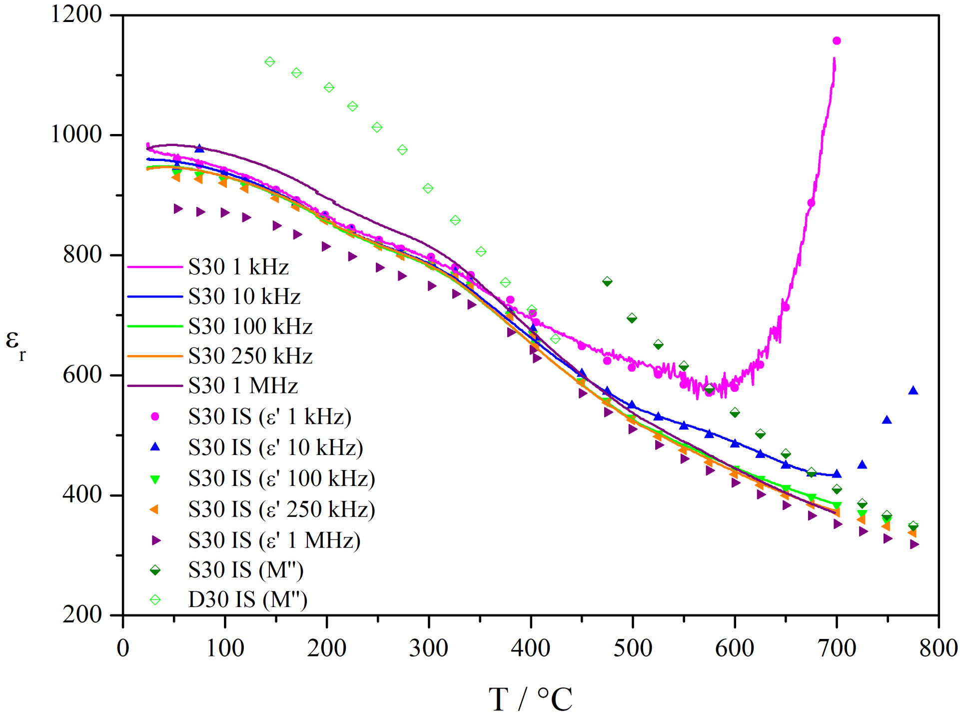

Figure 5.25: Temperature profiles of the relative permittivity for S30. Presenting data from dielectric measurements (solid lines), data extracted from ε' spectroscopic plots at select frequencies (filled symbols) and data extracted from M” peaks (half-filled symbols). Data from M” peaks for D30 (open symbols with horizontal line) is also shown.

Oxide ion transport numbers for the NB49T-NN series are presented in Figure 5.26. The ionic transport number seems to increase with temperature and there is no clear trend with the NN content.

In Figure 5.27 Z” and M” spectroscopic plots at ∼500 °C under nitrogen or oxygen are presented for a pellet of D30 as sintered and after being polished down to retain only ∼0.3 mm from the centre (the ”as sintered” pellet being ∼2 mm thick). For the polished pellet the measurements under oxygen were done in two separate experiments, one from 499 to 799 °C and another ranging between 204 and 502 °C. It can be appreciated that the high frequency response attributed to the bulk does not vary significantly, while the response in the Z” spectra

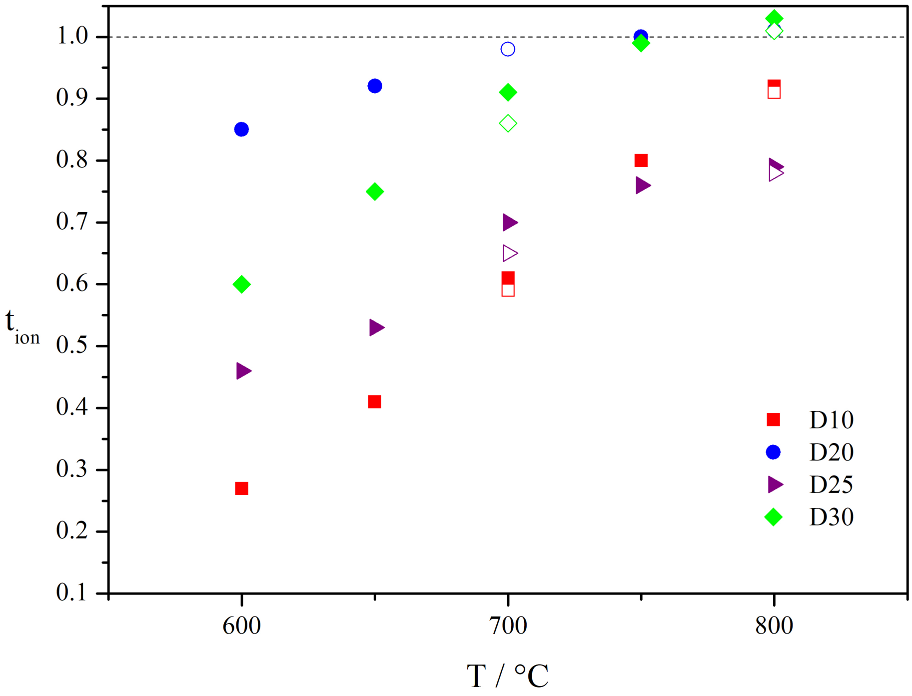

Figure 5.26: Oxide ion transport numbers from NB49T-NN solid solutions. Filled symbols correspond to a first measurement on cooling and open symbols correspond to measurements repeated on heating.

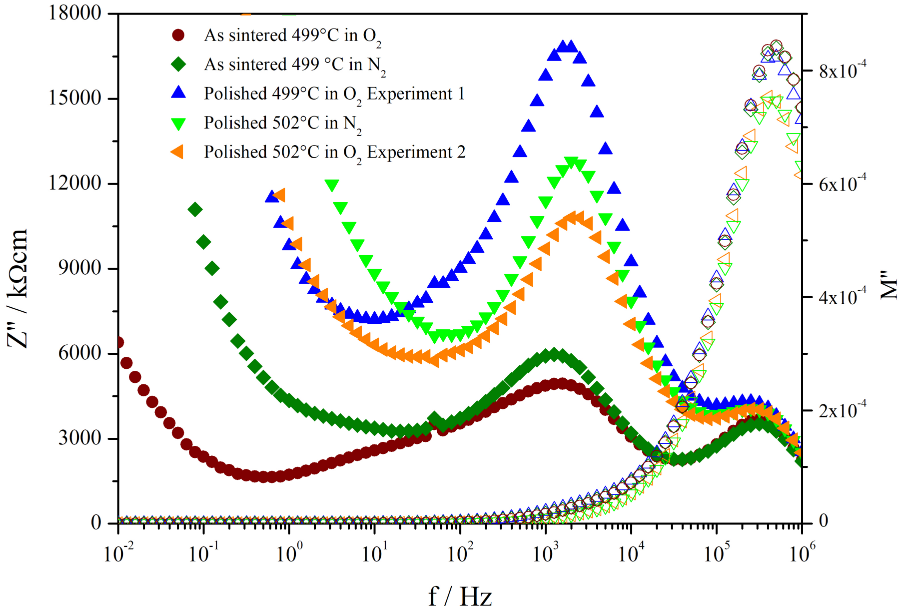

Figure 5.27: Z” (filled symbols) and M” (open symbols) spectroscopic plots at ∼500 °C under oxygen or nitrogen from a D30 pellet as sintered and after polishing.

around 1 kHz changes dramatically after polishing, it becomes less broad and noticeably more resistive. Focusing on the three measurements performed on heating on the polished pellet, a significant spread of the Z" peak heights is observed. The conductivity of the lower frequency response E2, discussed earlier for Figure 5.27, was extracted from the Z" peaks (by taking twice the peak height as the resistivity) and plotted in Figure 5.28. Also in FIgure 5.28, the corresponding capacitance obtained from the resistivity and time constant is compared against the bulk permittivity and the total permittivity.

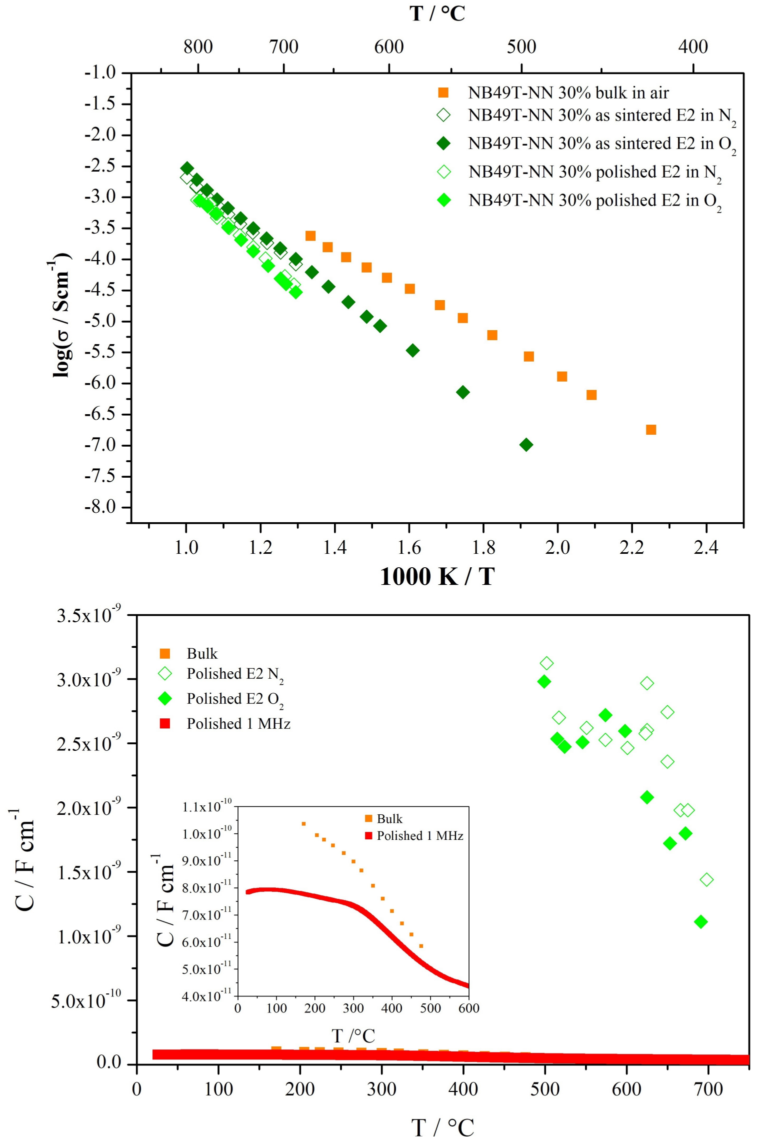

Figure 5.28: Top: Arrhenius plot for the bulk conductivity of D30 extracted from M" peaks and for the conductivity of the second (E2) element in the Z" spectroscopic plots. Bottom: Capacitance of the bulk (extracted from M" peaks) and the second element (from Z" spectroscopic plots) of D30, as well as the capacitance measured at 1 MHz.

5.3 Discussion

Laboratory XRD results in Figure 5.1 agree with the observations of Xu *et al.*, that the fraction of the low symmetry phase (Xu *et al.* consider $R3c$) diminishes with increasing NN content. Xu *et al.* track this by observing the (102) peak of the rhombohedral ($R3c$) phase around 23 degrees and the splitting of the (204) rhombohedral ($R3c$) peak just below 47 degrees into the (002) and (220) peaks of the tetragonal ($P4bm$) phase. As shown in Figure 5.3, the cell volume increases with NN content as expected from the larger radius of Nb^{5+} (64 pm) compared against Ti^{4+} (60.5 pm) and no significant difference is apparent between the D, S and R series. The change in cell volume and agreement between the starting compositions and quantitative EDX analysis in Figure 5.10 confirm the formation of the solid solution. The backscattered electron images show clearly the presence of impurities, while they are too small for adequate identification through EDX, the area containing the largest particle found was very rich in Ti, suggesting these impurities might be TiO_2. The impurities might be unreacted TiO_2 and Nb_2O_5 or products of decomposition of the main phase from losses of Na and Bi through volatilisation.

The room temperature neutron diffraction data in Figure 5.7 show that a higher symmetry phase is present in the R10 sample and the Cc polymorph is present in the D30 sample. The latter was not detected by XRD. This leads to conclude that, as the polymorphism of these materials is mainly related to different tilting schemes of the TiO_6 octahedra, the improved sensitivity of the neutrons to oxygen makes neutron diffraction more suitable than X-rays to detect the different phases. For D30, diffraction data at 4.2 K are compared against room temperature data in Figure 5.6, where it can be appreciated that there is no significant change in the amounts of both polymorphs. Two options for analysing the variable temperature neutron diffraction data in Figure 5.7 are considered. One based on coexistence of Cc and $P4bm$ structures in line with the polymorphism described in Reference [4]. The second option is to analyse this data considering the Cc and $Pnma$ polymorphs to coexist and then the orthorhombic ($Pnma$) cell transforming to the tetragonal ($P4bm$) one as considered in References [17, 18].

The first analysis tracks the evolution of the phase assemblages by relying on a few peaks that arise from only one polymorph such as the peaks around 2.35 and 1.78 Å for the low temperature polymorph (Cc) and those around 2.46, 2.08 Å for the tetragonal ($P4bm$) phase. At room temperature, for the R10 sample subtle signs of the tetragonal ($P4bm$) phase can be detected. These are much clearer for the other two compositions where both polymorphs clearly coexist, with the amount of tetragonal ($P4bm$) phase increasing with NN content. As the temperature increases, the amount of low symmetry (Cc) phase decreases and is no longer detected at 400 °C, in all three cases. It is interesting to note that from 250 °C the relative intensities of the peaks in the patterns of the three samples look fairly similar. At 600 °C the tetragonal

($P4bm$) phase can barely be detected indicating that the perovskite has nearly become cubic. Although Figures 5.4 and 5.5 indicate the presence of the $Pnma$ polymorph, in the second option for analysis it is not as clear at which temperatures the Cc polymorph dissapears and the $Pnma$ to $P4bm$ transitions occur since the peaks from $Pnma$ NBT overlap with the peaks that allow to distinguish the $P4bm$ and Cc polymorphs as illustrated in Figure 5.8. In any case, the introduction of NN is stabilising the tetragonal ($P4bm$) or orthorhombic ($Pnma$) polymorph to lower temperatures while maintaining the higher temperature transition (from fully tetragonal ($P4bm$) to cubic) similar across the three studied compositions.

The electrical behaviour of this system is complex and several effects can be appreciated in the results that have been presented. First the effect of NN on the permittivity-temperature profile of NBT is discussed. Next, the possible causes for the decrease in conductivity with the introduction of NN are discussed, followed by the evolution of the bulk conductivity activation energies along the D series. Then, the difference between the permittivity data obtained from dielectric measurements and the values extracted from M” spectroscopic plots for the bulk is analysed. Finally, the presence and behaviour of another electroactive region (as well as its influence on the ionic transport number measurements) are discussed.

It can be appreciated from the permittivity-temperature profiles in Figures 5.12 and 5.24 that, with the exception of D05 (which has a maximum slightly below 300 °C), all compositions seem to have a local permittivity maximum around 260 °C (which is more pronounced in the conductive samples) while another peak (more noticeable in the insulating samples) keeps shifting to lower temperature with increasing NN content. If the deconvolution of the permittivity-temperature profile (described in Chapter 2) suggested by Jo *et al.* [30] is assumed to be applicable to the NBT-NN system, it seems that NN causes the peak related to the Cc-$P4bm$ phase transition to decrease down to 260 °C and then stops, since from 10 % NN and above all samples display a permittivity feature around that temperature and the ND patterns in Figure 5.7 become similar for all three NN concentrations from 250 °C onwards. The anomaly related to the relaxor contribution keeps shifting to lower temperatures with increasing NN content, which contributes significantly to the broadening of the total permittivity response.

The fact that the S series is insulating is consistent with the trapping of oxygen vacancies by acceptors. The sodium from NN can act as an acceptor on the A site ($\mathrm{Na}_{\mathrm{Bi}}^{\prime\prime}$) and trap oxygen vacancies ($(\mathrm{Na}_{\mathrm{Bi}}^{\prime\prime}{-}\mathrm{V}_{\mathrm{O}}^{\bullet\bullet})^{\times}$), although not as strongly as B-site dopants do and therefore the small bismuth deficiency in the D series can reintroduce high levels of conductivity. Another contribution from NN to decreasing the conductivity could be that small losses of soda during processing leave an slightly donor-doped (Nb^{5+}) composition. A third possible contribution to the lowering of the conductivity with increasing NN content can be the reduced fraction of Bi-Bi-Ti saddle points forcing the oxide ions to migrate through Na-Bi-Ti triangles and reducing their mobility, causing the increase of the bulk conductivity activation energy with NN content. The presence of low frequency spikes (which can originate from mobile ions being blocked at the electrodes or a Warburg response, as discussed in Chapter 4) and weak p_{O_2} dependence observed in Figure 5.23 indicates that the conduction in D30 is predominantly ionic. There is also a p-type electronic contribution (in contrast with the n-type behaviour observed in Chapter 4) which could be attributed to oxygen absorption by the sample leading to partial oxidation of Bi^{3+} to Bi^{5+}.

The fact that the change in activation energy for the D10 sample in Figure 5.18 occurs at lower temperature than in NB49T and that in the other samples there is no appreciable change in slope agrees with the suggestion that this change is related to the ratios between polymorphs as the ND data shows the stabilisation of the high temperature polymorph to lower temperatures with increasing NN content. This also agrees with the shifting of the permittivity maxima to lower temperatures with increasing NN content observed in Figure 5.15.

The different shapes and mismatch of the magnitudes of the permittivity-temperature profiles from dielectric measurements and impedance spectroscopy compared in Figure 5.24 indicates there is more than one contribution to the total capacitance of these samples, since Figure 5.25 shows it is not an effect of measuring frequency and both instruments provide similar values at fixed frequencies, indicating the mismatch is not instrument related. This difference is most clear when focusing on the 10% NN samples (Figure 5.14) for which the differences seem more dramatic for the insulating NBT-NN case, while for the NB49T-NN sample the shape of the curve is similar, the insulating sample presents a large flattened region through the permittivity peak. One possibility is that the total capacitance responses are a mix of the bulk with some other electroactive region in the sample (it is reasonable to assume that there is a lower capacitance element connected in series, as the lowest capacitance would dominate the total capacitance in the circuit). The contribution of this other element is presumably less significant for the conductive NB49T based samples where the bulk has a lower resistivity. Another potential explanation is to consider that, as the ND data indicate there is phase coexistence for these samples between room temperature and 400 °C, the M” peaks might be a response from only one polymorph. This scenario would require significantly different electrical properties from both polymorphs to account for the fact that this sort of behaviour is not observed for undoped NBT.

In Figure 5.27 the dramatic change upon polishing (particularly regarding the broadness of the peak) and the sensitivity to the sample history (the difference between the two measurements done under oxygen) suggest this intermediate frequency response (E2) might be from surface layers on the pellet.

The temperature dependence of the oxide ion transport number observed in Figure 5.26 is unusual both in the range of transport numbers it spans and the gradients, since the electronic contribution is expected to become larger with increasing temperature due to its larger activation energy compared against the oxide ion conduction in NBT. From Figure 5.28 it is clear that in the temperature range used for the measurement of ionic transport numbers (600 to 800 °C) other electroactive regions such as E2 can influence or even dominate the total electrical response of the sample therefore, the ionic transport numbers measured do not correspond to the bulk.

5.4 Conclusions

Based on the EDX analysis in Figure 5.10 and the cell expansion seen in Figure 5.3 the solid solutions of NBT with NN can form to higher concentrations than those explored with high pressure bismuth-based perovskites discussed in Chapter 4. The introduction of NN into NBT stabilises the higher symmetry phases to lower temperatures. This is likely the cause for the shift in the temperature of the permittivity maximum and change in bulk conductivity activation energy which is appreciable for the D10 sample.

The introduction of more sodium ions on the A-site, which would diminish the amount of ”easy” Bi-Bi-Ti saddle points, might also lead to trapping of the oxygen vacancies as discussed in Chapter 4 or slightly donor-doped compositions due to sodium volatilisation causing low conductivities comparable to NB51T as shown in Figure 5.18. However, a small bismuth deficiency (see compositions in Table 5.1) can reintroduce conductivities comparable to NB49T suggesting the trapping by sodium ions is not very effective. Based on the weak dependence of the bulk conductivity with p_{O_2} evidenced in Figure 5.23, the high conductivity is mostly ionic. Since the measurements of oxide ion transport number for this system are not representative of the bulk, it is not possible with the available evidence to confirm oxide ion conduction.

Figure 5.27 suggests that another electroactive region with a strong dependence on sample history (therefore difficult to control) can have an impact on the measured electrical properties, as evidenced in Figure 5.28, which can explain the behaviour observed in the ionic transport number measurements in Figure 5.26.

The discrepancy of the permittivity-temperature profiles from dielectric measurements and those extracted from impedance spectroscopy in Figure 5.24 has not been reported before and clearly means that the 1 MHz permittivity response is not from a single element. This is strongly related to the attractive temperature stability of the permittivity. Since this other element is not identified nor understood (it could correspond to a microstructural feature or be due to the complex polymorphism of the system) it can introduce an issue with the reproducibility of the permittivity-temperature profiles as evidenced by the difference in their magnitudes (even for the same composition) seen in Figures 5.14 and 5.22, which could be due to changing ratios of the contribution of each element to the total permittivity.

Chapter 6

Pyrochlore solid solution

6.1 Introduction

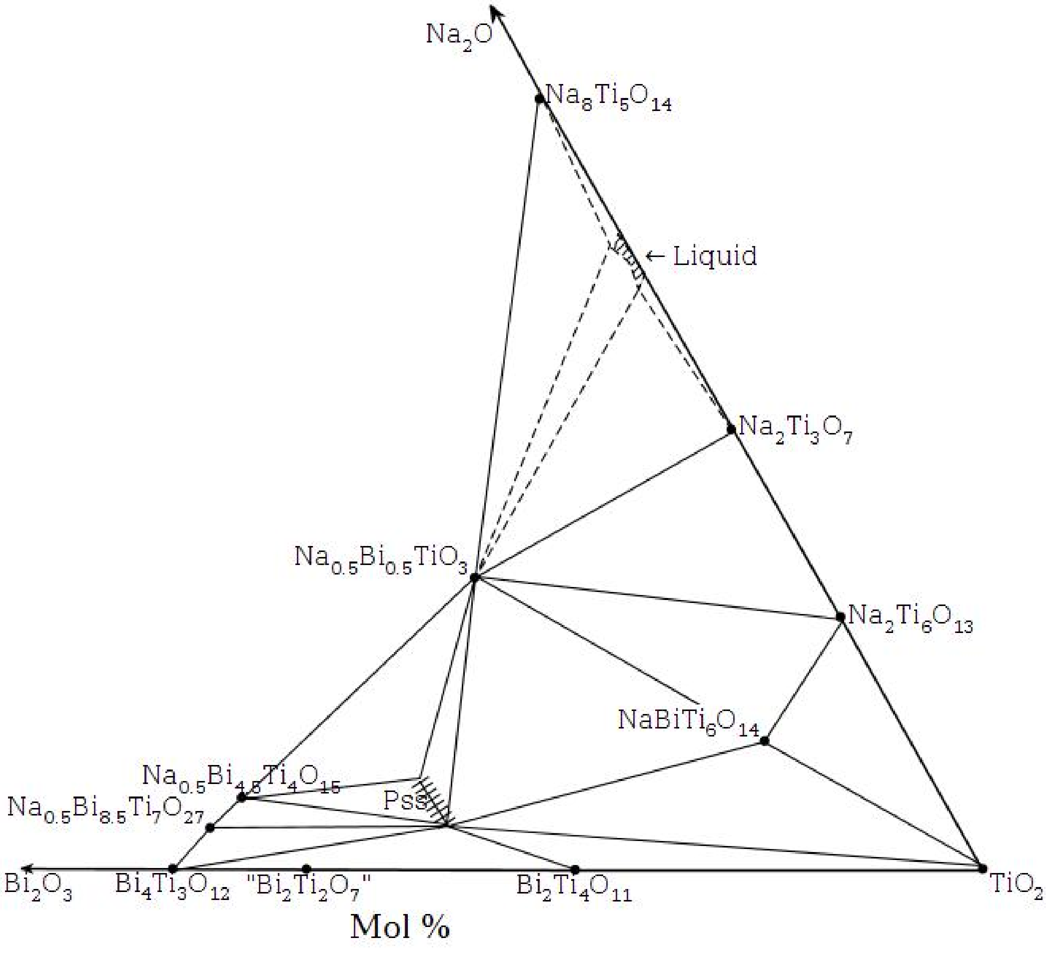

Figure 6.1: Partial $Na_2O{\cdot}Bi_2O_3{\cdot}TiO_2$ phase diagram. Adapted from Uchida and Kikuchi, *Subsolidus Phase Equilibria in the System* Na_2O*-*Bi_2O_3*-*TiO_2 *at 1000* °C, J. Am. Ceram. Soc., **61**, 58 (1978) with permission from John Wiley and Sons..

The $Na_2O \cdot Bi_2O_3 \cdot TiO_2$ ternary system contains several materials with electrical functionalities, for example the ferroelectric Aurivillius phases: $Bi_4Ti_3O_{12}$, $Na_{0.5}Bi_{8.5}Ti_7O_{27}$ and $Na_{0.5}Bi_{4.5}Ti_4O_{15}$ [98, 99]; $Na_{0.5}Bi_{0.5}TiO_3$ (NBT) is a ferroelectric perovskite that can exhibit high levels of oxide ion conduction [6] when prepared with deliberate Bi_2O_3 deficiency (i.e. $Na_{0.5}Bi_{0.49}TiO_{2.985}$) or a good dielectric or piezoelectric material if prepared nominally bismuth-rich to compensate for Bi_2O_3 losses during processing (i.e. $Na_{0.5}Bi_{0.51}TiO_{3+\delta}$); $Bi_2Ti_4O_{11}$ which is an antiferroelectric phase that has been investigated as a microwave dielectric material [100]. In 1978 Uchida and Kikuchi reported the phase equilibria at 1000 °C for the TiO_2-rich end of the phase diagram, here reproduced as Figure 6.1. Their work included the first (and only, to the best of my knowledge) observation of a pyrochlore solid solution (Pss) with the composition $x\%Na_2O \bullet 25\%Bi_2O_3 \bullet (75 - x\%)TiO_2$ (in mol%) for x ranging between 2.5 and 3.75% [24]. It is of interest to investigate the electrical properties of this unexplored pyrochlore solid solution and compare its conduction properties against the NBT perovskite.

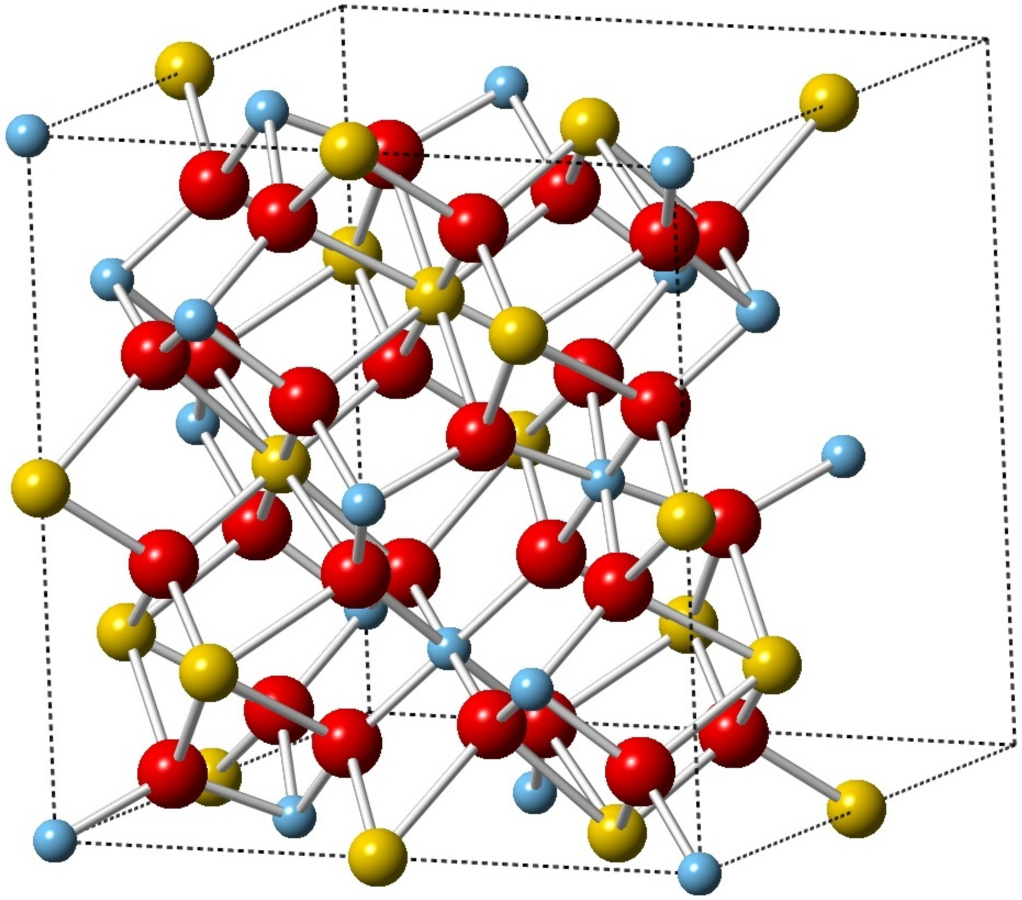

Figure 6.2: Half unit cell of an ideal $A_2B_2X_7$ pyrochlore. A ions in yellow, B ions in blue, X ions in red.

The pyrochlore structure $A_2B_2X_6X'$, represented in Figure 6.2, can be thought of as a defective fluorite (space group $Fd\bar{3}m$) with ordered cations and ordered anion vacancies. The large A ions occupy distorted cubic sites, the B site has octahedral coordination and the anions sit in $7/8$ths of the tetrahedral sites and the X site corresponds to the 48f Wycoff site and the X' site to the 8b site [101]. It is also often described as a rigid BX_6 octahedral network interpenetrated with a more flexible network of A_2X' chains. Pyrochlore oxides are know to exhibit diverse functionalities, including oxide ion conduction as electrolytes or mixed conductors [84, 102] enabled by the intrinsic anion vacancies and easy migration through unoccupied octahedral sites.

All known bismuth pyrochlores exhibit relaxor behaviour and have therefore been intensely studied for their attractive dielectric properties as well as low sintering temperatures compared to other common microwave dielectrics [103]; however, the dielectric loss tends to peak around room temperature in the GHz range which hinders their application in devices. Since the origin of the dielectric relaxation in these materials is not completely understood it is also difficult to tune or predict their properties. The relaxor behaviour expresses some common features in their properties such as broad ε' maxima, relatively low dielectric losses and a shift to higher temperatures of the ε'' maxima with increasing frequency accompanied by a decrease of ε' with frequency in the same temperature range.

$Bi_2Ti_2O_7$ is a pyrochlore that has been extensively studied due to the interesting optical and electrical properties found for several bismuth titanates and also as a photocatalyst for hydrogen production; however, it cannot be prepared through conventional solid state synthesis and sintering methods due to a narrow window of stability and the incongruent melting of the material [26, 104, 105]. Based on Rietveld refinements of neutron diffraction data, Radosavljevic *et al.* [106] and Kim *et al.* [107] conclude this compound forms as a cubic pyrochlore and is not actually stoichiometric but forms with a partially occupied A-site (~5 % vacant). In Reference [108] Piir *et al.* consider that $Bi_2Ti_2O_7$ forms with A-site vacancies because the r_{Bi}/r_{Ti} ratio (1.93) is too large and falls outside the stability field for pyrochlores (1.48 to 1.80 [84]). The A-site vacancies result in a smaller effective A-site radius and allow the pyrochlore phase to form. They also consider dopants can adjust this ratio and stabilise the pyrochlore.

A review by Esquivel-Elizondo *et al.* [105] details and discusses several issues with this material including a commonly observed bismuth-deficiency of around 10% and how to assess the phase purity of the powders, for which they contrast the colour and XRD pattern of the powder they synthesise through coprecipitation against those of some mixtures with $Bi_4Ti_3O_{12}$, which is one possible impurity. They also report a broad maximum in permittivity of 115 around

−50 °C between 500 to 2000 kHz in their microwave assisted sintered pellets. In a subsequent publication [109], Turner *et al.* study in more detail the dielectric properties of their $Bi_2Ti_2O_7$ pellets, which they compare against $Bi_{1.5}Zn_{1.0}Nb_{1.5}O_7$ (they use this compound to illustrate the characteristic response of most bismuth-pyrochlores) as seen in Figure 6.3. They find a significantly different response compared to other bismuth pyrochlores, which they attribute to the absence of substitutional ions on the A-site. The main differences are a lack of convergence of the ε' values at different frequencies at high temperatures, and the observation that peaks in ε'' occur at higher temperatures than other bismuth pyrochlores and that the relaxation frequencies are also much lower. The authors suggest the dielectric relaxation in $Bi_2Ti_2O_7$ is due to space charge polarisation based on the frequency range at which they observe it.

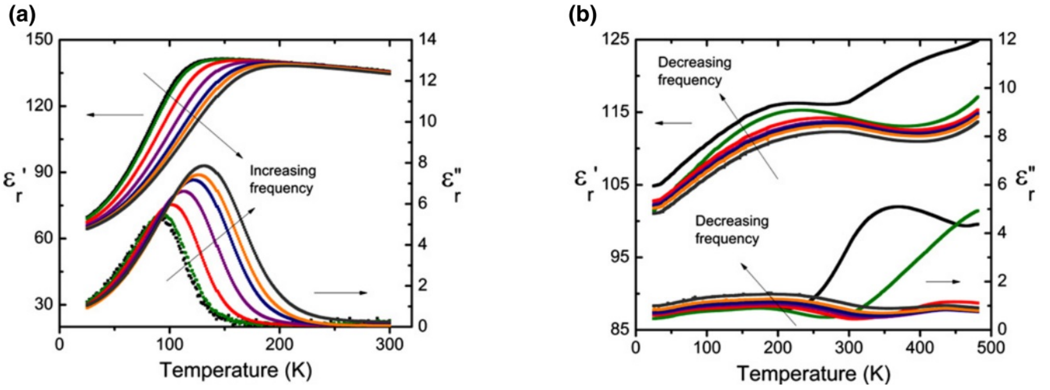

Figure 6.3: Temperature profiles of the real and imaginary components of the permittivity from 10 kHz to 2 MHz of a) $Bi_{1.5}Zn_{1.0}Nb_{1.5}O_7$ and b) $Bi_2Ti_2O_7$. Reproduced from Turner *et al.*, J. Am. Ceram. Soc., **97** [6], 17631768 (2014) with permission from John Wiley and Sons. © 2014 The American Ceramic Society.

6.2 Results and discussion

6.2.1 Processing and phase identification

Table 6.1: List of Pss samples prepared.

Sample	Composition	Nominal formula	Phases present by XRD
U1	2.5%N 25%B 72.5%T	$Na_{0.138}Bi_{1.379}Ti_2O_{6.138}$	Pss, NBT
U2	2.8%N 25%B 72.2%T	$Na_{0.155}Bi_{1.385}Ti_2O_{6.155}$	Pss, NBT
U3	3.2%N 25%B 71.8%T	$Na_{0.178}Bi_{1.393}Ti_2O_{6.179}$	Pss, NBT
U4	3.5%N 25%B 71.5%T	$Na_{0.196}Bi_{1.399}Ti_2O_{6.196}$	Pss, NBT
U5	3.75%N 25%B 71.25%T	$Na_{0.211}Bi_{1.404}Ti_2O_{6.211}$	Pss, NBT
A1	3.1%N 25.1%B 71.8%T	$Na_{0.173}Bi_{1.398}Ti_2O_{6.184}$	Pss, NBT
A2	3.0%N 25.2%B 71.8%T	$Na_{0.167}Bi_{1.404}Ti_2O_{6.189}$	Pss, NBT
A3	2.9%N 25.3%B 71.8%T	$Na_{0.162}Bi_{1.409}Ti_2O_{6.195}$	Pss, NBT
A4	2.7%N 25.5%B 71.8%T	$Na_{0.150}Bi_{1.421}Ti_2O_{6.206}$	Pss, NBT
A5	2.5%N 25.7%B 71.8%T	$Na_{0.139}Bi_{1.432}Ti_2O_{6.217}$	Pss, NBT
A6	2.3%N 25.9%B 71.8%T	$Na_{0.128}Bi_{1.443}Ti_2O_{6.228}$	Pss, NBT
A7	2.1%N 26.1%B 71.8%T	$Na_{0.117}Bi_{1.454}Ti_2O_{6.240}$	Pss, NBT?
A8	1.9%N 26.3%B 71.8%T	$Na_{0.106}Bi_{1.465}Ti_2O_{6.251}$	Pss
A9 (Pss09)	1.7%N 26.5%B 71.8%T	$Na_{0.095}Bi_{1.476}Ti_2O_{6.262}$	Pss
A10	1.5%N 26.7%B 71.8%T	$Na_{0.084}Bi_{1.487}Ti_2O_{6.273}$	Pss, $Bi_2Ti_4O_{11}$, $Bi_4Ti_3O_{12}$
A11	1.3%N 26.9%B 71.8%T	$Na_{0.072}Bi_{1.499}Ti_2O_{6.284}$	Pss, $Bi_2Ti_4O_{11}$, $Bi_4Ti_3O_{12}$
A12	0.9%N 27.3%B 71.8%T	$Na_{0.050}Bi_{1.521}Ti_2O_{6.306}$	Pss, $Bi_2Ti_4O_{11}$, $Bi_4Ti_3O_{12}$
B1	2.45%N 26.3%B 71.25%T	$Na_{0.138}Bi_{1.476}Ti_2O_{6.284}$	Pss, NBT
B2	2.25%N 26.5%B 71.25%T	$Na_{0.126}Bi_{1.488}Ti_2O_{6.295}$	Pss, NBT
B3	2.05%N 26.7%B 71.25%T	$Na_{0.115}Bi_{1.499}Ti_2O_{6.306}$	Pss
B4	1.85%N 26.9%B 71.25%T	$Na_{0.104}Bi_{1.510}Ti_2O_{6.317}$	Pss
B5	1.65%N 27.1%B 71.25%T	$Na_{0.093}Bi_{1.521}Ti_2O_{6.328}$	Pss
B6 (Pss08)	1.45%N 27.3%B 71.25%T	$Na_{0.081}Bi_{1.533}Ti_2O_{6.340}$	Pss
B7	1.25%N 27.5%B 71.25%T	$Na_{0.070}Bi_{1.544}Ti_2O_{6.351}$	Pss, $Bi_2Ti_4O_{11}$, $Bi_4Ti_3O_{12}$
B8	0.85%N 27.9%B 71.25%T	$Na_{0.048}Bi_{1.566}Ti_2O_{6.373}$	Pss, $Bi_2Ti_4O_{11}$, $Bi_4Ti_3O_{12}$
Pss07	1.24%N 27.9%B 70.82%T	$Na_{0.070}Bi_{1.578}Ti_2O_{6.402}$	Pss
Pss10	1.81%N 26.0%B 72.20%T	$Na_{0.100}Bi_{1.440}Ti_2O_{6.210}$	Pss

A list of compositions prepared in this work is given in Table 6.1, three series are presented: U (Uchida), A and B; their positions in the phase diagram are shown in Figure 6.4. The Pss reported in the phase diagram forms for the compositions with $x'Na_2O \bullet 25\,Bi_2O_3 \bullet (75-x')TiO_2$ in mol% having $2.5 < x' < 3.75$, which corresponds to $Na_{2x}Bi_{4/3}Ti_{2\text{-}x}O_{6\text{-}x}$ with $1/15 < x < 1/10$. Series U consists of five compositions (x' = 2.5, 2.8, 3.2, 3.5, 3.75) which were prepared through a calcination at 800 °C for two hours followed by another at 1000 °C for two hours. The XRD patterns for these are presented in Figure 6.5. The presence of the NBT perovskite in these

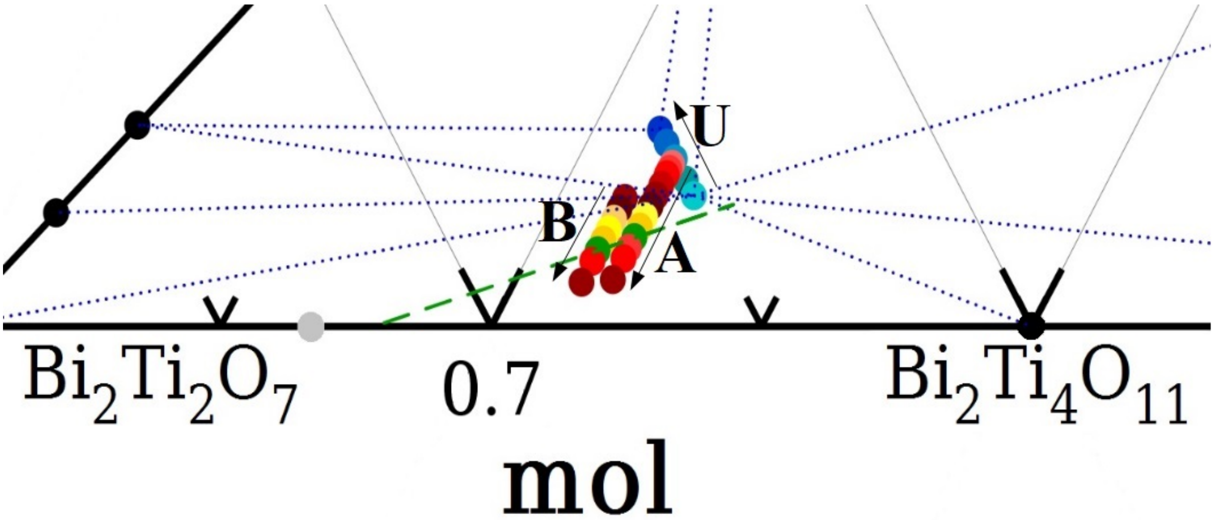

Figure 6.4: Series U, A and B in the Na_2O-Bi_2O_3-TiO_2 phase diagram (in mol fraction). Each coloured dot represents a composition listed in Table 6.1.

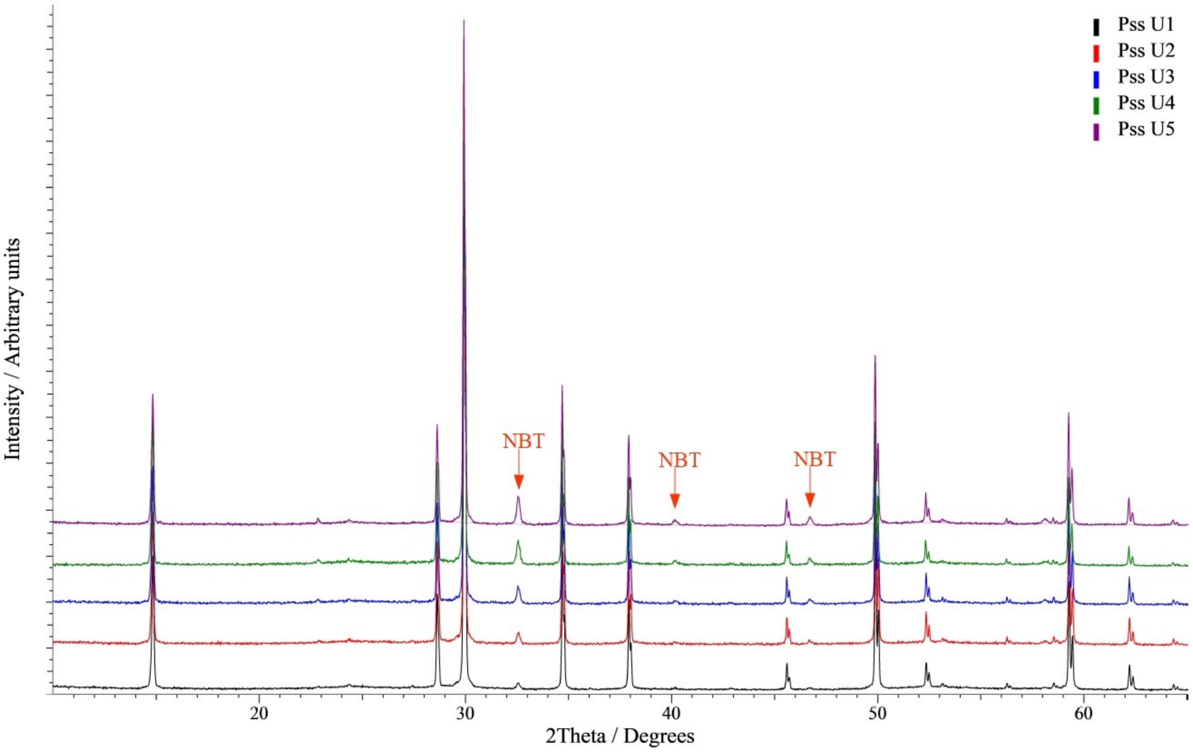

Figure 6.5: XRD patterns for the end members and three intermediate compositions along the originally reported Pss [24].

samples is clear and its concentration increases with sodium content, indicating the actual solid solution does not maintain a constant bismuth content and has lower sodium content. To determine the correct compositions, U3 and U5 were selected as the starting points for series A and B with less soda and more bismuth oxide according to $(\mathrm{x}'\text{-y})\mathrm{Na_2O}\bullet(25+y)\mathrm{Bi_2O_3}\bullet(75-\mathrm{x}')\mathrm{TiO_2}$.

For series A (x' = 3.2), the y values were: 0.1, 0.2, 0.3, 0.5, 0.7, 0.9, 1.1, 1.3, 1.5, 1.7, 1.9 and 2.3; for series B (x' = 3.75) y was taken from 1.3 to 2.5 with 0.2 intervals and y = 2.9 was also prepared. Figure 6.6 shows the peak positions of the secondary phases that can be detected in the Pss samples by XRD. Figures 6.7 and 6.8 present the diffraction patterns for a selection of these compositions after a two hour calcination at 1000 °C. For series A, XRD patterns without NBT and that do not show any additional peaks were obtained for A7, A8 and A9; for series B, phase pure pyrochlore occurs from B3 to B6. Based on these XRD data and taking into account the recommendations that Esquivel-Elizondo *et al.* make for $Bi_2Ti_2O_7$ [105] regarding the detection of $Bi_4Ti_3O_{12}$ impurities based on the yellow colour they provide the powders, the Pss forms for the A9 and B6 compositions and the formula for the solid solution is determined to be $Na_xBi_{1.9-4.6x}Ti_2O_{6.85-6.4x}$ which would follow the reaction presented in Equation 6.1, which is marked as a green dashed line in Figure 6.4. Further work indicates this holds for $0.07 < x < 0.10$ which will be denoted as Pss100x. The location of these compositions in the phase diagram is indicated in Figure 6.9.

$$(x/2)\mathrm{Na_2O} + 1/2(1.9 - 4.6\,\mathrm{x})\mathrm{Bi_2O_3} + 2\mathrm{TiO_2} \longrightarrow \mathrm{Na_xBi_{1.9-4.6x}Ti_2O_{6.85-6.4x}} \tag{6.1}$$

The mechanism in Equation 6.1 suggests the bismuth content decreases faster than the sodium content increases along the solid solution, introducing both oxygen and A-site vacancies. This is very different from the one reported by Uchida and Kikuchi ($Na_{2x}Bi_{4/3}Ti_{2-x}O_{6-x}$) where the introduction of sodium lowers the titanium and oxygen contents. The solid solution does not seem to involve a simple mechanism, for example the substitution of a Bi^{3+} and a O^{2-} by a Na^+ or of each Bi^{3+} by 3 Na^+. For ease of comparison Figure 6.9 presents (in green) the mechanism in Equation 6.1, in red and orange the "simple" mechanisms starting from $Bi_{1.9}Ti_2O_{6.85}$, and in blue the mechanism corresponding to the formula from Uchida and Kikuchi. The "simple" mechanisms would not decrease the r_A/r_B ratio and stabilise the pyrochlore. The role of Na^+ ions in stabilising the pyrochlore might be related to the more ionic character compared against Bi^{3+}, which might be preferred for the A-sites that do not have occupied O' sites associated, allowing to introduce more A-site vacancies without disrupting the bonding in the structure as much.

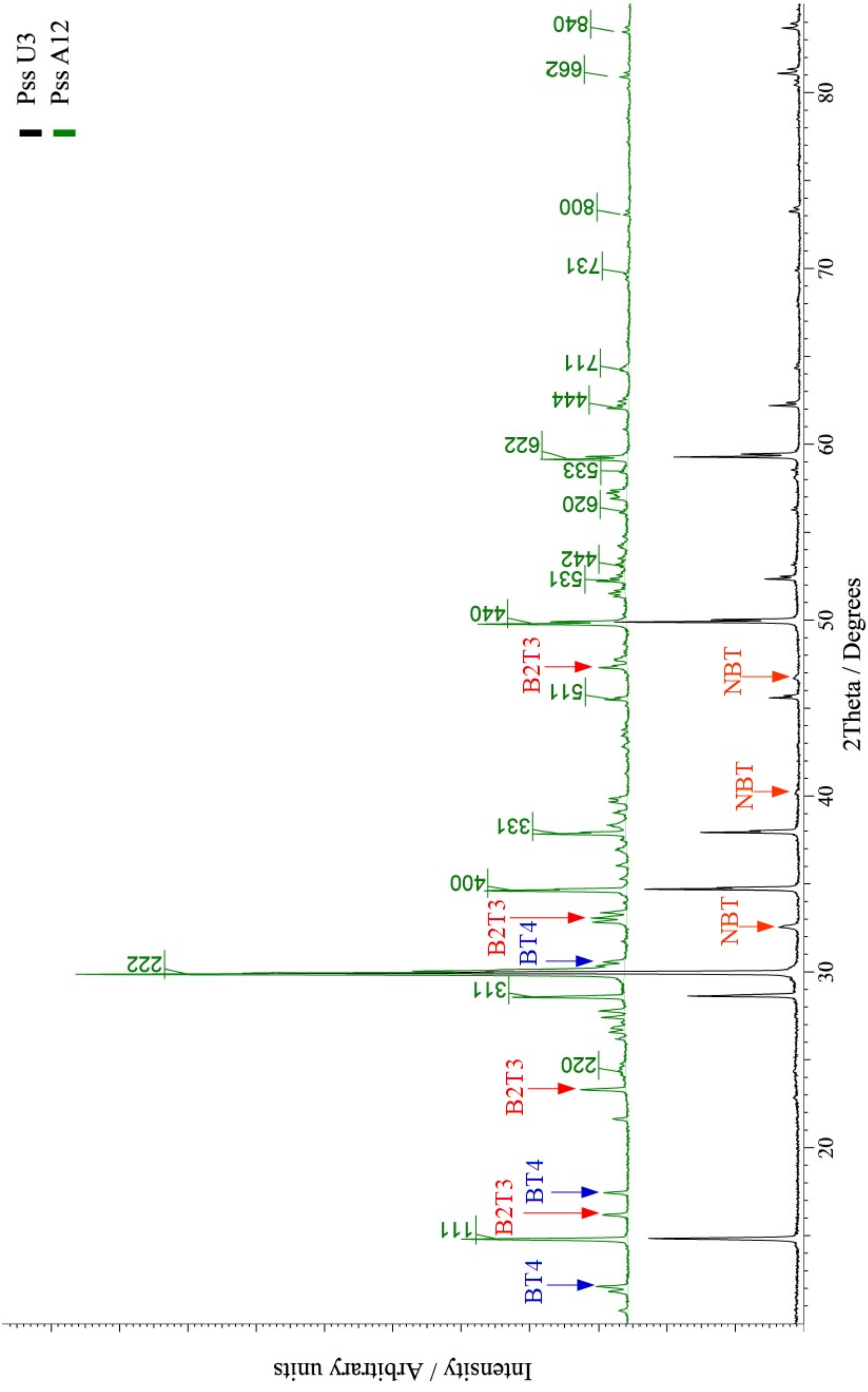

Figure 6.6: XRD patterns for U3 and A12 powders.

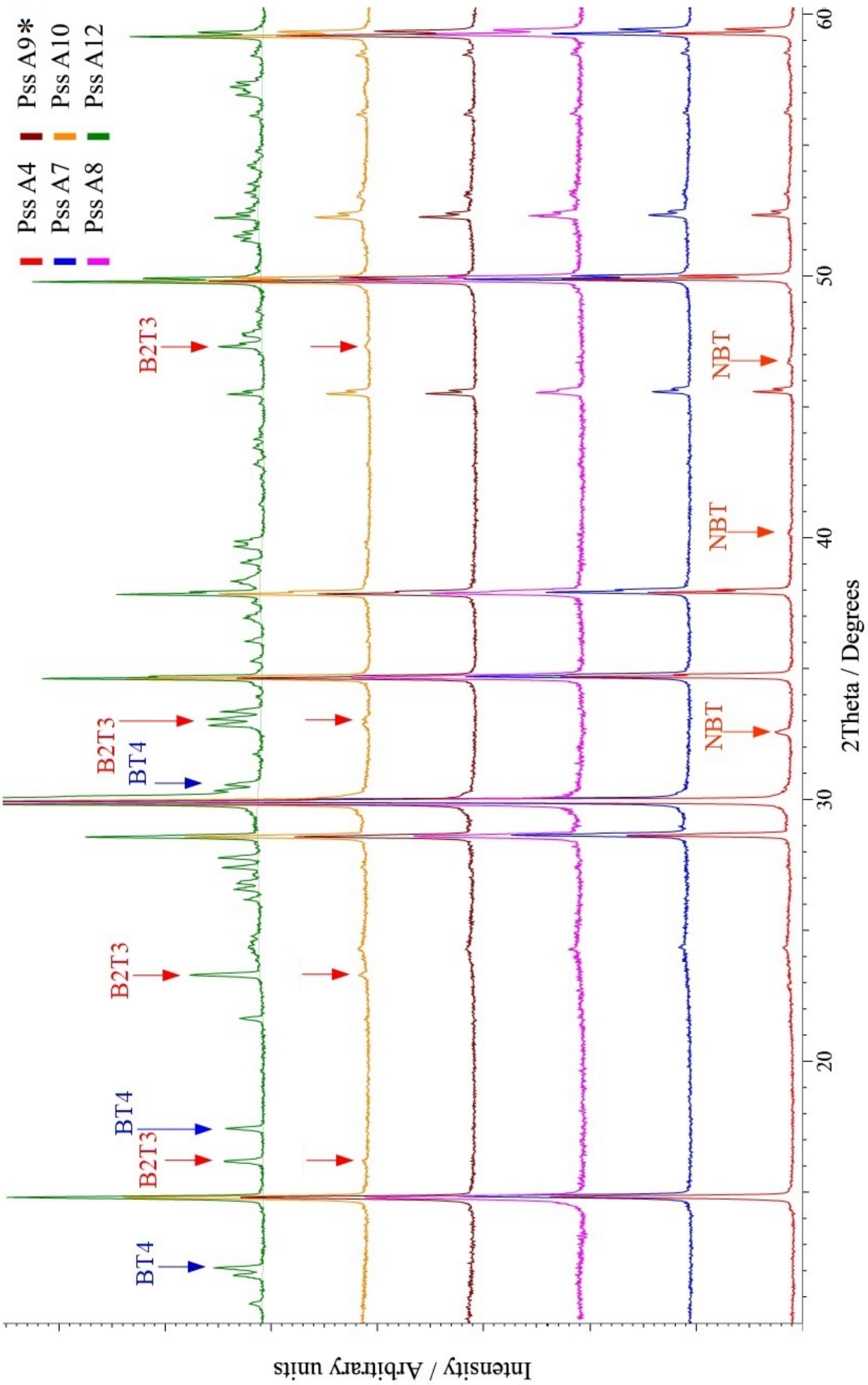

Figure 6.7: XRD patterns for selected compositions along series A.

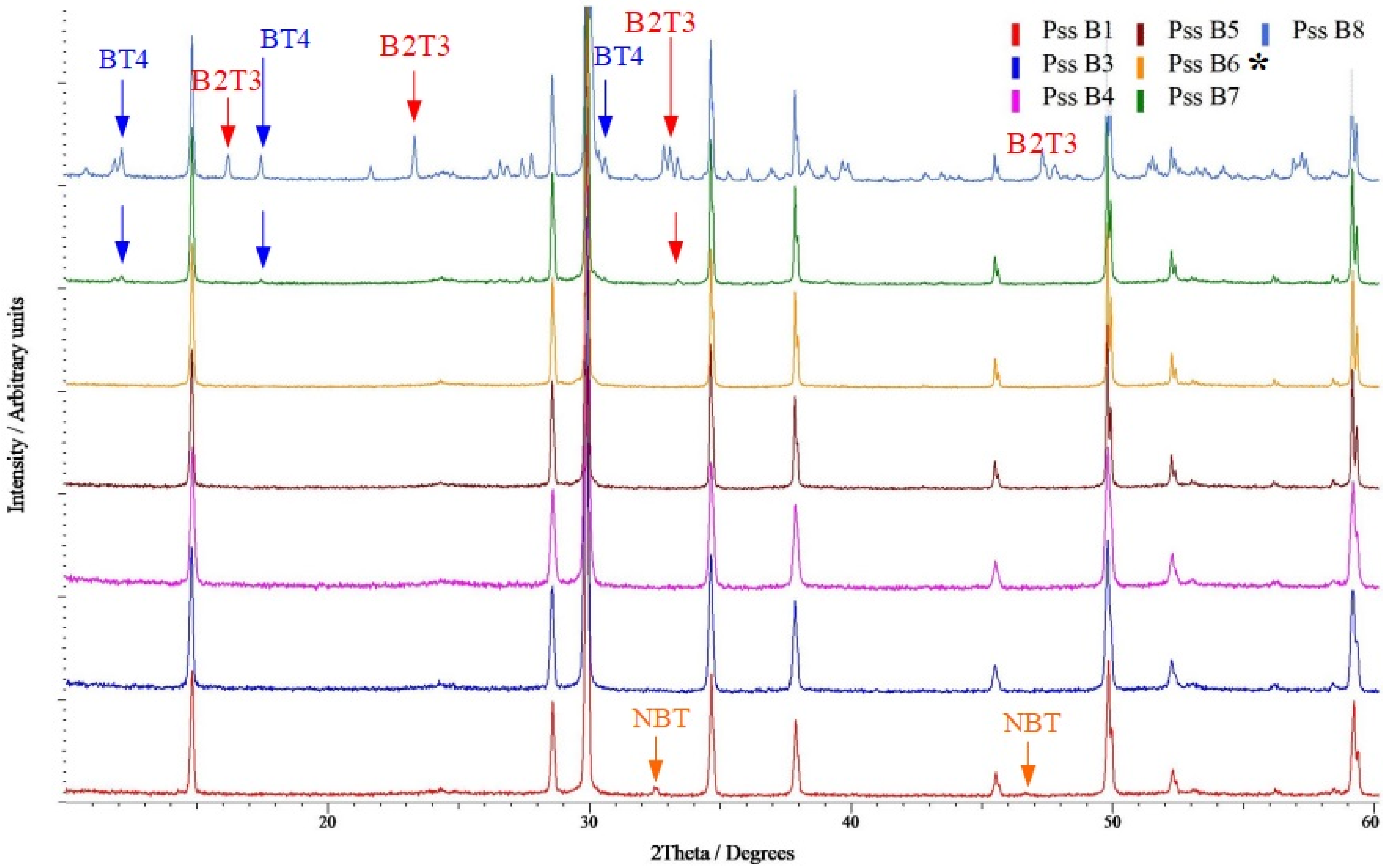

Figure 6.8: XRD patterns for slected compositions along series B.

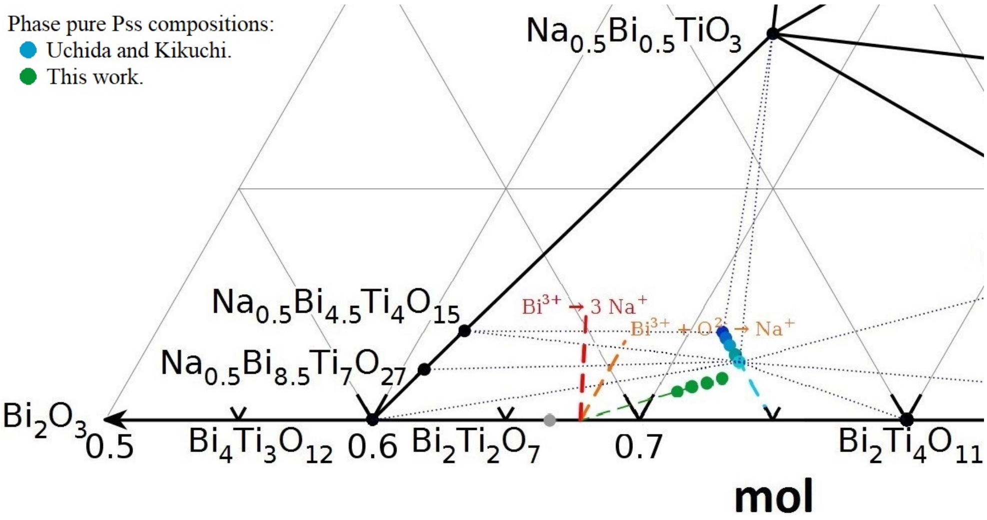

Figure 6.9: Position of diffferent doping mechanisms in the Na_2O-Bi_2O_3-TiO_2 phase diagram (in mol fraction). The red line corresponds to $Bi^{3+} \longrightarrow 3\,Na^{+}$, the orange one to $Bi^{3+} + O^{2-} \longrightarrow Na^{+}$. The green and blue dots correspond, respectively, to the Pss100x and U series in Table 6.1.

Processing of this Pss is challenging: as exemplified in Figure 6.10 the Pss powder calcined at 1000 °C releases $Bi_2Ti_4O_{11}$ when sintered at 1050 or 1100 °C for two hours buried in sacrificial powder, which can be a consequence of incongruent melting as reported for $Bi_2Ti_2O_7$ [26, 105]. One option to avoid the decomposition of the pyrochlore is to make a pellet in a single step, pressing the mixed reactants into a green pellet and taking it to the sintering temperature, in this manner the partial melting is useful to favour the product formation. The results are shown in the diffractograms in Figure 6.11. Samples prepared via this single step processing will be labelled as Pss100x RAW. Although the single step processing avoids the appearance of $Bi_2Ti_4O_{11}$ it is not an ideal solution, since it results in ceramics with lower densities. For example, a pellet with 92% of the theoretical density is obtained from phase-pure calcined powder fired at 1100 °C, while a pellet from the mixed reactants fired at the same temperature results in only 75% density.

The most likely reason for the poor densification is the release of CO_2 from Na_2CO_3 during the firing process. Single step Pss samples processed at 1200 °C attain nearly 90% density but as evidenced by the EDX analysis shown in Figure 6.12 they are contaminated with aluminium. It is probable that the Na_2O-Bi_2O_3-based liquid reacts with the Al_2O_3 crucible and facilitates the introduction of Al^{3+} into the product. The purity of the calcined powders used for the determination of the solid solution compositions was verified through EDX; spectra for one of the compositions are presented in Figure 6.13. No Al is detected in the powders calcined at 1000 °C. If the same powder is then fired at 1020 °C, Al is detected in the sample as shown by the spectrum in Figure 6.14. However a pellet prepared at 1100 °C using sacrificial powder

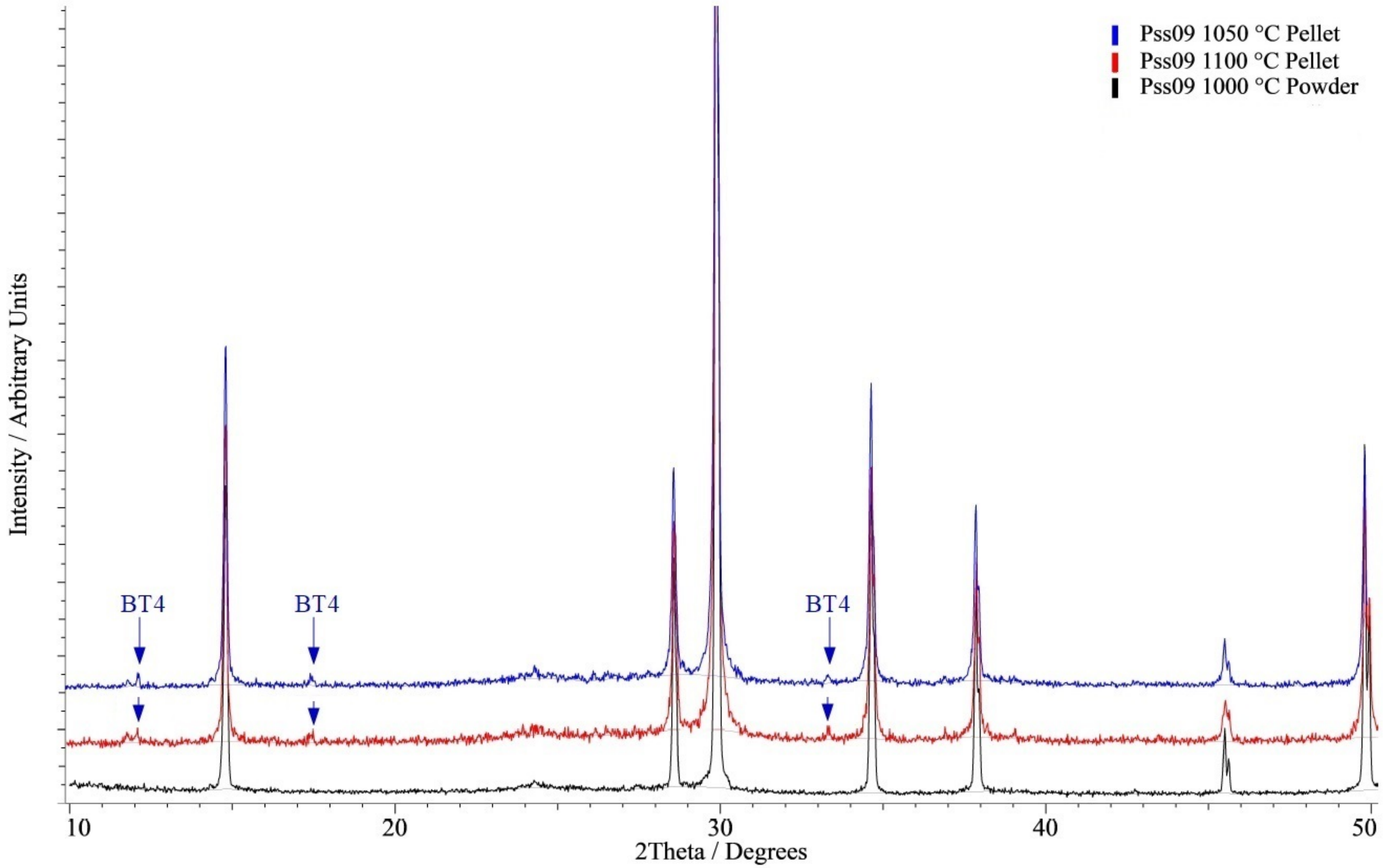

Figure 6.10: XRD patterns for A9 (Pss09) powder calcined at 1000 °C (bottom) and pellets sintered at 1050 (top) and 1100 °C (middle).

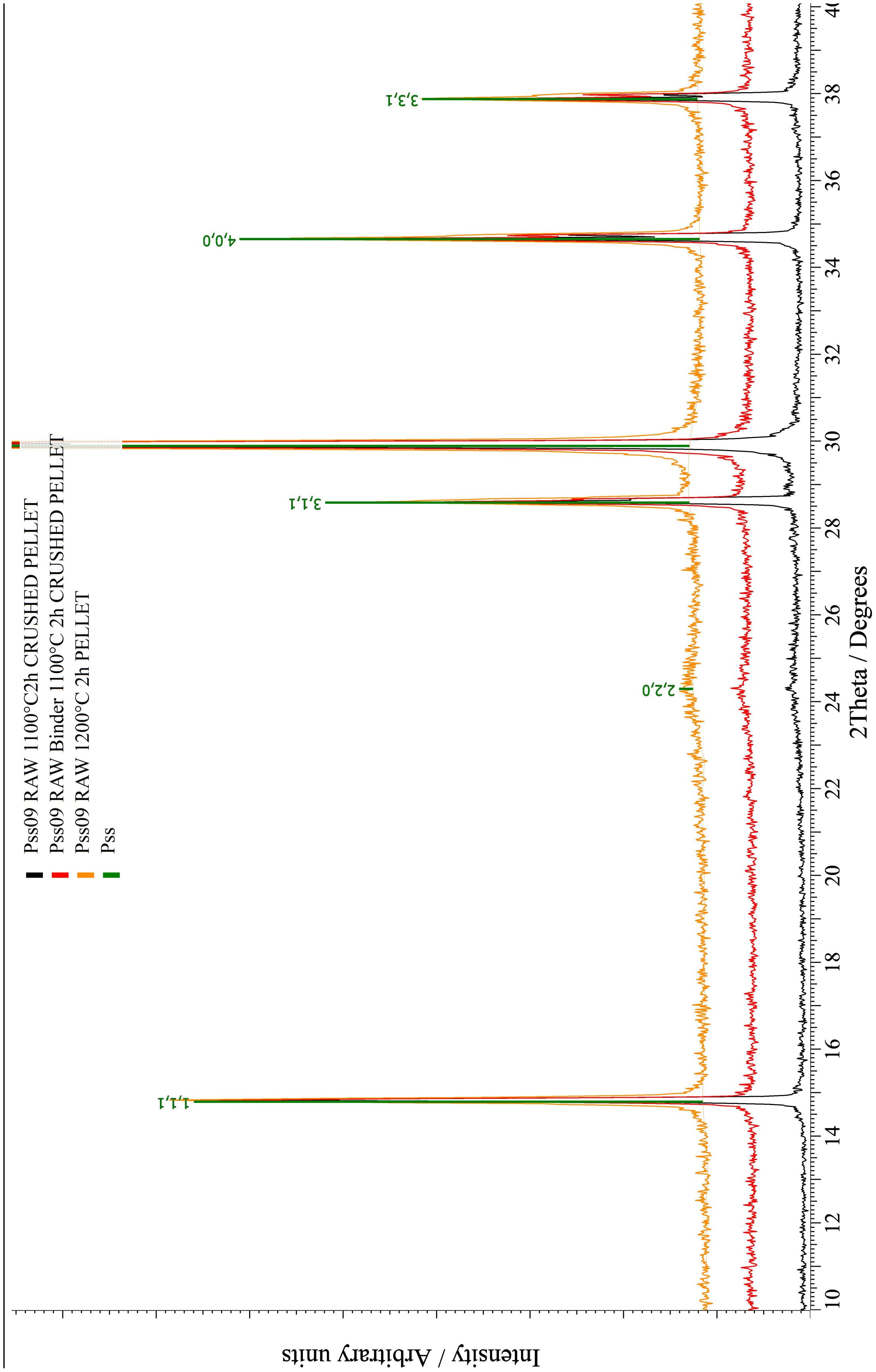

Figure 6.11: XRD patterns for Pss09 pellets prepared through a single step process.

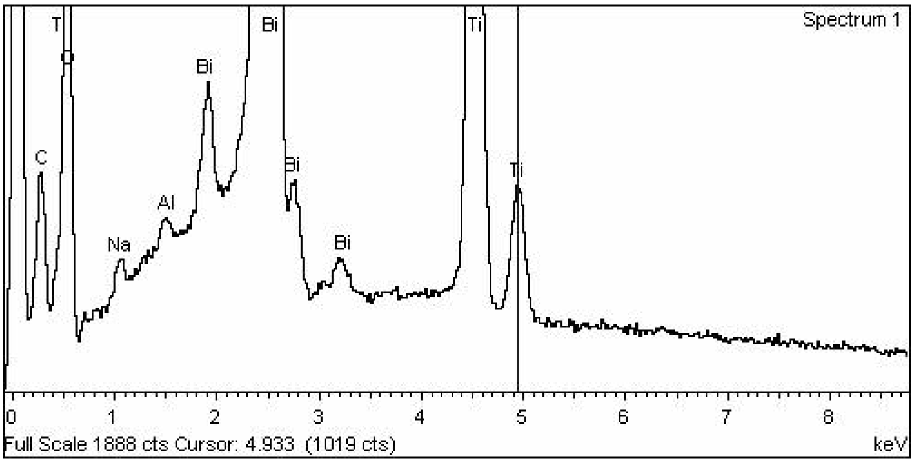

Figure 6.12: EDX spectrum on the polished surface of a Pss09 pellet sintered at 1200°C from the mixed reactants.

does not show signs of Al contamination as evidenced in Figure 6.15, suggesting the sacrificial powder is sufficient to prevent contamination at this temperature. Micrographs from secondary and back-scattered electrons of thermally etched Pss09 pellets sintered at 1100 °C are displayed in Figure 6.16 and exemplify the phase purity and homogeneity of the sample, and show grain sizes of $\sim 10\,\mu\mathrm{m}$.

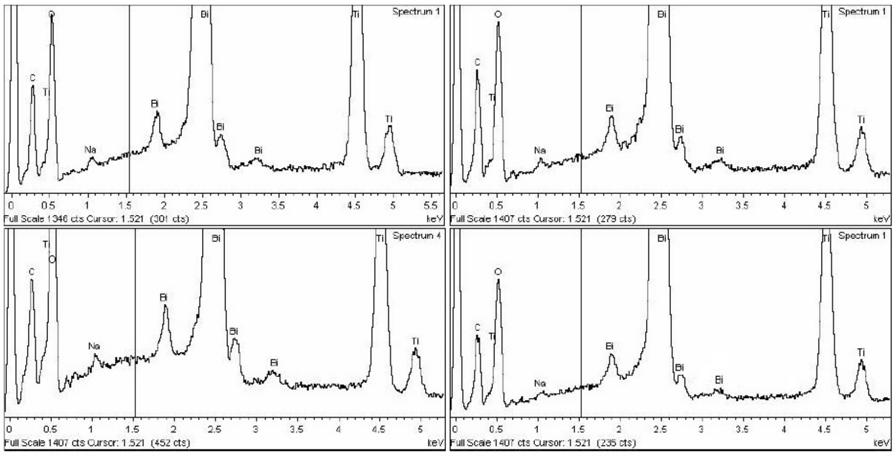

Figure 6.13: EDX spectra on calcined Pss09 powder. The line marks the position where a peak from Al could be expected.

Various attempts were made to improve the density of Pss pellets sintered at 1100 °C by pre-reacting the Na_2CO_3 and Bi_2O_3 mixture, adding binder, SiO_2 or B_2O_3, however none of these offered a satisfactory result. To make sintering at 1200 °C viable without a reaction with the crucible a few alternatives were tried, such as sintering on top of Ti foil under flowing Ar.

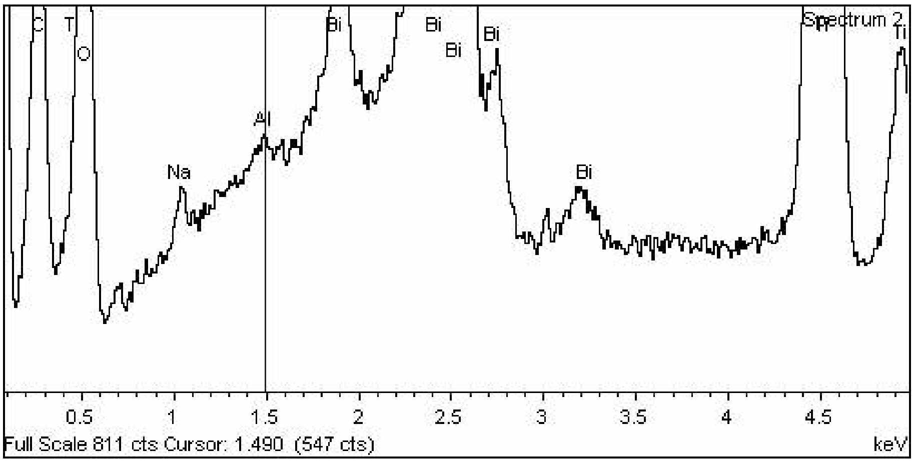

Figure 6.14: EDX spectra on calcined Pss09 powder taken to 1020 °C.

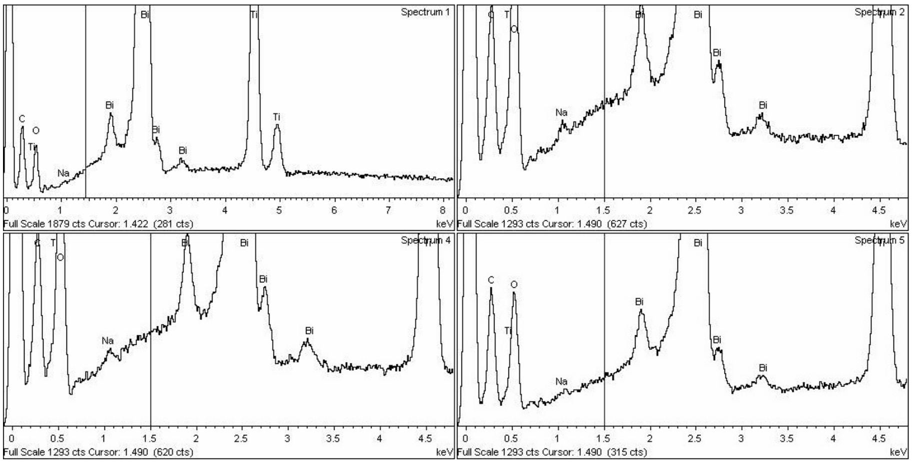

Figure 6.15: EDX spectra on Pss pellet sintered at 1100 °C. The line marks the position where a peak from Al could be expected.

The processing conditions that produce dense (~95 %), clean samples are firing the Pss pellet on top of a previously sintered NB51T pellet. A diffraction pattern of a pellet produced in this manner is presented in Figure 6.17. It is highly noticeable that the relative intensities of the peaks have been strongly affected, the Miller indices -mainly the (311) and (622) peaks- strongly suggest that this is a consequence of preferred orientation in the samples, suggesting that the pyrochlore has grown textured.

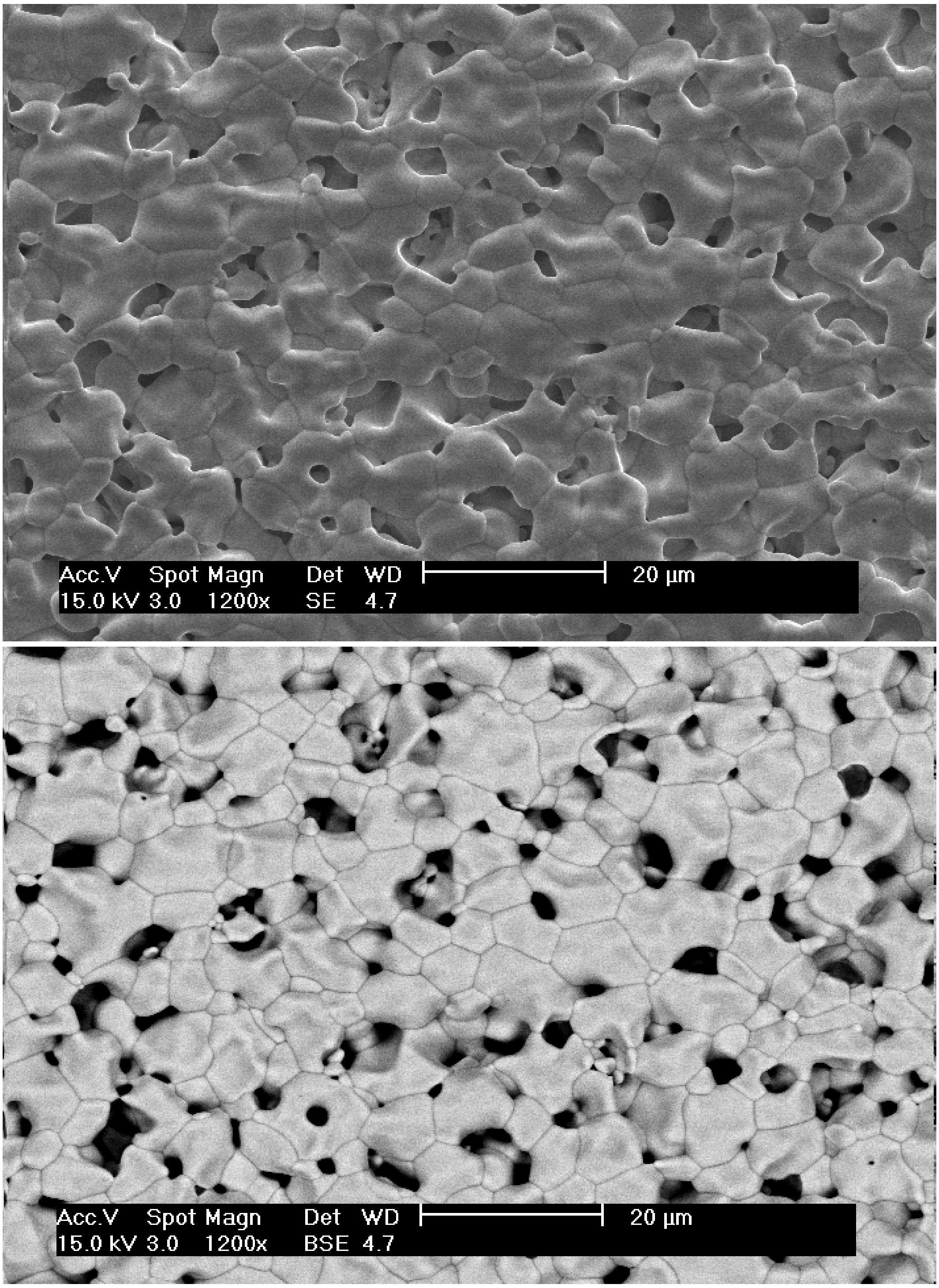

Figure 6.16: SEM micrographs of thermally etched Pss09 sintered at 1100°C. Top: Secondary electrons image. Bottom: Back-scattered electrons image.

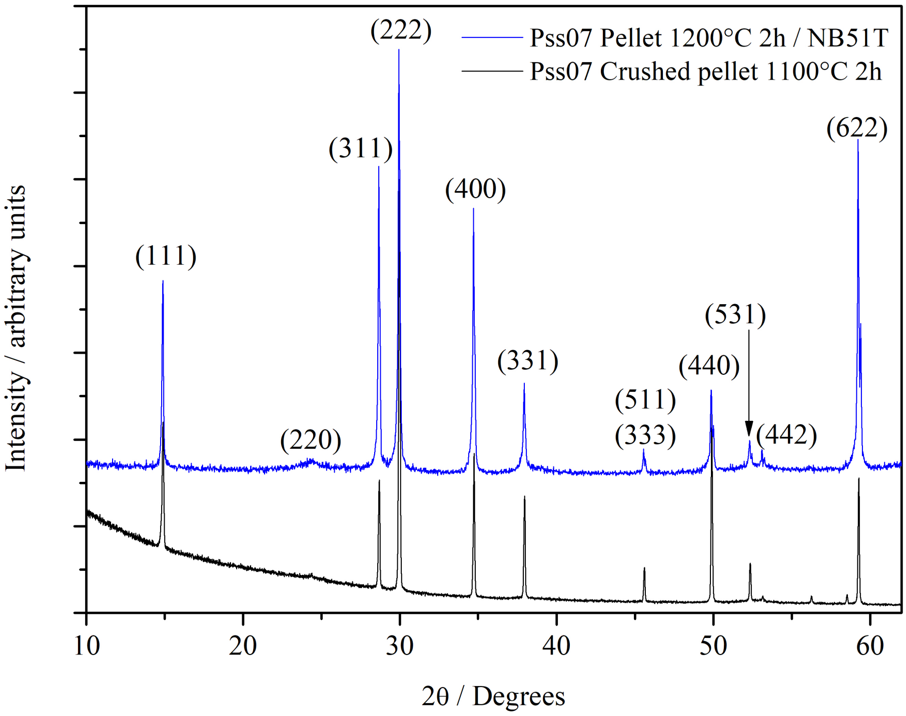

Figure 6.17: XRD patterns of a crushed Pss07 pellet sintered at 1100 °C and a Pss07 pellet sintered at 1200 °C on top of an NB51T pellet.

6.2.2 Neutron diffraction experiments

Neutron diffraction data for four Pss samples were collected on POLARIS at ISIS. For two compositions (Pss07 and Pss10) the samples were crushed pellets from single step processing at 1100 °C and the other two compositions (Pss08 and Pss09) were powders calcined at 1000 °C. For Pss07 and Pss10, variable temperature data were also collected, between 4.2 K and 600 °C. As mentioned in Chapter 3, the room temperature measurements were done first and the high temperature measurements were done last on heating. Before heating and collecting data, the furnace was evacuated to $10^{-5} \sim 10^{-4}$ mbar. Figure 6.18 presents the diffraction patterns collected at room temperature for the four samples on the 90 ° detector bank, these patterns show only Pss07 to be phase pure and the other three samples to contain small amounts of TiO_2.

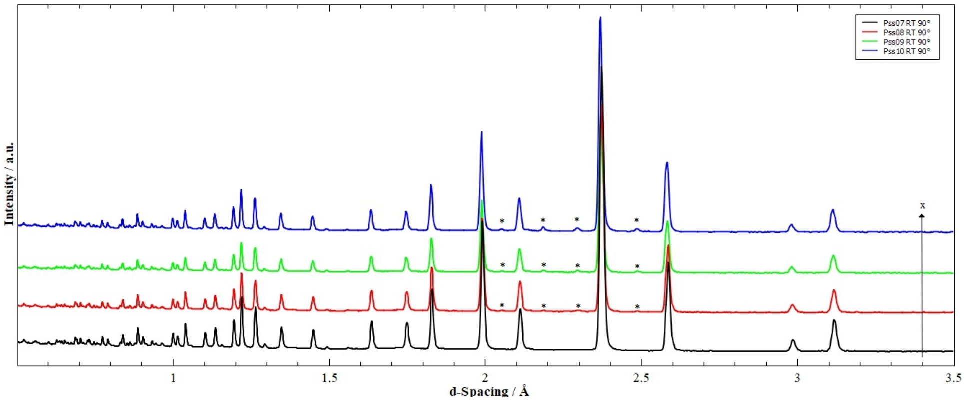

Figure 6.18: Neutron diffraction patterns collected on the 90 ° detector bank for Pss with x = 0.07, 0.08, 0.09, 0.10. (*) Marks peaks from TiO_2.

When removed from the vanadium cans, the samples that were heated to 600 °C had darkened turning nearly black. XRD patterns collected on the darkened powders (Figure 6.19) indicate they conserve the pyrochlore structure, a small increment in the amount of TiO_2 present can be appreciated which is probably a consequence of small losses of sodium or bismuth under the high temperature and vacuum. Figure 6.20 presents EDX spectra from Pss07 pristine powder and darkened powder from the ND experiments. There is no significant difference between both spectra, although the main peak from vanadium would overlap with a secondary titanium peak. These EDX results suggest the darkening of the Pss powders is not due to vanadium from the sample cans that could have reacted and incorporated into the structure but rather due to a redox process. This was confirmed by annealing these dark powders at 700 °C for two hours under flowing O_2, N_2 or Ar which returned them to the original colour. Pristine powder annealed under 5% H_2 in N_2 at 400 °C turned dark, showing these materials can be reduced.

The temperature of the sample can and furnace pressure during the ND experiments are shown in Figure 6.21. Data for NB49T-NN 30% are included as a reference for the expected behaviour: a sharp increment of the pressure when the temperature increases and its gradual decrease as a temperature is held (this is how the NB49T-NN 30 % data set behaves up to 500 °C). For the Pss, below 400 °C the pressure decays during each isotherm as expected (except for a small increase at the end of the 300 °C isotherm for Pss10); however, above this temperature the Pss samples start showing a clear increase in pressure during the isotherms. At 500 and 600 °C the pressure for the Pss samples goes through a maximum. This information indicates the pyrochlores were reducing under the vacuum required for the furnace in the ND experiments. Since the oxygen contents in the samples were changing during the data collection, the results of the high temperature refinements are not appropriate for further analysis.

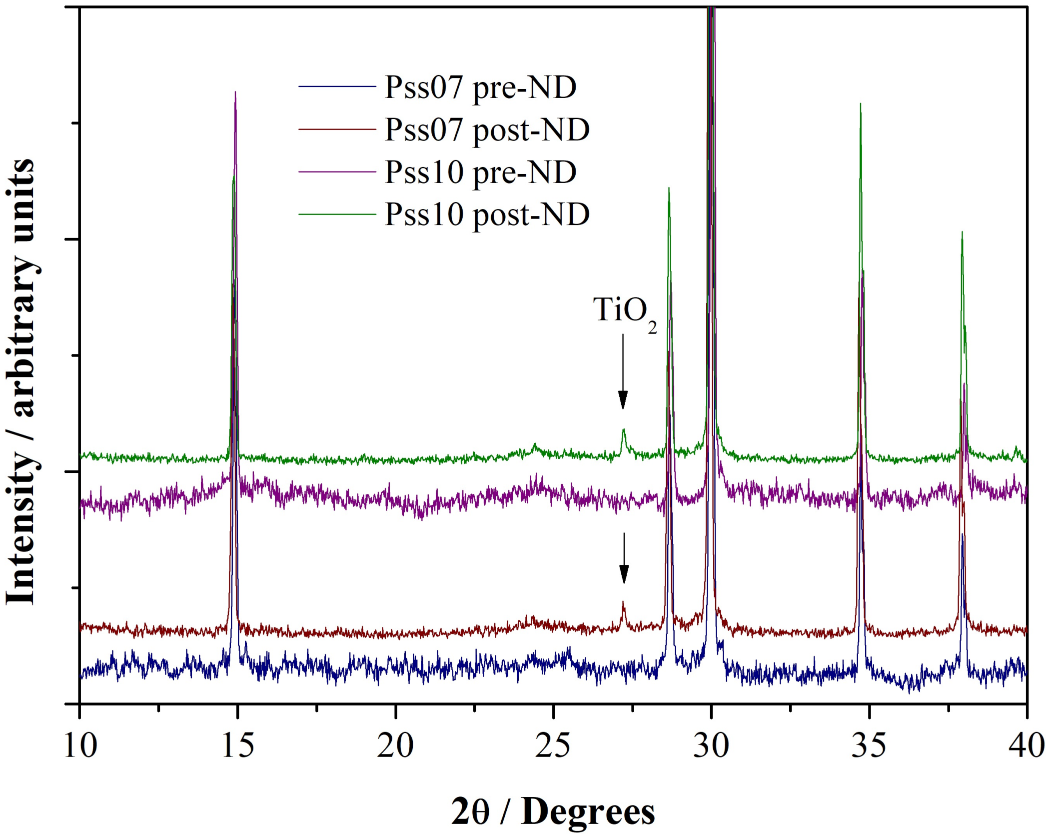

Figure 6.19: XRD patterns of Pss07 and Pss10 before and after the ND experiments.

A thermogravimetric analysis under air of the light (pristine powder) and dark (after the ND experiments) Pss10 powders is presented in Figure 6.22. Complex behaviour is observed. Both types of powder show a small loss of mass during the initial stages of the measurement and both start recovering weight as the heating continues. The pristine powder starts loosing much more weight above 100 °C and stops changing around 700 °C. For the dark post-ND sample,

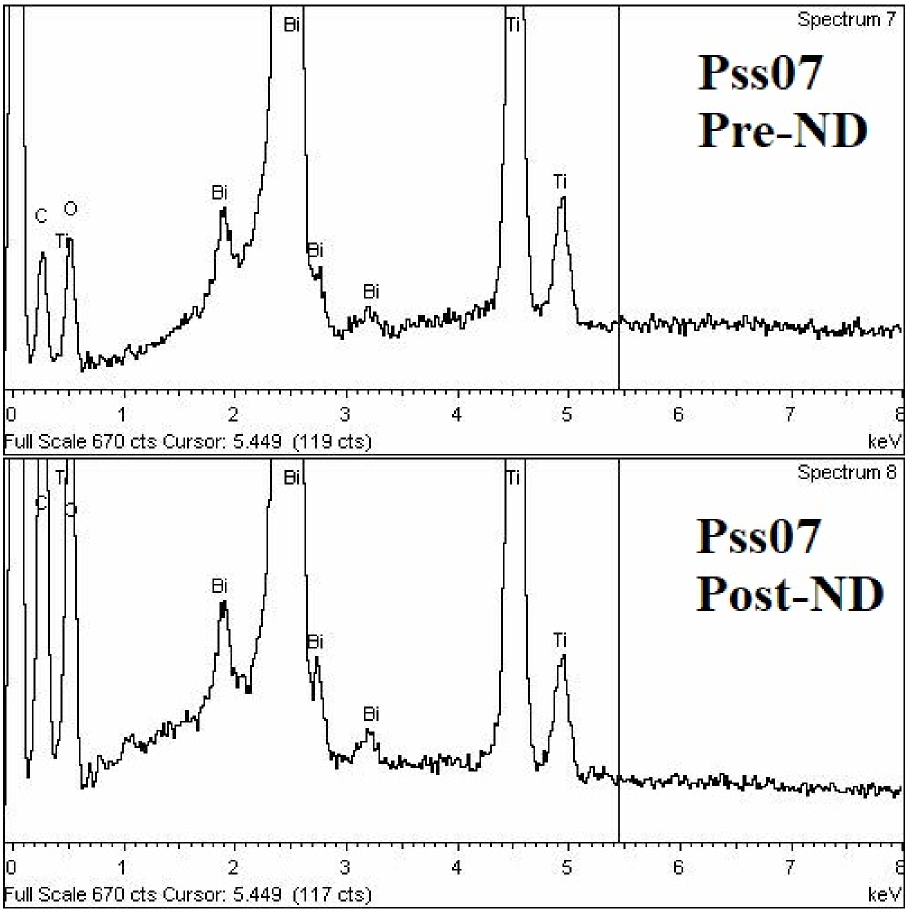

Figure 6.20: EDX spectra for Pss07 powders before and after the ND experiments. The line below 4.5 keV indicates the position for a secondary Vanadium peak.

after the initial mass loss it slowly gains weight up to ∼150 °C. Then a slow decrease of mass is observed until ∼330 °C, followed by a mass gain up to ∼520 °C leaving the sample with a higher mass than it originally had. From 520 to 620 °C the mass decreases slightly and then seems to stabilise at a mass still higher than the original. The most important feature is the post-ND sample ending with higher relative mass than the pre-ND sample. This is consistent with the idea that it had been reduced under the vacuum during the ND experiments and is being re-oxidised in the TGA. The initial mass loss observed for both samples probably corresponds to adsorbed water. The larger loss observed for the pre-ND sample could be due to bound water. For the post-ND sample, the loss of bound water might be occurring simultaneously with the re-oxidation, giving rise to the more complex profile.

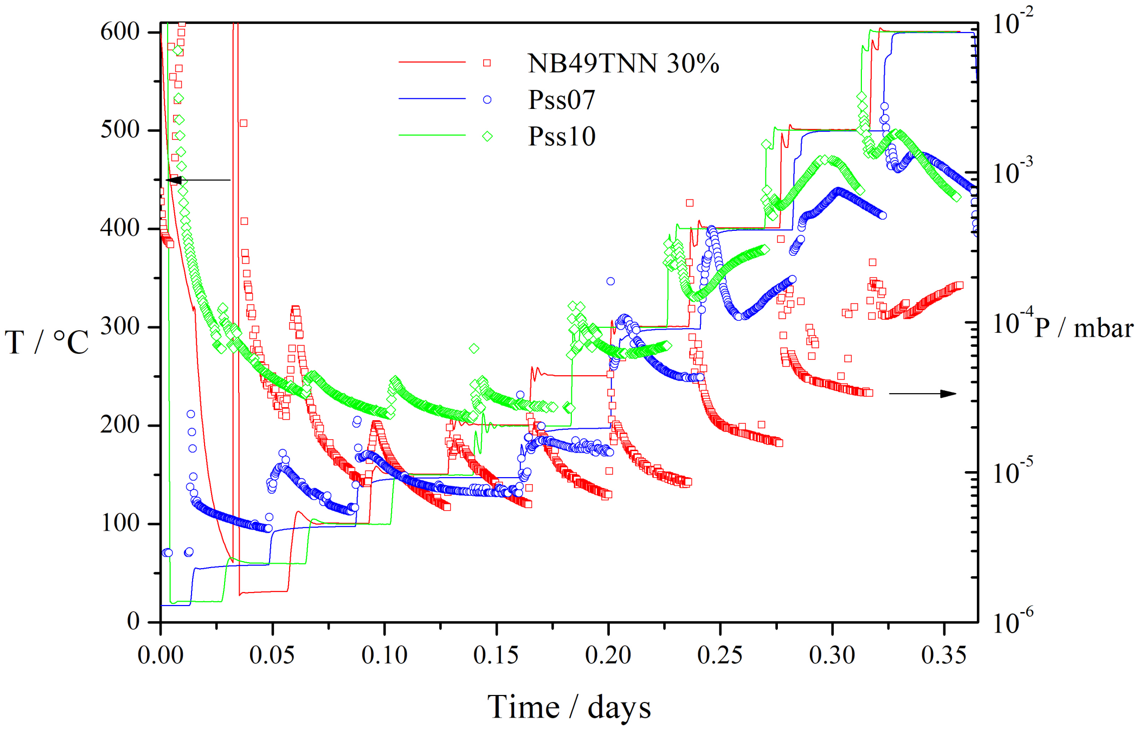

Figure 6.21: Evolution of temperature (solid lines) and pressure (open symbols) in the furnace during neutron diffraction experiments for Pss07, Pss10 and NB49T-NN 30%.

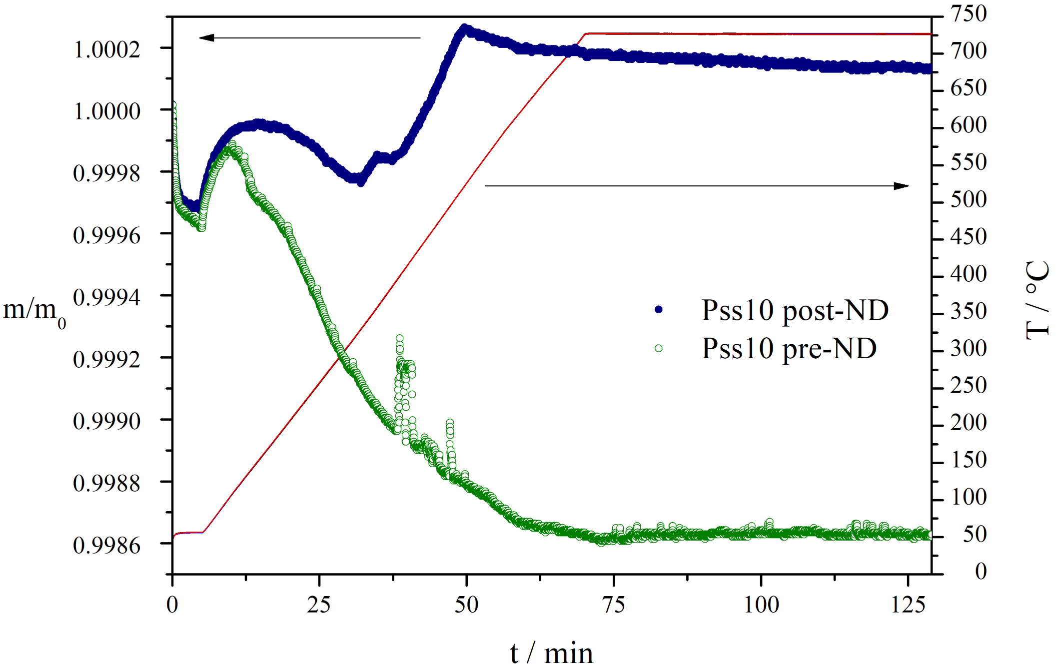

Figure 6.22: TGA profiles for Pss10 crushed pellets under air. Comparing pristine powder (open symbols) and powder used in the ND high temperature experiments (filled symbols).

Analysis and Rietveld refinements of neutron diffraction data

The first refinement made was for the room temperature data from Pss07, which started with the structure published by Esquivel-Elizondo *et al.* for $Bi_2Ti_2O_7$ [105]. The room temperature refinements for the other compositions were started from the refined model of the previous (lower x value) composition, each variable temperature refinement started with the results from the previous temperature data. The refinement strategy followed starts with the background being fitted with shifted Chebyschev polynomials starting with 12 terms for each histogram and adjusting if necessary, then the lattice parameter was refined. For the room temperature refinements, the diffractometer constants (DIFC) of the lower resolution detector banks and the DIFA values accounting for the energy dependence of the neutron absorption by the sample on all banks were refined after the lattice parameter. Another room temperature measurement was made with the Pss07 sample loaded in the furnace to perform a refinement where the DIFA and DIFC constants were refined while fixing the lattice parameter and structural parameters to the values obtained from the refinement of the sample outside the furnace. Those DIFA and DIFC values were then kept fixed for the subsequent refinements of high temperature data.

The next refined parameters are the peak profiles (function 3 in GSAS). The atomic positions of the bismuth/sodium ions and O1 ions were refined starting with the Bi ions (since they are the strongest scatterers) alongside the Na ions which have been constrained to have the same position and thermal displacement parameter as the Bi ions, then the O1 position was refined separately and finally both positions simultaneously. The same strategy was used for the isotropic thermal displacement parameters (Uiso's) starting with Bi/Na, followed by O1 and O2, then Ti and finally all simultaneously. Afterwards the atomic positions were refined simultaneously with the thermal displacement parameters. The final step was the refinement of the fractional site occupancies, using the same logic used for the Uiso's. The occupancies of Bi, O1, O3, and Ti were not found to vary significantly from the previous refinement and were therefore fixed to the initial values, refining the sodium occupancy led to unstable refinements or unphysical results, hence it was not actually refined but adjusted according to the nominal Na/Bi ratio. As an example, the progress of the refinement for the 600 °C data of Pss07 is presented in Table 6.2.

For the Pss07 sample only pyrochlore peaks are observed in Figure 6.18. A Rietveld plot corresponding to the 90 degree detector bank is shown in Figure 6.23, where clearly all peaks are well described by the model structure. In the other three samples some rutile is detected. Rietveld refinements indicate that for Pss10, the sample with highest TiO_2 content, the amount is barely above 1 wt%. The amount of rutile increases slightly with sodium content, suggesting the mechanism in Equation 6.1 is not entirely correct and the actual solid solution has less A-

Table 6.2: Progress of the Rietveld refinement for Pss07 at 600 °C.

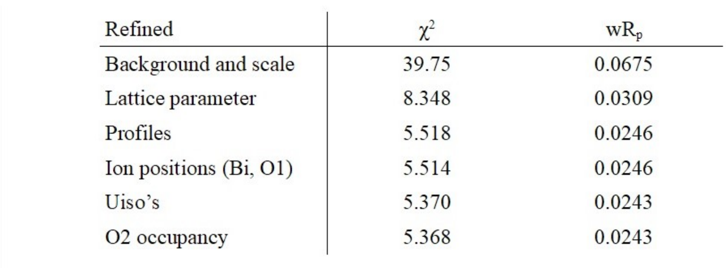

Refined	χ^2	wR_p
Background and scale	39.75	0.0675
Lattice parameter	8.348	0.0309
Profiles	5.518	0.0246
Ion positions (Bi, O1)	5.514	0.0246
Uiso's	5.370	0.0243
O2 occupancy	5.368	0.0243

site vacancies. As an example, the refined atomic coordinates obtained for Pss07 are presented in Table 6.3. Tables 6.4 and 6.5 contain, respectively, bond lengths and angles extracted from the refined models. The metal-oxygen bond lengths obtained have reasonable values and the angles are consistent with the coordinations expected from a pyrochlore, i.e. octahedral for the B-site, distorted cubic for the A-site and tetrahedral for the anions. Lattice parameters obtained from the refinements, wRp and χ^2 values are presented in Table 6.6. In Figure 6.24 a contraction of the cell is observed with increasing sodium content, which confirms that there is a solid solution. Since Bi^{3+} and Na^+ have very similar sizes [80], this is then a consequence of the vacancies introduced across the solid solution. The contraction of the cell is consistent with the idea that a smaller r_A/r_B ratio is involved in stabilising these pyrochlores.

Table 6.3: Refined atomic coordinates for Pss07. The errors quoted between brackets correspond to 2σ. Quantities without quoted errors were not refined.

	x	y	z
Na^+/Bi^{3+}	0.0147(4)	0.0147(4)	-0.0295(4)
Ti^{4+}	0.5	0.5	0.5
O^{2-} 1	0.125	0.125	0.43120(8)
O^{2-} 2	0.125	0.125	0.125

The compositions for refined models shown in Table 6.6 consistently show a higher oxygen content than that expected to neutralise the charge of the cations. This excess also increases with sodium content. This can be due to structurally bound water, consistent with the mass loss seen on TGA. Since the ”excess” is larger for compositions with more sodium, the conclusion is that the presence of Na^+ in the structure makes it more hygroscopic, as sodium compounds commonly are. Another possibility is that some of the bismuth is present as Bi^{5+} ions which could be stabilised by the electropositive nature of Na^+. To fully account for the oxygen ”excesses” listed in Table 6.6 24 % of the bismuth in Pss07 would have to be Bi^{5+} which would

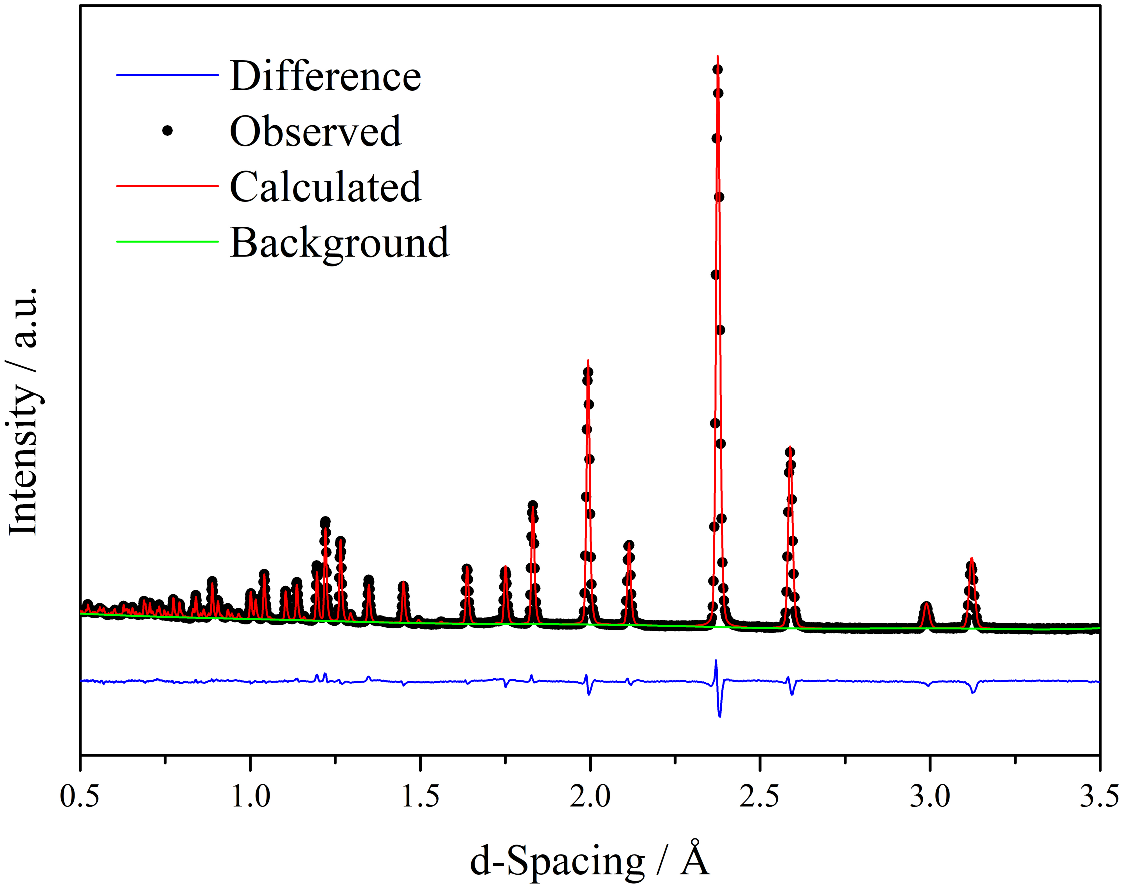

Figure 6.23: Rietveld plot for the 90 degree detector bank data from a multi-bank refinement of Pss07 neutron diffraction data at room temperature using space group $Fd\bar{3}m$.

Table 6.4: Bond lengths, in Angstroms, from Rietveld refinements of room temperature neutron diffraction data for the Pss using space group $Fd\bar{3}m$. The errors quoted between brackets correspond to 2σ.

	Bi-O1	**Bi-O2**	**Ti-O1**
Pss07	2.252(3), 2.457(1), 2.823(2), 2.988(2)	2.271(6), 2.272(6)	1.9630(3)
Pss08	2.248(3), 2.455(2), 2.822(2), 2.989(2)	2.270(7), 2.272(7)	1.9626(3)
Pss09	2.251(3), 2.455(2), 2.817(2), 2.982(3)	2.267(8), 2.270(8)	1.9617(3)
Pss10	2.256(2), 2.457(1), 2.8068(8), 2.9697(8)	2.257(5), 2.276(5)	1.9623(4)

increase across the solid solution to 39 % in Pss10. Naturally, it is possible that both Bi^{5+} and structurally bound water are present in the samples. As hydrogen atoms are not considered in the refinements it is not possible to directly compare the "excess" oxygen in Table 6.6 with the mass loss in Figure 6.22. This is further complicated by the fact that the ND and TGA ex-

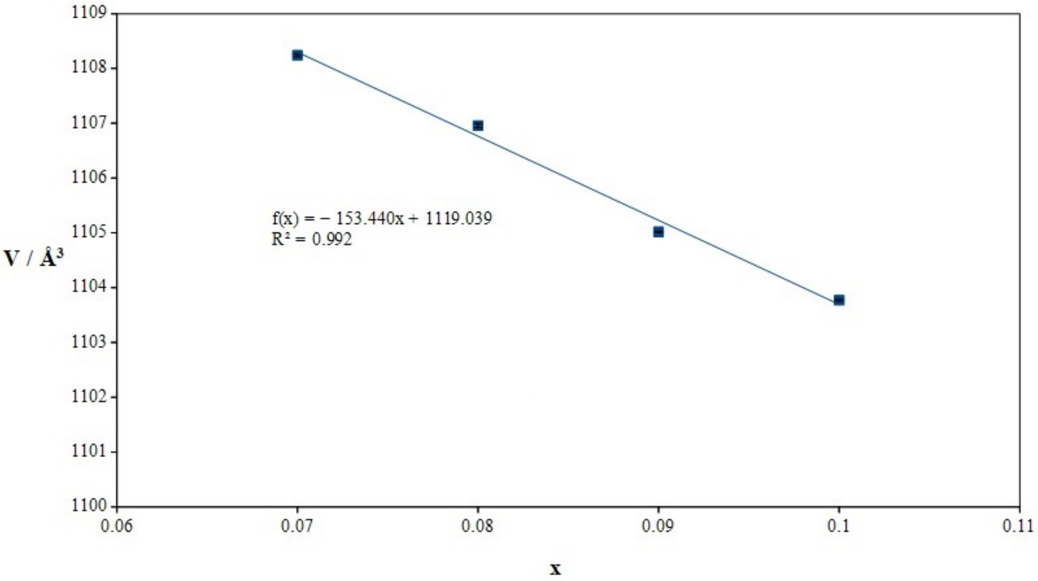

Figure 6.24: Refined cell volumes at room temperature accross the Pss.

Table 6.5: Bond angles, in degrees, from Rietveld refinements of room temperature neutron diffraction data for the Pss using space group $Fd\bar{3}m$.* Other angles obtained in the model are excluded from this table. The errors quoted between brackets correspond to 2σ.

	O1-Ti-O1	**Bi-O2-Bi***	**Ti-O1-Bi***	**Ti-O1-Ti**
Pss07	87.49(3), 92.51(3), 180	104.62(3), 107.84(3), 109.48(5), 110.29(3), 113.91(3)	104.65(5), 105.34(3), 111.54(5), 112.15(6)	137.47(5)
Pss08	87.46(3), 92.54(3), 180	104.60(3), 107.83(4), 109.46(6), 110.31(3), 113.92(3)	104.67(5), 105.35(4), 111.59(6), 112.19(7)	137.42(5)
Pss09	87.43(3), 92.57(3), 180	104.65(3), 107.87(4), 109.46(6), 110.29(3), 113.87(3)	104.69(5), 105.35(4), 111.54(6), 112.10(8)	137.38(5)
Pss10	87.30(4), 92.70(4), 180	104.76(2), 107.98(2), 109.39(4), 110.28(2), 113.76(1)	104.80(4), 105.36(3), 111.48(4), 11.90(4)	137.19(6)

periments were run under very different conditions (i.e. vacuum for ND) at different locations and different times. However, the total mass loss (∼0.14 %) observed for the pre-ND Pss10 in Figure 6.22 is somewhat comparable to the mass of the ”excess” oxygen (∼0.04 %). More detailed results regarding the compositions are presented in Table 6.7. During refinement the occupancies of the Ti, O1 and O3 sites did not change significantly from the initial values, and were therefore fixed to said values for the remainder of the refinements.

Table 6.6: Summary of Rietveld refinements of room temperature neutron diffraction data for the Pss using space group $Fd\bar{3}m$. The uncertainties quoted between parenthesis correspond to 2σ.

Sample	χ^2	R_{wp}	a / Å	Refined composition	Oxygen ”excess”
Pss07	14.56	0.043	10.34852(8)	$Na_{0.072}Bi_{1.656}Ti_2O_{6.841}$	0.321
Pss08	11.16	0.045	10.3445(2)	$Na_{0.084}Bi_{1.656}Ti_2O_{6.879}$	0.353
Pss09	12.26	0.044	10.3385(2)	$Na_{0.096}Bi_{1.620}Ti_2O_{6.879}$	0.401
Pss10	15.4	0.051	10.3346(3)	$Na_{0.108}Bi_{1.596}Ti_2O_{6.894}$	0.446

Table 6.7: Refined site occupancies of Pss from Rietveld refinements of room temperature neutron diffraction data. The multiplicity of each site is quoted between square brackets. Na occupancy was adjusted according to the nominal Na:Bi ratio. The errors quoted between brackets correspond to 2σ.

Sample	F Bi [96]	F O2 [8]	Refined composition	Nominal composition
Pss07	0.138(<0.001)	0.841(8)	$Na_{0.072}Bi_{1.656}Ti_2O_{6.841}$	$Na_{0.070}Bi_{1.578}Ti_2O_{6.402}$
Pss08	0.138(<0.001)	0.88(1)	$Na_{0.084}Bi_{1.656}Ti_2O_{6.879}$	$Na_{0.080}Bi_{1.532}Ti_2O_{6.338}$
Pss09	0.135(<0.001)	0.88(1)	$Na_{0.096}Bi_{1.620}Ti_2O_{6.879}$	$Na_{0.090}Bi_{1.486}Ti_2O_{6.274}$
Pss10	0.133(<0.001)	0.89(1)	$Na_{0.108}Bi_{1.596}Ti_2O_{6.894}$	$Na_{0.100}Bi_{1.440}Ti_2O_{6.210}$

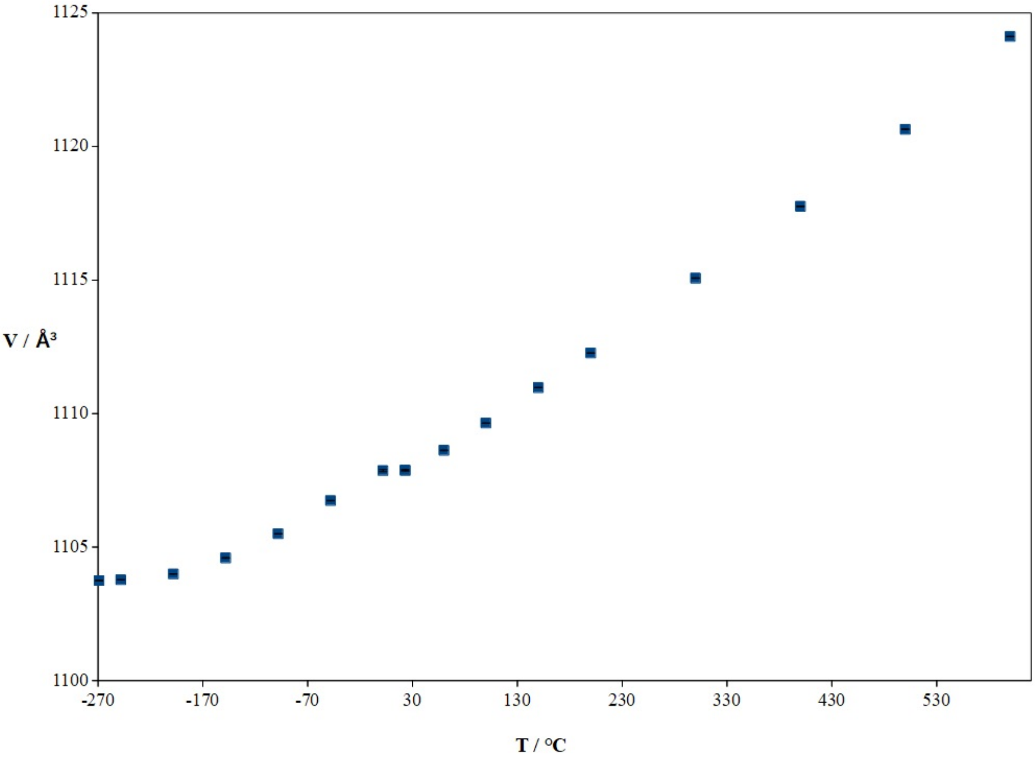

Figure 6.25: Refined cell volume of Pss07 as a function of temperature.

From the variable temperature data from Pss07, no sign of any phase transition was observed between 4.2 and 873.15 K. Figure 6.25 presents the variation of the cell volume with temperature, which varies linearly except at very low temperatures. The slight mismatch between the low temperature data and the data above room temperature is attributed to the slightly different positioning of the sample in the cryostat which cannot be corrected due to the lack of a room temperature measurement in the cryostat.

6.2.3 Electrical characterisation

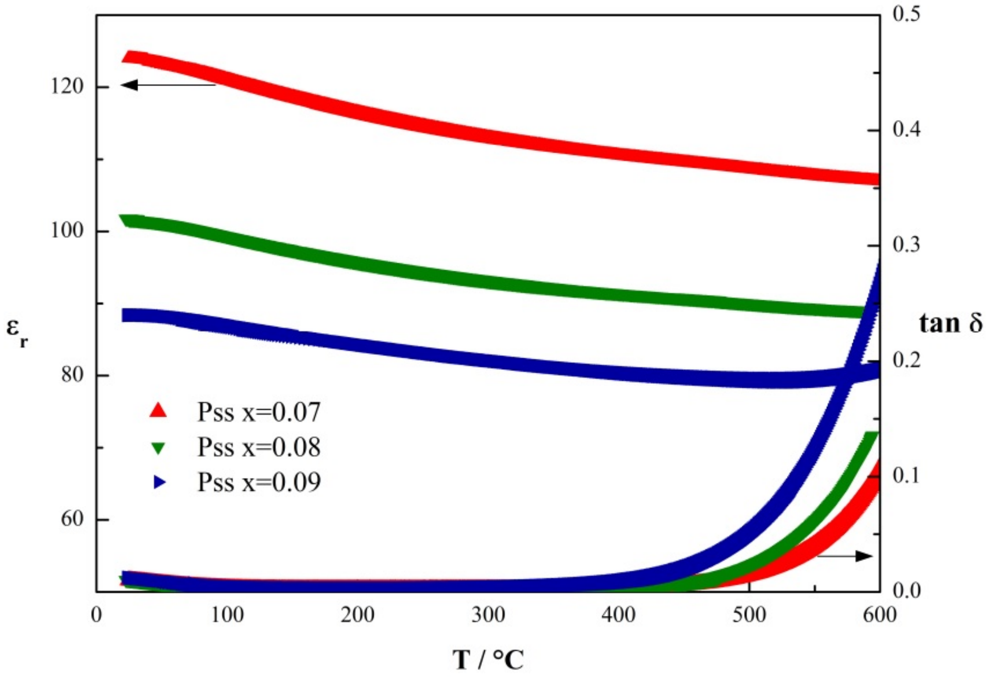

Figure 6.26: Temperature dependence of the relative permittivity and dielectric loss of Pss07, Pss08 and Pss09 at 1 MHz.

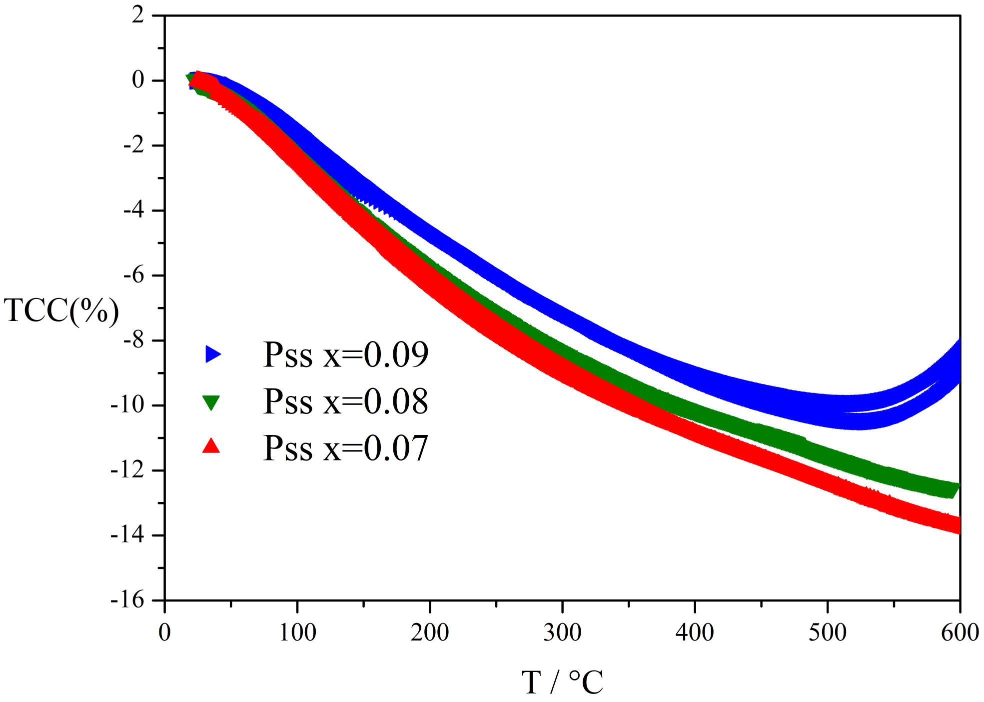

Figure 6.27: Temperature coefficient of the capacitance at 1 MHz for Pss07, Pss08 and Pss09.

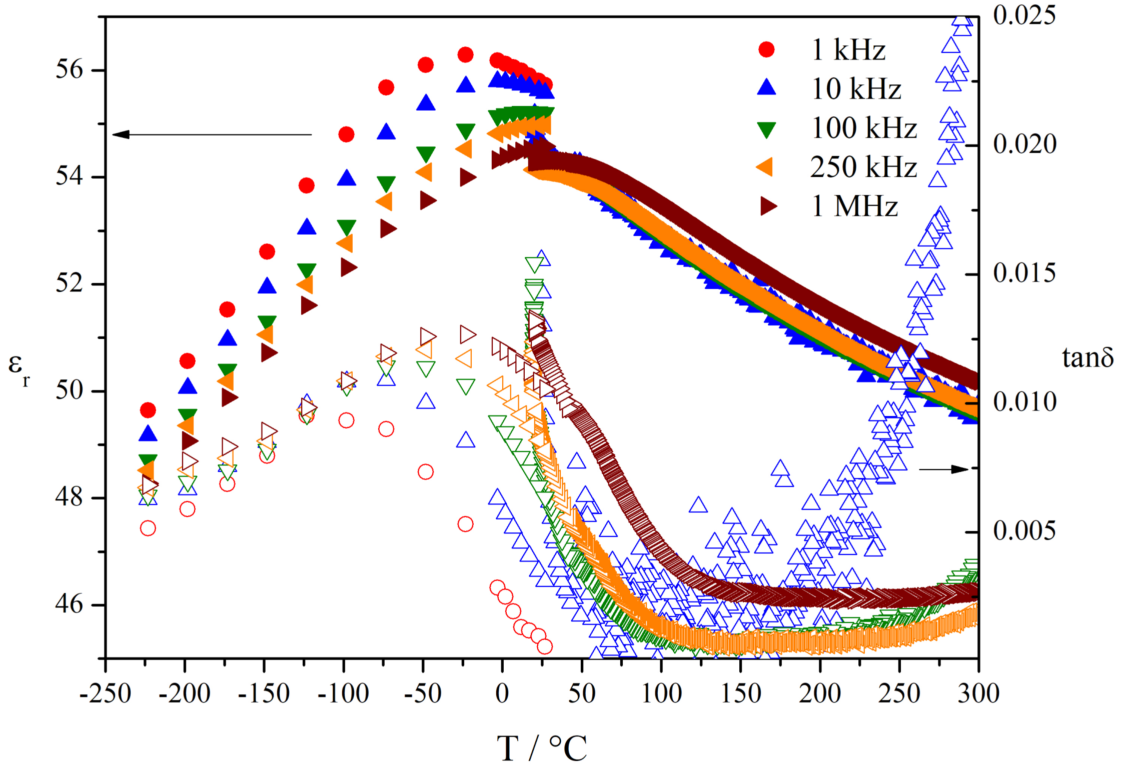

Figure 6.28: Temperature profiles at various frequencies of permittivity (filled symbols) and dielectric loss (open symbols) of a Pss10 pellet sintered at 1100 °C. High temperature data at 1 kHz are excluded for clarity.

Figure 6.26 presents the dielectric measurements from room temperature to 600 °C at 1 MHz on heating and cooling for Pss07, Pss08 and Pss09 sintered on top of NB51T pellets. All exhibit broad permittivity maxima around room temperature with values between 85 and 125. The permittivity drops with increasing Na content, which is to be expected due to the large decrease of bismuth and A-site occupancy in the cell. The dielectric loss increases slightly with the sodium content. Figure 6.27 plots the temperature coefficient of the capacitance defined as the difference (as a percentage) of the permittivity with respect to the value at 25 °C, highlighting the temperature stability of this property in these pyrochlores. It can be appreciated that their permittivities drop by less than 10% up to 400 °C. Figure 6.28 shows the relative permittivity and dielectric loss at various frequencies for a Pss10 pellet sintered at 1100 °C, including low temperature data. It exhibits a broad permittivity maximum of $\sim$ 50 around room temperature. The actual permittivity is expected to be significantly higher (close to 80), but the low density ($\sim$ 75 %) of the measured pellet results in a lower value being measured. The low temperature data show a shift of the maxima in permittivity and dielectric loss to higher temperatures with increasing frequency which indicates relaxor behaviour. It is worthwhile remarking that the dielectric behaviour of the Pss is much more similar to that of ”typical” bismuth pyrochlores than to that reported for $Bi_2Ti_2O_7$, which supports the conclusion from Turner *et al.* about it exhibiting different responses due to the lack of substitutional ions. Although it is noticeable that the ε' and ε'' maxima occur at higher temperatures than the "typical" bismuth pyrochlores.

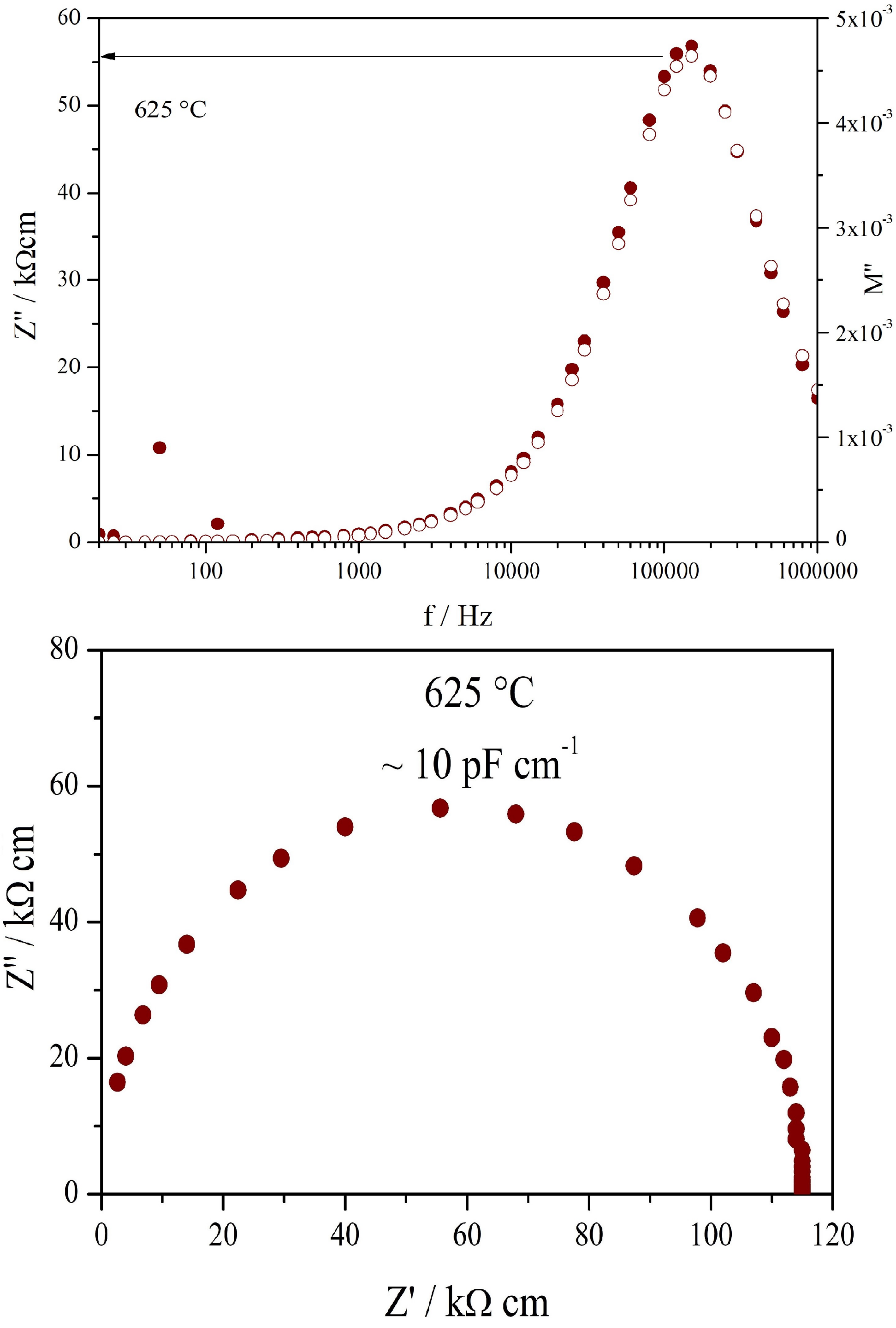

Figure 6.29: Spectroscopic plots of the imaginary components of the impedance and electric modulus (top) and complex impedance plot (bottom) for Pss07 at 625 °C.

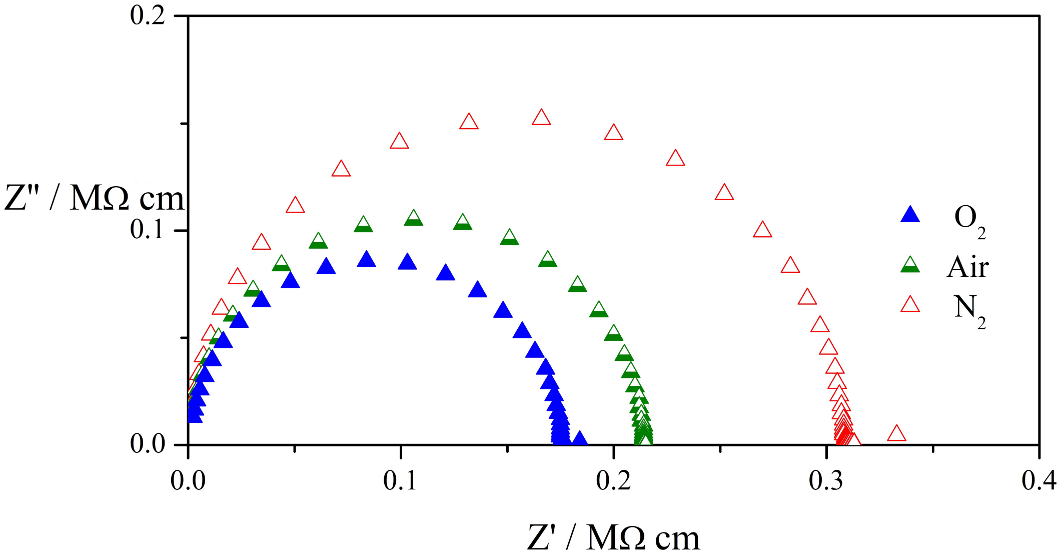

Figure 6.30: Complex impedance plots for Pss07 at 591 °C under O_2, air and N_2.

In Figure 6.29 the impedance spectrum of Pss07 at 625 °C is presented as an example of the data collected. A single response in the Z”, M” and Z* plots is observed in each case which is attributed to the bulk response of the material, based on capacitance values in the order of 10 $\mathrm{pF/cm}$. Figure 6.30 illustrates the p_{O_2} dependence of the impedance for Pss07 at 591 °C, the impedance decreases with increasing p_{O_2} indicating p-type behaviour.

An Arrhenius plot of the bulk conductivities of the Pss is presented in Figure 6.31, including data for a conductive and an insulating NBT for comparison. It can be clearly appreciated that the conductivity of the Pss with an activation energy of $\sim$1.2 to 1.3 eV are comparable to insulating NB51T. Like the dielectric loss, the conductivity slowly increases with sodium content, indicating the increasing loss is dominated by long range conduction. Considering the connectivity of the oxygen sites in the pyrochlore structure, it is thought that vacancies on the 48f sites (those in the BO_6 octahedral network) are essential for efficient long-range migration of the anions [102, 110]. In the case of the $Na_xBi_{1.9\text{-}4.6x}Ti_2O_{6.85\text{-}6.4x}$ pyrochlores in this work, the substitution of Bi by Na most likely means the vacancies occur in the A_2O' chains, so despite the large concentration of vacancies, their mobility is too low to provide high ionic conductivity. Substitutions of the B site ion for larger, more polarisable ions could induce disorder in the anion sublattice pushing the structure towards a defective fluorite, which might provide high oxide ion conductivity. Another option would be to acceptor-dope the B site to introduce vacancies in the octahedral network.

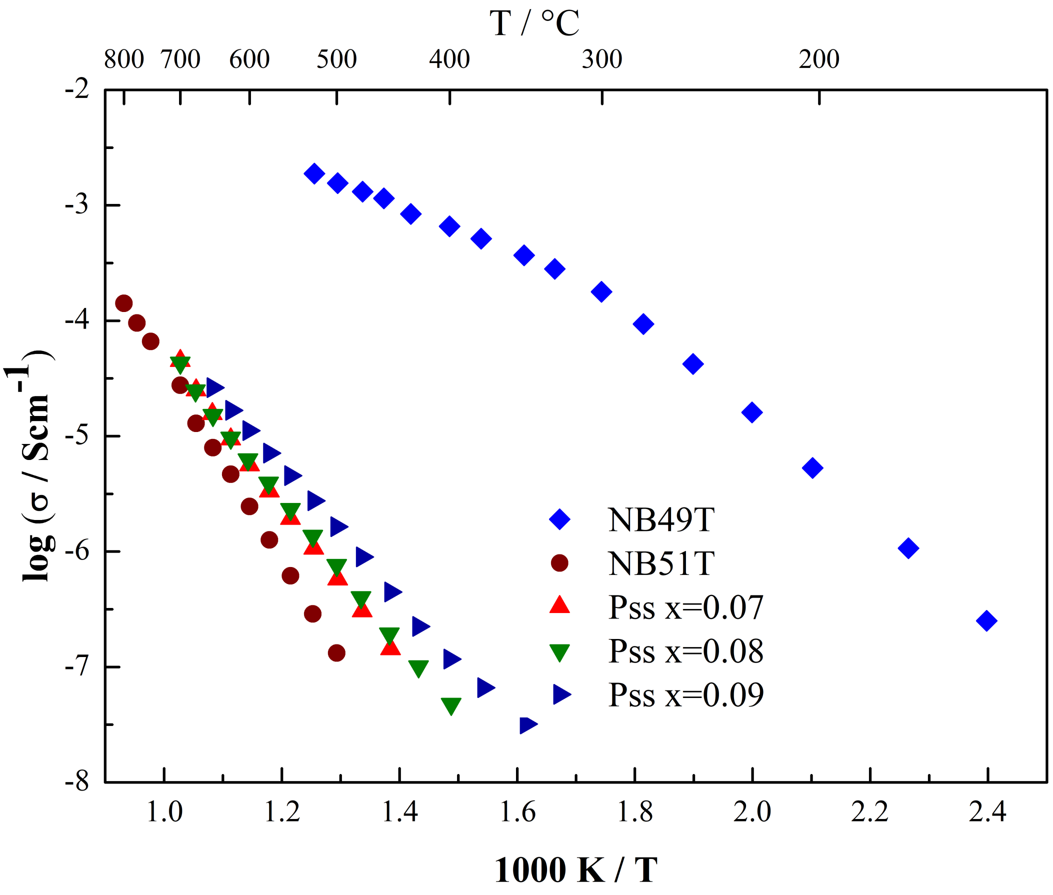

Figure 6.31: Arrhenius plot for the bulk conductivity of Pss. Data from Reference [6] for conductive (NB49T) and insulating (NB51T) NBT are included for comparison.

6.3 Conclusions

The existence of a pyrochlore solid solution in the $Na_2O{\cdot}Bi_2O_3{\cdot}TiO_2$ system has been confirmed as seen in Figure 6.24, although the compositions are different from the originally reported (see Figure 6.9). Similar to the parent phase, these pyrochlores form with A-site vacancies, whose concentration increases quickly with sodium content. Unlike pure ”$Bi_2Ti_2O_7$” the Pss can be prepared through solid state synthesis, however sintering it remains challenging since it can easily decompose through incongruent melting. The peritectic reaction can be taken advantage of to obtain dense ceramics, although the highly reactive liquid introduces a new challenge since it can easily be contaminated (Figure 6.12) by reacting with the crucibles (Al_2O_3 in this work). To avoid this, the Pss can be sintered over NBT. Under high vacuum or slightly reducing atmospheres, these materials can partially reduce turning dark. Figure 6.22 shows that heating a reduced sample under air leads to a small weight gain. The indication that these ceramics are redox-active and their ease of preparation compared to $Bi_2Ti_2O_7$ suggest that a study of their photocatalytic activity should be explored.

These materials exhibit high permittivities with broad maxima around room temperature. These are an expression of the relaxor nature of these solid solutions. In contrast to the bismuth titanate pyrochlore, these sodium containing pyrochlores show dielectric responses like ”traditional” bismuth pyrochlores as exemplified in Figure 6.28, where different frequencies do converge at higher temperatures and at low temperatures the permittivity decreases with increasing frequency; however, they differ in that their maxima for both ε' and ε' occur at noticeable higher temperatures. Bulk conductivities extracted from impedance spectroscopy shown in Figure 6.31 have values comparable to those of insulating NBT. The clear presence of an electronic component and the lack of a low frequency ”spike” suggest that there is negligible oxide ion conduction in these samples; this might be due to the vacancies being concentrated in the A_2O' chains. Having clarified or solved many of the processing issues of these pyrochlores, additional dopants could be attempted to introduce vacancies in the BO_6 octahedral network that may induce oxide ion conduction in these materials.

Chapter 7

Conclusions

There are noticeable differences between the two types of NBT-based solid solutions studied in this work. The solid solutions with high pressure bismuth-based perovskites have solid solution limits below 10% (6∼7% for NBT-BMN and less than 4% for NBT-BZN), while the solid solution with NN can go over 30%. Presumably, higher pressures could help stabilise solid solutions with higher concentrations of bismuth-based perovskites. In all three cases the bulk conductivity decreases with increasing dopant concentration until it is comparable to that of NB51T. The case of NBT-BMN is similar to that of NBT-BA reported in the literature and is consistent with trapping from the acceptor introduced on the B-site as suggested in Reference [14]. In contrast, the more limited solid solution in the NBT-BZN system makes it uncertain if its faster decrease of the ionic conductivity is due to the same effect. Since only the BMN system had a large enough solid solution with NBT to make a comparison against NBT-BA, more systems of this type should be explored to be able to determine if different acceptors impact the ionic conduction in NBT or only their effective charge does. As mentioned in Chapter 4, NBT-$BiZn_{0.5}Ti_{0.5}O_3$ and NBT-$BiMg_{0.5}Ti_{0.5}O_3$ solid solutions are a good option to explore.

The NBT-NN system is insulating by 10% NN, however a small bismuth-deficiency can reintroduce ionic conductivity into the material which decreases with increasing NN content. Perhaps because of the higher solid solution limit, the introduction of NN into NBT affects its polymorphism stabilising to lower temperatures its orthorhombic polymorph.

The bismuth-based perovskites had little effect on the permittivity-temperature profile. On the other hand, for NBT-NN the permittivity becomes lower and much more temperature stable with increasing NN content but this is due to the 1 MHz response having contributions from more than one electroactive element. Other electroactive regions (detected by impedance spectroscopy at higher temperatures) impact the total electrical response, have a strong dependence on processing and p_{O_2} and the bulk itself has such dependence on the processing conditions as to not have easily repeatable electrical properties. Lower NN concentrations should be studied for the stoichiometric system to be able to better compare it against the Bi-based perovskites. It may also be of interest to investigate the conductivity behaviour of NBT solid solutions with other perovskites that have a monovalent A-site ion. It seems that the low solid solution limits of NBT with high pressure Bi-based perovskites may be hindering their use in tuning the properties of NBT. In contrast, those based on perovskites stable at ambient pressure might be more versatile but care must be taken since, at least in the case of NN, dramatic changes in conductivity can occur with small compositional variations.

The cubic Pss studied in Chapter 6 is formed at different compositions from those originally reported by Uchida and Kikuchi. Like ”$Bi_2Ti_2O_7$” it forms with A-site vacancies but the addition of Na_2O stabilises the pyrochlore to lower temperatures allowing it to be obtained through solid state synthesis. The Pss is also difficult to process due to incongruent melting and the potential presence of some redox activity that would mean the solid solution lies on a quaternary phase diagram instead of a ternary, which could account for the different compositions reported here and by Uchida and Kikuchi. Pss exhibit permittivity maxima of $\sim$100 around room temperature and display low electrical conductivity. Although peaks in dielectric loss around room temperature and the difficult processing make it unappealing for applications, it would be of interest to explore introducing mobile vacancies by acceptor doping the B-site, in order to learn if oxide ions in the pyrochlore behave similarly to those in NBT.

Appendices

Appendix A

Rietveld refinements for NBT-BMN and NBT-BZN

Table A.1 presents the progress of the Rietveld refinement for NBT-BMN 2% (using space group Cc) as an example of the refinements performed. Table A.2 shows the refined atomic coordinates for this sample, the quantities without a quoted uncertainty were not refined in the final step . Figure A.1 is a Rietveld plot exemplifying the good agreement between the data collected and the refined model. Finally, Tables A.3 and A.4 present bond lengths observed in the refined models for the NBT-BMN an NBT-BZN solid solutions which are reasonable values and therefore provide confidence in the refinements.

Table A.1: Progress of the Rietveld refinement for NBT-BMN 2%.

Refined	χ^2	wR_p
Background and phase fractions	12.55	0.2014
NBT lattice parameters	10.17	0.1812
Profiles	1.637	0.0726
Atomic positions (A-site only)	1.624	0.0723
Uiso's	1.608	0.0718

Table A.2: Refined atomic coordinates for NBT-BMN 2%. The errors quoted between brackets correspond to 2σ.

	x	y	z
Na^+/Bi^{3+}	0.008(6)	0.250(7)	0.015(5)
$Mg^{2+}/Ti^{4+}/Nb^{5+}$	0.25	0.25	0.75
O^{2-} 1	-0.0024	0.1997	0.4568
O^{2-} 2	0.1985	0.4862	-0.077
O^{2-} 3	0.2586	0.0095	-0.012

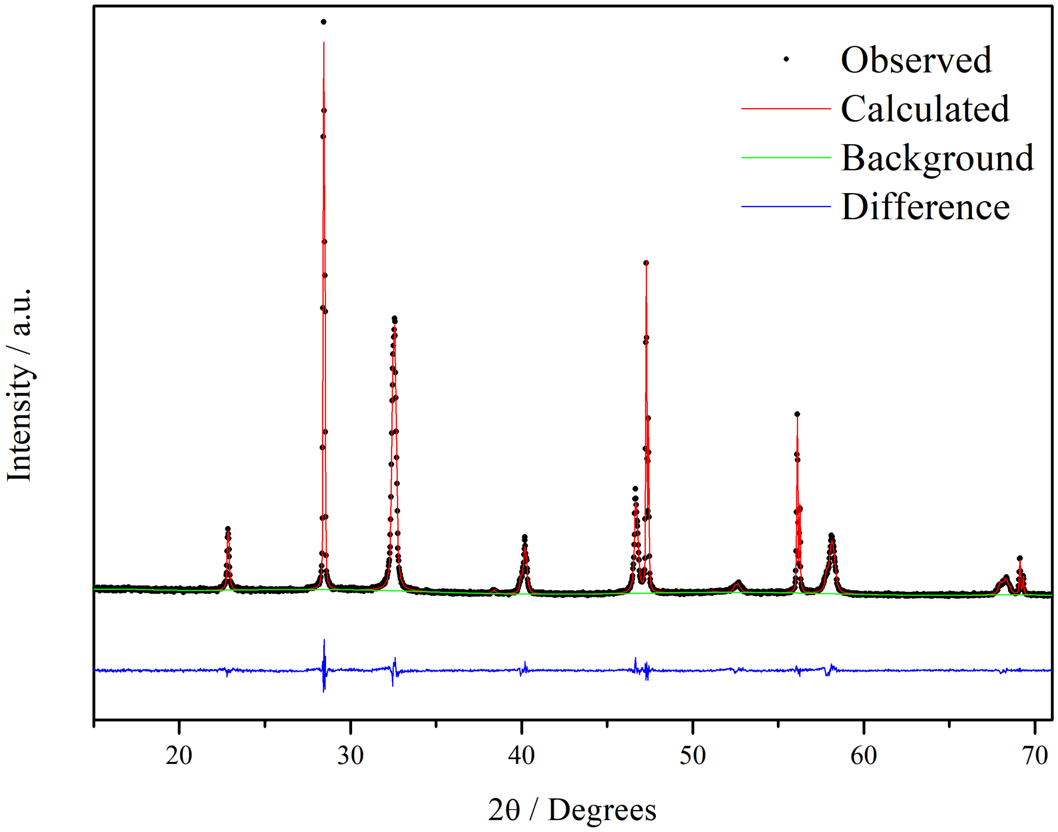

Figure A.1: Rietveld plot for the XRD data refinement of NBT-BMN 2% using space group Cc.

Table A.3: Bond lengths, in Angstroms, from Rietveld refinements of XRD data for NBT-BMN solid solutions using space group Cc. The errors quoted between brackets correspond to 2σ.

NBT-BMN	Bi-O1	Bi-O2	Bi-O3	Ti-O1	Ti-O2	Ti-O3
1%	2.45(4), 2.49(4), 3.04(3), 3.09(3)	2.37(3), 2.54(5), 3.02(5), 3.18(3)	2.67(5), 2.69(3), 2.84(5)	1.9552(4), 1.9945(4)	1.8347(2), 2.1378(2)	1.8294(2), 2.0632(2)
2%	2.48(4), 2.51(4), 3.03(4), 3.04(4)	2.40(3), 2.51(5), 3.05(5), 3.15(3)	2.70(5), 2.71(3), 2.80(5), 2.81(3)	1.9561(5), 1.9952(5)	1.8352(2), 2.1380(3)	1.8297(2), 2.0636(3)
3%	2.5(1) 3.0(1)	2.5(1), 2.6(2), 3.0(2), 3.1(1)	2.6(2), 2.8(1), 2.9(2)	1.956(2), 1.994(1)	1.8372(6), 2.1369(8)	1.8314(7), 2.0657(8)
4%	2.48(4), 2.57(7), 2.98(7), 3.03(4)	2.45(5), 2.49(6), 3.05(6), 3.10(5)	2.70(6), 2.75(4), 2.76(4), 2.80(6)	1.9581(4), 1.959(4)	1.8367(2), 2.1379(2)	1.8302(2), 2.0644(2)
5%	2.48(5), 2.56(1), 3.0(1), 3.03(5)	2.45(7), 2.48(8), 3.07(7), 3.10(6)	2.72(8) 2.75(6), 2.76(3), 2.79(8)	1.959(1), 1.997(1)	1.8374(4), 2.1383(5)	1.8308(4), 2.0650(4)
6%	2.48(3), 2.6(1), 2.9(1), 3.03(3)	2.50(8), 3.03(6), 3.04(8)	2.69(8), 2.82(8)	1.9601(6), 1.9974(6)	1.8383(2), 2.1388(3)	1.8314(2), 2.0657(3)
7%	2.48(4), 2.6(1), 2.9(1), 3.03(4)	2.51(8), 2.5(1), 3.0(1), 3.01(7)	2.7(1), 2.68(8), 2.83(8), 2.9(1)	1.961(1), 1.998(1)	1.8392(4), 2.1394(5)	1.8321(4), 2.0675(4)
8%	2.48(5), 2.6(1), 2.9(1), 3.03(5)	2.5(1), 3.0(1)	2.7(1), 2.84(8), 2.9(1)	1.962(1), 1.999(1)	1.8399(5), 2.1403(6)	1.8328(5), 2.0672(6)

Table A.4: Bond lengths, in Angstroms, from Rietveld refinements of XRD data for NBT-BZN solid solutions using space group Cc. The errors quoted between brackets correspond to 2σ.

NBT-BZN	**Bi-O1**	**Bi-O2**	**Bi-O3**	**Ti-O1**	**Ti-O2**	**Ti-O3**
1%	2.49(5), 2.51(4), 3.03(5), 3.04(3)	2.36(3), 2.47(4), 3.09(4), 3.20(3)	2.67(3), 2.73(4), 2.77(4), 2.85(3)	1.9548(6), 1.9939(6)	1.8347(3), 2.1376(3)	1.8293(3), 2.0632(3)
2%	2.48(4), 2.53(5), 3.01(5), 3.03(4)	2.42(4), 2.51(6), 3.04(6), 3.12(4)	2.68(6), 2.74(4), 2.77(4), 2.81(6)	1.9560(5), 1.9942(5)	1.8354(2), 2.1371(3)	1.8294(2), 2.0634(3)
3%	2.48(3), 2.54(6), 3.00(6), 3.03(3)	2.44(4), 2.52(6), 3.03(6), 3.10(4)	2.68(6), 2.75(4), 2.76(4), 2.82(6)	1.9571(5), 1.9950(5)	1.8360(2), 2.1374(3)	1.8297(2), 2.0638(2)
4%	2.48(5), 2.57(7), 2.98(8), 3.03(5)	2.48(6), 2.53(7), 3.01(7), 3.05(6)	2.66(8), 2.71(6), 2.80(6), 2.84(8)	1.9576(6), 1.9954(6)	1.8368(3), 2.1380(4)	1.8304(3), 2.0646(3)

Appendix B

Metal-oxygen bond strengths in oxides

Bond strengths in most tables of thermochemical data are based entirely on gaseous phase. Rethwisch and Dumesic suggest in Reference [82] (for simple oxides) using the magnitude of the lattice energy (for the "ionic" bond strength) or cohesive energy (for the "neutral" bond strength) of the solid, normalised to one mole of oxygen atoms and divided by the coordination number of oxide ions in the solid. These quantities can be calculated from thermodynamic properties. The cases for aluminium are used as an example. The formation energies of the solids were taken from Reference [111] and other thermodynamic data from Reference [112].

$$\frac{1}{3}\,\mathrm{Al_2O_{3(s)}} \longrightarrow \frac{2}{3}\,\mathrm{Al^{3+}_{(g)}} + \mathrm{O^{2-}_{(g)}} \tag{B.1}$$

$$\frac{1}{3}\,\mathrm{Al_2O_{3(s)}} \longrightarrow \frac{2}{3}\,\mathrm{Al_{(g)}} + \mathrm{O_{(g)}} \tag{B.2}$$

For the ionic bond strength, Equation B.1 is considered. The change of enthalpy will be given by:

$$\begin{aligned}\Delta H_{Al-O}(ionic) = {} & [\Delta H_f(\mathrm{Al_2O}_{3(s)}) - 2\Delta H_{at}(Al_{(s)}) - 3\Delta H_{at}(O_{(g)}) \\ & - 2\Sigma IE(Al_{(g)}) - 3\Sigma\Delta H_{EA}(O_{(g)})]/3\end{aligned} \tag{B.3}$$

where $\Delta H_f(\mathrm{Al_2O}_{3(s)})$ is the formation enthalpy of corundum, $\Delta H_{at}(Al_{(s)})$ and $\Delta H_{at}(O_{(g)})$ the atomisation enthalpies for aluminium and oxygen, respectively; $IE(Al_{(g)})$ are the ionisation energies of aluminium and $\Delta H_{EA}(O_{(g)})$ the changes in enthalpy corresponding to the electron affinities of oxygen. The $\Delta H_{Al-O}(ionic)$ is then divided by the coordination number for oxygen in the solid CN_O (4 in corundum) to obtain the value in Table 4.1. For the "neutral" case of Equation B.2 a similar procedure is followed, excluding the ionisation energies and electron affinities from Equation B.3. Rethwisch and Dumesic state that since bonds are not completely ionic, $\Delta H_{Al-O}(ionic)$ will overestimate the bond strengths, hence the ”neutral” scenarios should also be considered. They note however, at least in the example they provide, that both give the same trend.

Appendix C

Lattice parameters from Rietveld refinements of XRD data for NBT-NN

Tables C.1 and C.2 provide, respectively, examples for the evolution of Rietveld refinements of NBT-NN solid solutions using space groups Cc or $Pnma$. Tables C.3 and C.4 and Figures C.1 and C.2 present the corresponding refined atomic coordinates and Rietveld plots. Bond lengths which again have reasonable values are shown in Tables C.5 and C.6.

Table C.1: Progress of the Rietveld refinement for D05 using space group Cc.

Refined	χ^2	wR_p
Background and phase fractions	54.81	0.4453
NBT lattice parameters	15.05	0.2331
Profiles	9.462	0.1846
Atomic positions (A-site only)	3.924	0.1191
Uiso's	2.826	0.1006

Table C.2: Progress of the Rietveld refinement for D30 using space group $Pnma$.

Refined	χ^2	wR_p
Background and phase fractions	10.45	0.4858
NBT lattice parameters	7.342	0.4070
Profiles	2.473	0.2360
Atomic positions (A-site only)	2.344	0.2296
Uiso's	2.040	0.2139

Table C.3: Refined atomic coordinates for D05 using space group Cc. The errors quoted between brackets correspond to 2σ.

	x	y	z
Na^+/Bi^{3+}	0.030(9)	0.3(2)	0.09(1)
$Mg^{2+}/Ti^{4+}/Nb^{5+}$	0.2703	0.2474	0.8427
O^{2-} 1	0.01(2)	0.23(5)	0.59(4)
O^{2-} 2	0.33(3)	0.50(5)	0.16(7)
O^{2-} 3	0.30(3)	-0.011(8)	0.14(5)

Table C.4: Refined atomic coordinates for D30 using space group Cc. The errors quoted between brackets correspond to 2σ.

	x	y	z
Na^+/Bi^{3+}	0.002(3)	0.25	0.00(1)
$Mg^{2+}/Ti^{4+}/Nb^{5+}$	0.5	0	0
O^{2-} 1	0.07(1)	0.25	0.46(1)
O^{2-} 2	0.73(2)	-0.01(2)	0.27(2)

Table C.5: Bond lengths, in Angstroms, from Rietveld refinements of XRD data for NBT-NN solid solutions using space group Cc. The errors quoted between brackets correspond to 2σ.

	Bi-O1	**Bi-O2**	**Bi-O3**	**Ti-O1**	**Ti-O2**	**Ti-O3**
D05	2.5(1), 2.7(3), 2.9(3), 3.1(1)	2.5(3), 3.1(3)	2.6(7), 2.7(3), 2.9(3), 3.0(3)	1.7(1), 2.3(1)	2.0(3)	1.8(3), 2.1(3)
D10	2.70(5), 2.72(5), 2.87(5), 2.88(4)	2.43(5), 2.44(4), 3.11(4), 3.13(5)	2.49(4), 2.60(5), 2.95(5), 3.05(4)	1.502(1), 2.388(2)	1.8157(4), 2.2125(5)	1.5718(3), 2.3379(5)
D15	2.48(3), 2.58(4), 3.00(4), 3.10(3)	2.480, 2.526, 3.004, 3.041	2.590, 2.591, 2.931, 2.934	1.5884(5), 2.3525(8)	1.910, 2.080	1.704, 2.200
S10	2.55(4), 2.7(2), 2.9(2), 2.97(5)	2.6(1), 2.7(1), 2.84(8), 2.9(1)	2.7(1), 2.75(8), 2.8(1), 2.83(8)	1.6772(8), 2.221(1)	1.7732(2), 2.1801(3)	1.4198(2), 2.4546(3)
R10	2.5(3), 2.7(5), 2.8(5), 3.00(3)	2.4(1), 2.5(1), 3.1(1), 3.2(1)	2.3(4), 2.3(6), 2.9(6), 3.0(3)	1.9(5), 2.0(5)	2.0243(5), 2.0701(4)	1.9(6), 2.0(6)

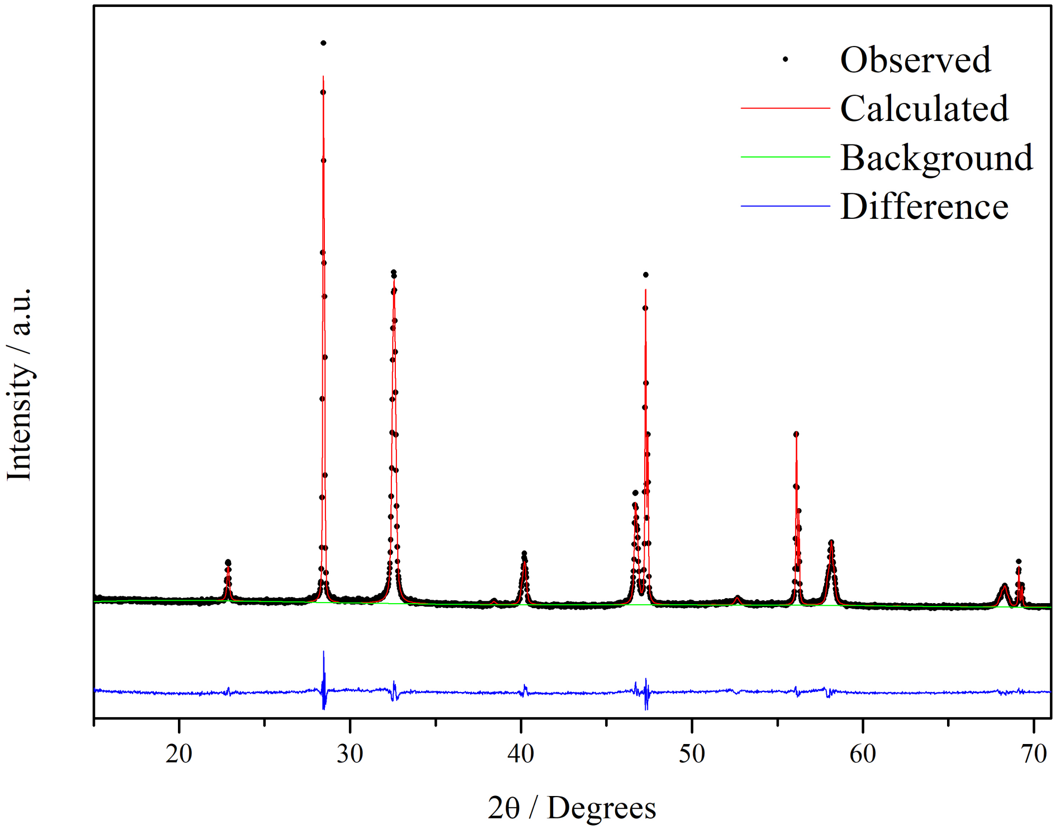

Figure C.1: Rietveld plot for the XRD data refinement of D05 using space group Cc.

Table C.6: Bond lengths, in Angstroms, from Rietveld refinements of XRD data for NBT-NN solid solutions using space group $Pnma$. The errors quoted between brackets correspond to 2σ.

	Bi-O1	**Bi-O2**	**Ti-O1**	**Ti-O2**
D20	2.649(6), 2.665(6), 2.836(7), 2.852(7)	2.632(2), 2.723(3), 2.803(2), 2.854(2)	1.9487(4)	1.931(3), 1.964(3)
D25	2.6(3), 2.66(5), 2.85(5), 2.9(3)	2.68(8), 2.72(8), 2.75(8), 2.86(8)	1.95(1)	1.9419(3), 1.9496(3)
D30	2.40(8), 2.54(8), 3.01(8), 3.12(8)	2.6(1), 2.7(1), 2.8(1), 2.9(1)	2.00(2)	2.00(2)
S20	2.32(3), 2.70(2), 2.87(2), 3.18(3)	2.63(2), 2.80(2), 2.85(2)	1.9955(4)	1.559(1), 2.336(2)
S30	1.86(2), 2.40(2), 3.47(2), 3.80(2)	2.64(2), 2.68(2), 2.81(1), 2.89(1)	2.2975(2)	1.8812(3), 2.0151(2)
R20	2.6(1), 2.7(1), 2.8(1), 2.9(1)	2.49(6), 2.79(6), 2.96(6)	1.947(8)	1.914(3), 2.004(3)
R30	2.64(2), 2.7(1), 2.9(1), 2.87(2)	2.59(6), 2.77(6), 2.82(6), 2.84(6)	1.9509(2)	1.948(2), 1.950(2)

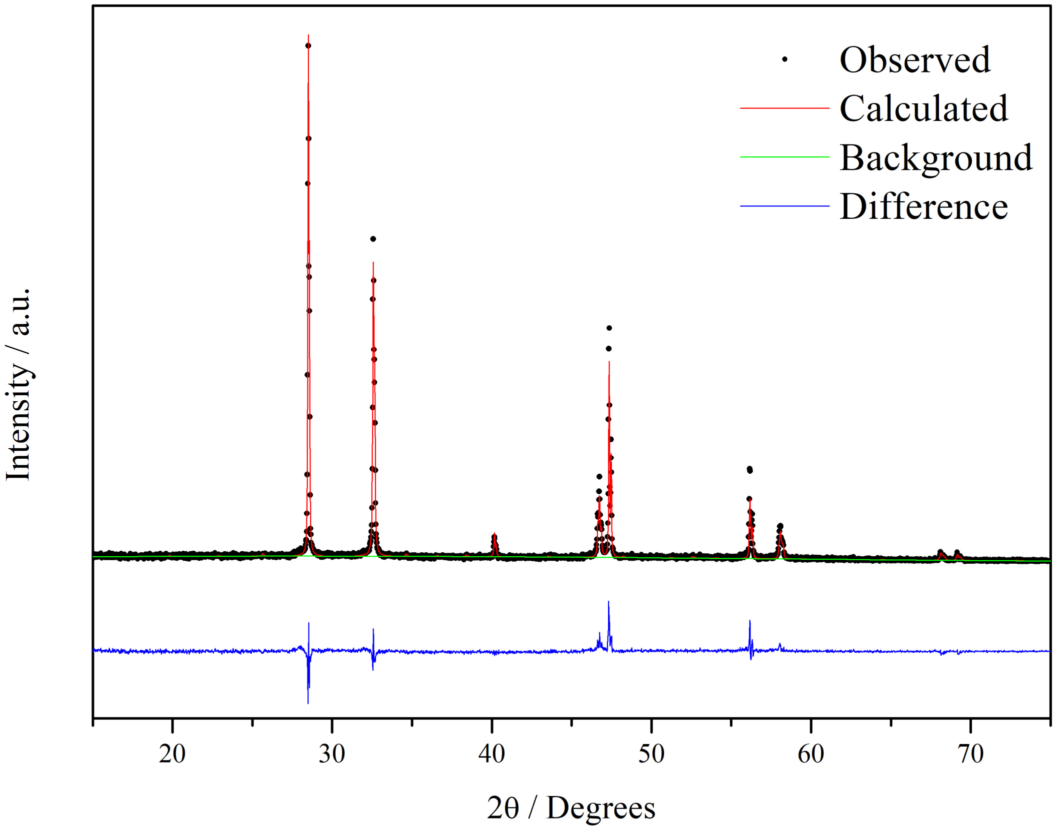

Figure C.2: Rietveld plot for the XRD data refinement of D30 using space group $Pnma$.

Appendix D

Attempt at Rietveld refinement of ND data for NBT-NN

Rietveld refinements of the variable temperature ND data, desirable to extract the fractions of different polymorphs, were unsuccessful. An example is presented here for the room temperature data for D30 attempting a combined refinement using space groups Cc and $Pnma$ of the $90°$ and backscattered detectors and XRD data collected on a STOE STADI-P diffractometer with monochromated Cu $K_{\alpha 1}$ radiation and a linear position sensitive detector. When attempting to refine atomic positions and thermal displacement parameters, achieving convergence becomes difficult if refining both phases simultaneously and the thermal displacement parameters tend towards negative values. Even more worrying is the fact that while the ND pattern from the $90°$ detector seems to have a decent fit, the other ND pattern and the XRD pattern have significant discrepancies in the intensities of the measured data and the predicted patterns as observed in Figure D.1. Figure D.2 compares the difference plots from this refinement to highlight the discrepancies obtained between the different data sets. This difficulty probably arises from the facts that all peaks from the Cc phase overlap with peaks from $Pnma$ and that both the phase fractions and the atomic positions influence the peak intensities.

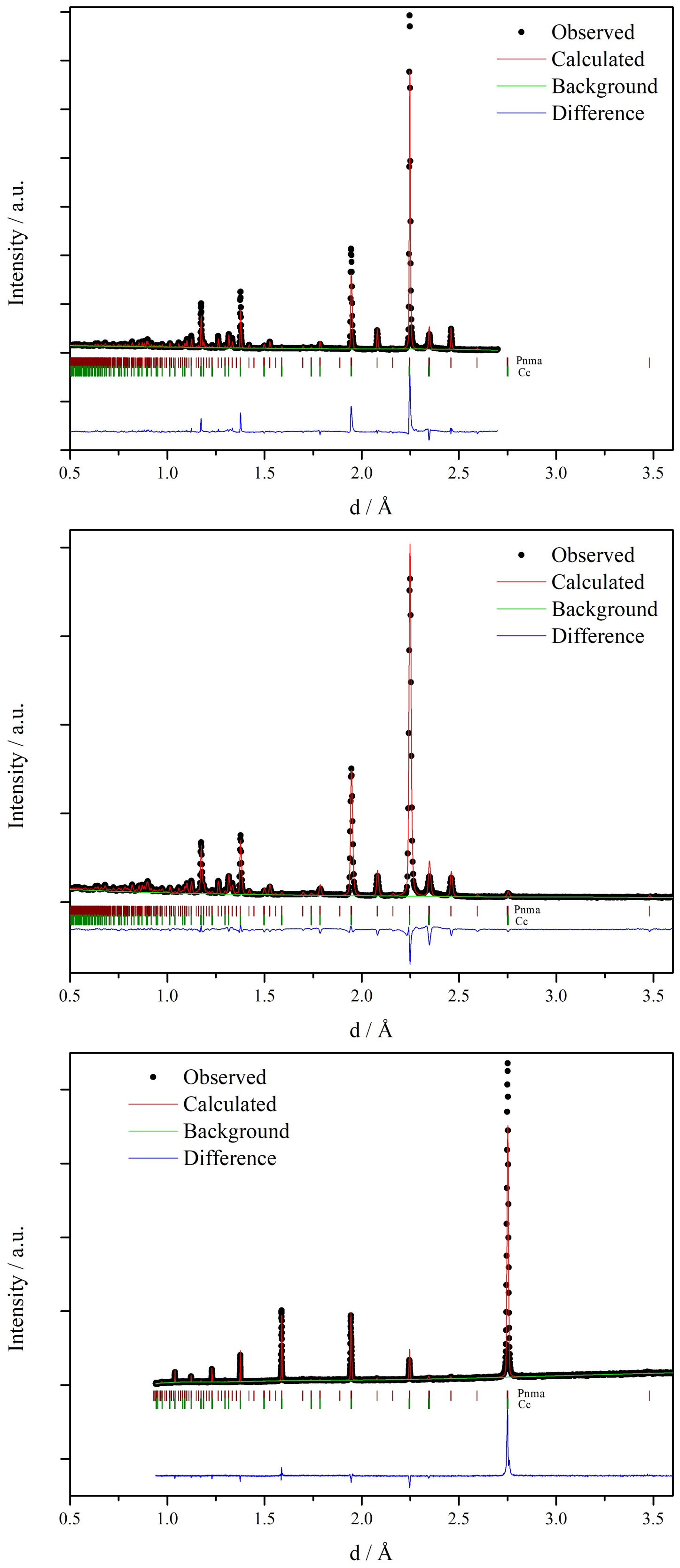

Figure D.1: Rietveld plots for a combined Rietveld refinement for NBT-NN solid solutions using space groups $Pnma$ and Cc, using XRD data and ND data from the 90 ° and backscattered detector on POLARIS.

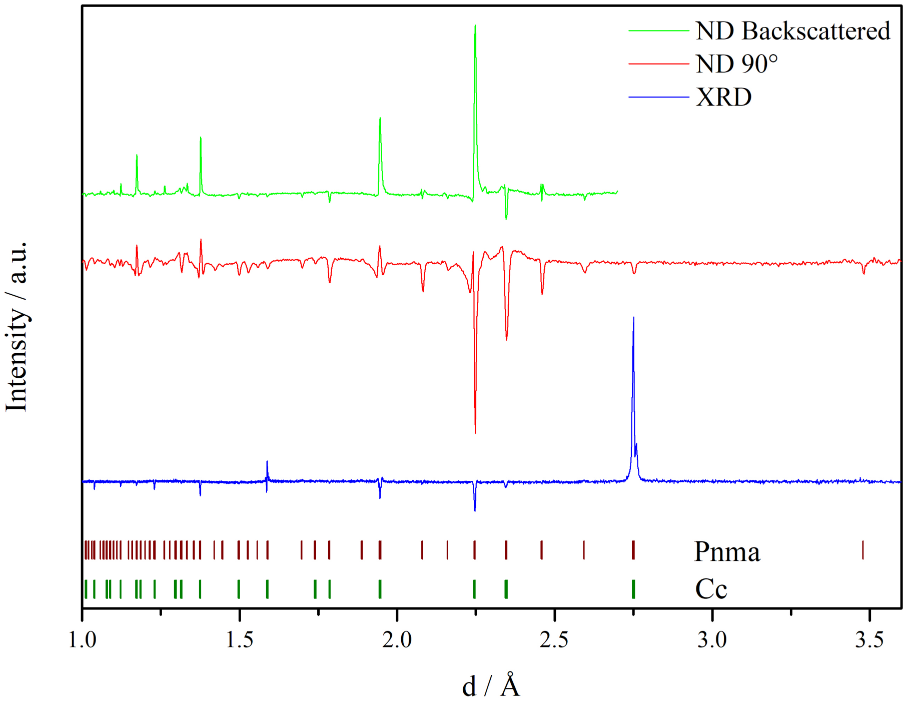

Figure D.2: Normalised difference plots for a combined Rietveld refinement for NBT-NN solid solutions using space groups $Pnma$ and Cc, using XRD data and ND data from the 90 ° and backscattered detector on POLARIS.

Bibliography

[1] S. O. Leontsev and R. E. Eitel, *Progress in engineering high strain lead-free piezoelectric ceramics*, Sci. Technol. Adv. Mater., 2010, **11**, 044302.

[2] J. Rödel, W. Jo, K. T. P. Seifert, E. M. Anton, T. Granzow and D. Damjanovic, *Perspective on the development of lead-free piezoceramics*, J. Am. Ceram. Soc., 2009, **92**, 1153–1177.

[3] A. Zeb and S. J. Milne, *High temperature dielectric ceramics: a review of temperature-stable high-permittivity perovskites*, J. Mater. Sci. Mater. Electron., 2015, **26**, 9243–9255.

[4] G. O. Jones and P. A. Thomas, *Investigation of the structure and phase transitions in the novel A-site substituted distorted perovskite compound* $Na_{0.5}Bi_{0.5}TiO_3$, Acta Crystallogr. Sect. B, 2002, **B58**, 168–178.

[5] I. Levin and I. M. Reaney, *Nano- and Mesoscale Structure of* $Na_{1/2}Bi_{1/2}TiO_3$*: A TEM Perspective*, Adv. Funct. Mater., 2012, **22**, 3445–3452.

[6] M. Li, M. J. Pietrowski, R. A. De Souza, H. Zhang, I. M. Reaney, S. N. Cook, J. A. Kilner and D. C. Sinclair, *A family of oxide ion conductors based on the ferroelectric perovskite* $Na_{0.5}Bi_{0.5}TiO_3$, Nat. Mater., 2014, **13**, 31–5.

[7] F. Yang, M. Li, L. Li, P. Wu, E. Pradal-Velázquez and D. Sinclair, *Review: Defect chemistry and electrical properties of sodium bismuth titanate perovskite*, J. Mater. Chem. A, 2017.

[8] L. Li, *Oxide Ion Conduction in A-site Bi-containing Perovskite-type Ceramics*, Thesis presented for the degree of doctor of philosophy, University of Sheffield, 2016.

[9] F. Yang, M. Li, L. Li, P. Wu, E. Pradal-Velázque and D. C. Sinclair, *Optimisation of oxide-ion conductivity in acceptor-doped* $Na_{0.5}Bi_{0.5}TiO_3$ *perovskite: Approaching the limit?*, J. Mater. Chem. A, 2017, **5**, 21658–21662.

[10] S. S. Sundari, B. Kumar and R. Dhanasekaran, *Synthesis , dielectric and relaxation behavior of lead free NBT−BT ceramics*, Ceram. Int., 2013, **39**, 555–561.

[11] Q. Xu, Z. Song, W. Tang, H. Hao, L. Zhang, M. Appiah, M. Cao, Z. Yao, Z. He and H. Liu, *Ultra-Wide Temperature Stable Dielectrics Based on $Bi_{0.5}Na_{0.5}TiO_3$-$NaNbO_3$ System*, J. Am. Ceram. Soc., 2015, 3119–3126.

[12] E. A. Patterson and D. P. Cann, *Bipolar piezoelectric fatigue of $Bi(Zn_{0.5}Ti_{0.5})O_3-(Bi_{0.5}K_{0.5})TiO_3-(Bi_{0.5}Na_{0.5})TiO_3$ Pb-free ceramics*, Appl. Phys. Lett., 2012, **101**, 042905.

[13] E. A. Patterson and D. P. Cann, *Relaxor to ferroelectric transitions in $(Bi_{1/2}Na_{1/2})TiO_3-Bi(Zn_{1/2}Ti_{1/2})O_3$ solid solutions*, J. Am. Ceram. Soc., 2012, **95**, 3509–3513.

[14] F. Yang, P. Wu and D. C. Sinclair, *Suppression of electrical conductivity and switching of conduction mechanisms in stoichiometric' $(Na_{0.5}Bi_{0.5}TiO_3)_{1-x}(BiAlO_3)_x$ ($0 \leq x \leq 0.08$) solid solutions*, J. Mater. Chem. C, 2017, **5**, 7243–7252.

[15] G. A. Smolenskii, V. A. Isupov, A. I. Agranovskaya and N. N. Krainik, *New ferroelectrics with complex compounds IV*, Fiz. Tverdogo Tela, 1960, **2**, 2982–2985.

[16] R. Mitchell, *Perovskites: Modern and Ancient*, Almaz Press, Ontario, 2002.

[17] V. Dorcet, G. Trolliard and P. Boullay, *Reinvestigation of Phase Transitions in $Na_{0.5}Bi_{0.5}TiO_3$ by TEM . Part I : First Order Rhombohedral to Orthorhombic Phase Transition*, Chem. Mater., 2008, **20**, 5061–5073.

[18] G. Trolliard and V. Dorcet, *Reinvestigation of Phase Transitions in $Na_{0.5}Bi_{0.5}TiO_3$ by TEM. Part II : Second Order Orthorhombic to Tetragonal Phase Transition*, Chem. Mater., 2008, **20**, 5074–5082.

[19] S. Gorfman and P. A. Thomas, *Evidence for a non-rhombohedral average structure in the lead-free piezoelectric material $Na_{0.5}Bi_{0.5}TiO_3$*, J. Appl. Crystallogr., 2010, **43**, 1409–1414.

[20] D. Schütz, M. Deluca, W. Krauss, A. Feteira, T. Jackson and K. Reichmann, *Lone-Pair-Induced Covalency as the Cause of Temperature- and Field-Induced Instabilities in Bismuth Sodium Titanate*, Adv. Funct. Mater., 2012, **22**, 2285–2294.

[21] J. Zang, M. Li, D. C. Sinclair, W. Jo and J. Rödel, *Impedance Spectroscopy of $(Bi_{1/2}Na_{1/2})TiO_3-BaTiO_3$ Ceramics Modified with $(K_{0.5}Na_{0.5})NbO_3$*, J. Am. Ceram. Soc., 2014, **97**, 1523–1529.

[22] S. Bhandari and B. Kumar, *Effect of Structural Modification by MnO_2 Addition on the Electrical Properties of Lead Free Flux Grown $(Na_{0.5}Bi_{0.5})TiO_3-(K_{0.5}Bi_{0.5})TiO_3$ Single Crystals*, Crystal Growth & Design, 2015, **15**, 867–874.

[23] R. A. Cowley, S. N. Gvasaliya, S. G. Lushnikov, B. Roessli and G. M. Rotaru, *Relaxing with relaxors: a review of relaxor ferroelectrics*, Advances in Physics, 2011, **60**, 229–327.

[24] K. Uchida and T. Kikuchi, *Subsolidus Phase Equilibria in the System $Na_2O-Bi_2O_3-TiO_2$ at 1000* °C, J. Am. Ceram. Soc., 1978, **61**, 5–8.

[25] Y. Masuda, H. Masumoto, A. Baba, T. Goto and T. Hirai, *Crystal Growth, Dielectric and Polarization Reversal Properties of $Bi_4Ti_3O_{12}$ Single Crystal*, Jpn. J. Appl. Phys., 1992, **31**, 3108–3112.

[26] Y. F. Kargin, S. N. Ivicheva and V. V. Volkov, *Phase Relations in the $Bi_2O_3-TiO_2$ System*, Russ. J. Inorg. Chem., 2015, **60**, 691–697.

[27] M. Gröting, S. Hayn and K. Albe, *Chemical order and local structure of the lead-free relaxor ferroelectric $Na_{1/2}Bi_{1/2}TiO_3$*, J. Solid State Chem., 2011, **184**, 2041–2046.

[28] T. Ibn-Mohammed, I. M. Reaney, S. C. L. Koh, A. Acquaye, D. C. Sinclair, C. A. Randall, F. H. Abubakar, L. Smith, G. Schileo and L. Ozawa-Meida, *Life cycle assessment and environmental profile evaluation of lead-free piezoelectrics in comparison with lead zirconate titanate*, J. Eur. Ceram. Soc., 2018, **38**, 4922–4938.

[29] S. M. Denkhaus, M. Vögler, N. Novak and J. Rödel, *Short crack fracture toughness in $(1-x)(Na_{1/2}Bi_{1/2})TiO_3-xBaTiO_3$ relaxor ferroelectrics*, J. Am. Ceram. Soc., 2017, **100**, 4760–4769.

[30] W. Jo, S. Schaab, E. Sapper, L. A. Schmitt, H.-J. Kleebe, A. J. Bell and J. Rödel, *On the phase identity and its thermal evolution of lead free $(Bi_{1/2}Na_{1/2})TiO_3$-6 mol% $BaTiO_3$*, J. Appl. Phys., 2011, **110**, 074106.

[31] H. Nagata, *Electrical properties and tracer diffusion of oxygen in some Bi-based lead-free piezoelectric ceramics*, J. Ceram. Soc. Japan, 2008, **116**, 271–277.

[32] Y. S. Sung, J. M. Kim, J. H. Cho, T. K. Song, M. H. Kim and T. G. Park, *Effects of Bi nonstoichiometry in $(Bi_{0.5+x}Na)TiO_3$ ceramics*, Appl. Phys. Lett., 2011, **98**, 012902.

[33] B. Kim, S. Han, J. Kim, J. Lee, B. Ahn and Q. Xu, *Electrical properties of $(1-x)Bi_{0.5}Na_{0.5}TiO_3-xBaTiO_3$ synthesized by emulsion method*, Ceram. Int., 2007, **33**, 447–452.

[34] M. Cernea, B. S. Vasile, C. Capiani, A. Ioncea and C. Galassi, *Dielectric and piezoelectric behaviors of NBT−$BT_{0.05}$ processed by sol-gel method*, J. Eur. Ceram. Soc., 2012, **32**, 133–139.

[35] C. Kim, T. Sekino and K. Niihara, *Synthesis of bismuth sodium titanate nanosized powders by solution sol-gel process*, J. Am. Ceram. Soc., 2003, **86**, 1464–1467.

[36] M. Cernea, E. Andronescu, R. Radu, F. Fochi and C. Galassi, *Sol-gel synthesis and characterization of $BaTiO_3$-doped $(Bi_{0.5}Na_{0.5})TiO_3$ piezoelectric ceramics*, J. Alloys Compd., 2010, **490**, 690–694.

[37] Y. S. Sung, J. M. Kim, J. H. Cho, T. K. Song, M. H. Kim, H. H. Chong, T. G. Park, D. Do and S. S. Kim, *Effects of Na nonstoichiometry in $(Bi_{0.5}Na_{0.5+x})TiO_3$ ceramics*, Appl. Phys. Lett., 2010, **96**, 022901.

[38] Y. Hiruma, H. Nagata and T. Takenaka, *Thermal depoling process and piezoelectric properties of bismuth sodium titanate ceramics*, J. Appl. Phys., 2009, **105**, 084112.

[39] M. Li, H. Zhang, S. N. Cook, L. Li, J. a. Kilner, I. M. Reaney and D. C. Sinclair, *Dramatic Influence of A-Site Nonstoichiometry on the Electrical Conductivity and Conduction Mechanisms in the Perovskite Oxide $Na_{0.5}Bi_{0.5}TiO_3$*, Chem. Mater., 2015, **27**, 629–634.

[40] L. Li, M. Li, H. Zhang, I. M. Reaney and D. C. Sinclair, *Controlling mixed conductivity in $Na_{1/2}Bi_{1/2}TiO_3$ using A-site non-stoichiometry and Nb-donor doping*, J. Mater. Chem. C, 2016, **4**, 5779–5786.

[41] E. Aksel, *Structure and Properties of Sodium Bismuth Titanate*, Thesis presented for the degree of doctor of philosophy, University of Florida, 2012.

[42] X. He and Y. Mo, *Accelerated Materials Design of $Na_{0.5}Bi_{0.5}TiO_3$ Oxygen Ionic Conductors Based on First Principles Calculations*, Phys. Chem. Chem. Phys., 2015, **17**, 18035–18044.

[43] M. Saiful Islam, *Ionic transport in ABO_3 perovskite oxides: a computer modelling tour*, J. Mater. Chem., 2000, **10**, 1027–1038.

[44] R. A. De Souza, *Oxygen Diffusion in SrTiO3 and Related Perovskite Oxides*, Adv. Funct. Mater., 2015, **25**, 6326–6342.

[45] J. W. Fergus, *Electrolytes for solid oxide fuel cells*, J. Power Sources, 2006, **162**, 30–40.

[46] R. A. Maier, C. A. Randall and J. Stevenson, *Low-Temperature Ionic Conductivity of an Acceptor-Doped Perovskite: I. Impedance of Single-Crystal SrTiO3*, J. Am. Ceram. Soc., 2016, **99**, 3350–3359.

[47] C. Haavik, E. M. Ottesen, K. Nomura, J. A. Kilner and T. Norby, *Temperature dependence of oxygen ion transport in Sr+Mg-substituted LaGaO3 (LSGM) with varying grain sizes*, Solid State Ionics, 2004, **174**, 233–243.

[48] A. Bogicevic and C. Wolverton, *Nature and strength of defect interactions in cubic stabilized zirconia*, Phys. Rev. B, 2003, **67**, 024106.

[49] S. T. Norberg, S. Hull, I. Ahmed, S. G. Eriksson, D. Marrocchelli, P. A. Madden, P. Li and J. T. S. Irvine, *Structural Disorder in Doped Zirconias, Part I: The Zr0.8Sc0.2-xYx O1.9 (0.0 x 0.2) System*, Chem. Mater., 2011, **23**, 1356–1364.

[50] D. Marrocchelli, P. A. Madden, S. T. Norberg and S. Hull, *Structural disorder in doped zirconias, part II: Vacancy ordering effects and the conductivity maximum*, Chem. Mater., 2011, **23**, 1365–1373.

[51] M. S. Islam and R. A. Davies, *Atomistic study of dopant site-selectivity and defect association in the lanthanum gallate perovskite*, J. Mater. Chem., 2004, **14**, 86–93.

[52] F. Yang, H. Zhang, L. Li, I. M. Reaney and D. C. Sinclair, *High Ionic Conductivity with Low Degradation in A-Site Strontium-Doped Nonstoichiometric Sodium Bismuth Titanate Perovskite*, Chem. Mater., 2016, **28**, 5269–5273.

[53] K.-C. Meyer and K. Albe, *Influence of phase transitions and defect associates on the oxygen migration in the ion conductor* $Na_{1/2}Bi_{1/2}TiO_3$, J. Mater. Chem. A, 2017, **5**, 4368–4375.

[54] L. Koch, S. Steiner, K.-C. Meyer, I.-T. Seo, K. Albe and T. Frömling, *Ionic conductivity of acceptor doped sodium bismuth titanate: influence of dopants, phase transitions and defect associates*, J. Mater. Chem. C, 2017, **5**, 8958–8965.

[55] Z. Gao, L. V. Mogni, E. C. Miller, J. G. Railsback and S. A. Barnett, *A Perspective On Low-Temperature Solid Oxide Fuel Cells*, Energy Environ. Sci., 2016.

[56] Y. Lu, C. A. López, J. Wang, J. A. Alonso and C. Sun, *Insight into the structure and functional application of Mg-doped* $Na_{0}\cdot{}_{5}Bi_{0}\cdot{}_{5}TiO_{3}$ *electrolyte for solid oxide fuel cells*, J. Alloys Compd., 2018, **752**, 213–219.

[57] W. H. Bragg and W. L. Bragg, *The Reflection of X-rays by Crystals*, Proc. R. Soc. A Math. Phys. Eng. Sci., 1913, **88**, 428–438.

[58] H. M. Rietveld, *Line profiles of neutron powder-diffraction peaks for structure refinement*, Acta Crystallogr., 1967, **22**, 151–152.

[59] H. M. Rietveld, *A profile refinement method for nuclear and magnetic structures*, J. Appl. Crystallogr., 1969, **2**, 65–71.

[60] B. H. Toby, *R factors in Rietveld analysis : How good is good enough ?*, Powder Diffr., 2006, **21**, 67–70.

[61] L. B. McCusker, R. B. Von Dreele, D. E. Cox, D. Louër and P. Scardi, *Rietveld refinement guidelines*, J. Appl. Crystallogr., 1999, **32**, 36–50.

[62] A. C. Larson and R. B. Von Dreele, *General Structure Analysis System (GSAS)*, Los Alamos National Laboratory Report LAUR 86-748, 2000.

[63] B. H. Toby, *EXPGUI, a graphical user interface for GSAS*, J. Appl. Cryst., 2001, **34**, 210–213.

[64] E. Aksel, J. S. Forrester, J. L. Jones, P. A. Thomas, K. Page and M. R. Suchomel, *Monoclinic crystal structure of polycrystalline* $Na_{0.5}Bi_{0.5}TiO_3$, Applied Physics Letters, 2011, **98**, 152901.

[65] P. A. Thomas, J. Kreisel, M. A. Glazer, P. Bouvier, Q. Jiang and R. Smith, *The high-pressure structural phase transitions of sodium bismuth titanate*, Zeitschrift fr Kristallographie - Crystalline Materials, 2009, **220**, 717–725.

[66] J. T. S. Irvine, D. C. Sinclair and A. R. West, *Electroceramics: Characterization by Impedance Spectroscopy*, Adv. Mater., 1990, **2**, 132–138.

[67] A. West, *Solid State Chemistry and its Applications*, Wiley, UK, 2014.

[68] L. R. F.R.S., *XXXI. Investigations in optics, with special reference to the spectroscope*, The London, Edinburgh, and Dublin Philosophical Magazine and Journal of Science, 1879, **8**, 261–274.

[69] J. Goldstein, D. Newbury, J. Michael, N. Ritchie, J. Scott and D. Joy, *Scanning Electron Microscopy and X-Ray Microanalysis*, Springer New York, 2017.

[70] A. A. Belik, T. Wuernisha, T. Kamiyama, K. Mori, M. Male, T. Nagai, Y. Matsui and E. Takayama-Muromachi, *High-pressure synthesis, crystal structures, and properties of perovskite-like* $BiAlO_3$ *and pyroxene-like* $BiGaO_3$, Chem. Mater., 2006, **18**, 133–139.

[71] A. A. Belik, T. Yokosawa, K. Kimoto, Y. Matsui and E. Takayama-Muromachi, *High-Pressure Synthesis and Properties of Solid Solutions between $BiMnO_3$ and $BiScO_3$*, Chem. Mater., 2007, **19**, 1679–1689.

[72] Y. Inaguma, A. Miyaguchi, M. Yoshida, T. Katsumata, Y. Shimojo, R. Wang and T. Sekiya, *High-pressure synthesis and ferroelectric properties in perovskite-type $BiScO_3$-$PbTiO_3$ solid solution*, J. Appl. Phys., 2004, **95**, 231–235.

[73] A. V. Pushkarev, N. M. Olekhnovich and Y. V. Radyush, *High-pressure $Bi(Mg_{1x}Zn_x)_{1/2}Ti_{1/2}O_3$ perovskite solid solutions*, Inorg. Mater., 2011, **47**, 1116–1119.

[74] I. Levin, V. Krayzman, J. C. Woicik, F. Bridges, G. E. Sterbinsky, T. M. Usher, J. L. Jones and D. Torrejon, *Local structure in $BaTiO_3-BiScO_3$ dipole glasses*, Phys. Rev. B, 2016, **93**, 1–12.

[75] N. Kumar and D. P. Cann, *Tailoring transport properties through nonstoichiometry in $BaTiO_3BiScO_3$ and $SrTiO_3Bi(Zn_{1/2}Ti_{1/2})O_3$ for capacitor applications*, J. Mater. Sci., 2016, **51**, 9404–9414.

[76] R. E. Eitel, C. A. Randall, T. R. Shrout, P. W. Rehrig, W. Hackenberger and S.-E. Park, *New High Temperature Morphotropic Phase Boundary Piezoelectrics Based on $Bi(Me)O_3PbTiO_3$ Ceramics*, Jpn. J. Appl. Phys., 2001, **40**, 5999–6002.

[77] Y. V. Radyush, N. M. Olekhnovich and A. V. Pushkarev, *Crystal structure and dielectric properties of $(1x)KNbO_3{\cdot}xBiMg_{2/3}Nb_{1/3}O_3$ perovskite solid solutions*, Inorg. Mater., 2009, **45**, 1053–1057.

[78] H. Nagata, T. Takenaka, I. Ueda and S. Ikegami, *Lead-Free Piezoelectric Ceramics of $(Bi_{1/2}Na_{1/2})TiO_3$-$1/2(Bi_2O_3{\cdot}Sc_2O_3)$ System*, Jpn. J. Appl. Phys., 1997, **36**, 6055–6057.

[79] H. Yu and Z.-G. Ye, *Dielectric, ferroelectric, and piezoelectric properties of the lead-free $(1x)(Na_{0.5}Bi_{0.5}TiO_3-xBiAlO_3$ solid solution*, Appl. Phys. Lett., 2008, **93**, 112902.

[80] R. D. Shannon, *Revised Effective Ionic Radii and Systematic Studies of Interatomic Distances in Halides and Chaleogenides*, Acta Crystallogr., 1976, **A 32**, 751.

[81] A. Bogicevic, C. Wolverton, G. M. Crosbie and E. B. Stechel, *Defect ordering in aliovalently doped cubic zirconia from first principles*, Phys. Rev. B, 2001, **64**, 014106.

[82] D. G. Rethwisch and J. A. Dumesic, *Effect of MetalOxygen Bond Strength on Properties of Oxides. 1. Infrared Spectroscopy of Adsorbed CO and CO2*, Langmuir, 1986, **2**, 73–79.

[83] A. Urban, A. Abdellahi, S. Dacek, N. Artrith and G. Ceder, *Electronic-Structure Origin of Cation Disorder in Transition-Metal Oxides*, Phys. Rev. Lett., 2017, **119**, 1–6.

[84] M. Subramanian, G. Aravamudan and G. Subba Rao, *Oxide pyrochlores A review*, Prog. Solid State Chem., 1983, **15**, 55–143.

[85] J. Koruza, P. Groszewicz, H. Breitzke, G. Buntkowsky, T. Rojac and B. Malič, *Grain-size-induced ferroelectricity in* $NaNbO_3$, Acta Mater., 2017, **126**, 77–85.

[86] K. E. Johnston, J. M. Griffin, R. I. Walton, D. M. Dawson, P. Lightfoot and S. E. Ashbrook, *^{93}Nb NMR and DFT investigation of the polymorphs of* $NaNbO_3$, Phys. Chem. Chem. Phys., 2011, **13**, 7565–7576.

[87] M. D. Peel, S. P. Thompson, A. Daoud-Aladine, S. E. Ashbrook and P. Lightfoot, *New Twists on the Perovskite Theme: Crystal Structures of the Elusive Phases R and S of* $NaNbO_3$, Inorg. Chem., 2012, **51**, 6876–6889.

[88] Y. Shiratori, A. Magrez, J. Dornseiffer, F.-H. Haegel, C. Pithan and R. Waser, *Polymorphism in Micro-, Submicro-, and Nanocrystalline* $NaNbO_3$, J. Phys. Chem. B, 2005, **109**, 20122–20130.

[89] M. Tyunina, A. Dejneka, D. Rytz, I. Gregora, F. Borodavka, M. Vondracek and J. Honolka, *Ferroelectricity in antiferroelectric* $NaNbO_3$, J. Phys. Condens. Matter, 2014, **26**, 125901.

[90] R. T. George, D. C. Joshi, S. Nayak, N. Tiwari, R. N. Chauhan, P. Pramanik, T. A. Dar, S. Ghosh and S. Thota, *Effect of NiO substitution on the structural and dielectric behaviour of* $NaNbO_3$, J. Appl. Phys., 2018, **123**, 054101.

[91] L. Chao, Y. Hou, M. Zheng, Y. Yue and M. Zhu, $NaNbO_3$ *nanoparticles: Rapid mechanochemical synthesis and high densification behavior*, J. Alloys Compd., 2017, **695**, 3331–3338.

[92] H. Guo, H. Shimizu and C. A. Randall, *Direct evidence of an incommensurate phase in* $NaNbO_3$ *and its implication in* $NaNbO_3$*-based lead-free antiferroelectrics*, Appl. Phys. Lett., 2015, **107**, 112904.

[93] H. Ge, Y. Hou, C. Xia, M. Zhu, H. Wang and H. Yan, *Preparation and Piezoelectricity of* $NaNbO_3$ *High-Density Ceramics by Molten Salt Synthesis*, J. Am. Ceram. Soc., 2011, **94**, 4329–4334.

[94] J. Koruza and B. Malič, *Initial stage sintering mechanism of* $NaNbO_3$ *and implications regarding the densification of alkaline niobates*, J. Eur. Ceram. Soc., 2014, **34**, 1971–1979.

[95] T. Takenaka, T. Okuda and K. Takegahara, *Lead-free piezoelectric ceramics based on* $(Bi_{1/2}Na_{1/2})TiO_3{-}NaNbO_3$, Ferroelectrics, 1997, **196**, 175–178.

[96] T. Wada, K. Toyoike, Y. Imanaka and Y. Matsuo, *Dielectric and Piezoelectric Properties of* $(A_{0.5}Bi_{0.5})TiO_3ANbO_3$ *(A=Na, K) Systems*, Jpn. J. Appl. Phys., 2001, **40**, 5703 – 5705.

[97] Q. Xu, T. Li, H. Hao, S. Zhang, Z. Wang, M. Cao, Z. Yao and H. Liu, *Enhanced energy storage properties of NaNbO3 modified Bi0.5Na0.5TiO3 based ceramics*, J. Eur. Ceram. Soc., 2015, **35**, 545–553.

[98] T. Jardiel, A. C. Caballero and M. Villegas, *Aurivillius ceramics:* $Bi_4Ti_3O_{12}$*-based piezoelectrics*, J. Ceram. Soc. Japan, 2008, **116**, 511–518.

[99] A. Yokoi and J. Sugishita, *Ferroelectric properties of mixed bismuth layer-structured* $Na_{0.5}Bi_{8.5}Ti_7O_{27}$ *ceramic and* $Sr_xNa_{0.5\text{-}x/2}Bi_{8.5\text{-}x/2}Ti_7O_{27}$ *solid solutions*, J. Alloys Compd., 2008, **452**, 467–472.

[100] V. Kahlenberg and H. Böhm, *The structures of* α *and* β $Bi_2Ti_4O_{11}$, Acta Crystallogr. Sect. B, 1995, **B51**, 11–18.

[101] G. Laurita, J. Vielma, F. Winter, R. Berthelot, A. Largeteau, R. Pöttgen, G. Schneider and M. A. Subramanian, *From* $Ag_2Sb_2O_6$ *to* $Cd_2Sb_2O_7$*: Investigations on an anion-deficient to ideal pyrochlore solid solution*, J. Solid State Chem., 2014, **210**, 65–73.

[102] P. J. Wilde and C. R. A. Catlow, *Defects and diffusion in pyrochlore structured oxides*, Solid State Ionics, 1998, **112**, 173–183.

[103] D. P. Cann, C. A. Randall and T. R. Shrout, *Investigation of the dielectric properties of bismuth pyrochlores*, Solid State Commun., 1996, **100**, 529–534.

[104] O. Merka, D. W. Bahnemann and M. Wark, *Photocatalytic hydrogen production with non-stoichiometric pyrochlore bismuth titanate*, Catal. Today, 2014, **225**, 102–110.

[105] J. R. Esquivel-Elizondo, B. B. Hinojosa and J. C. Nino, $Bi_2Ti_2O_7$ *: It Is Not What You Have Read*, Chem. Mater., 2011, **23**, 4965–4974.

[106] I. Radosavljevic, J. Evans and A. Sleight, *Synthesis and Structure of Pyrochlore-Type Bismuth Titanate*, J. Solid State Chem., 1998, **136**, 63–66.

[107] S. S. Kim, M. H. Park, J. K. Chung and W. J. Kim, *Structural study of a sol-gel derived pyrochlore* $Bi_2Ti_2O_7$ *using a Rietveld analysis method based on neutron scattering studies*, J. Appl. Phys., 2009, **105**, 8–13.

[108] I. V. Piir, M. S. Koroleva, Y. I. Ryabkov, D. A. Korolev, N. V. Chezhina, V. G. Semenov and V. V. Panchuk, *Bismuth iron titanate pyrochlores: Thermostability, structure and properties*, J. Solid State Chem., 2013, **204**, 245–250.

[109] C. G. Turner, J. R. Esquivel-Elizondo and J. C. Nino, *Dielectric properties and relaxation of* $Bi_2Ti_2O_7$, J. Am. Ceram. Soc., 2014, **97**, 1763–1768.

[110] B. J. Wuensch, K. W. Eberman, C. Heremans, E. M. Ku, P. Onnerud, E. M. E. Yeo, S. M. Haile, J. K. Stalick and J. D. Jorgensen, *Connection between oxygen-ion conductivity of pyrochlore fuel-cell materials and structural change with composition and temperature*, Solid State Ionics, 2000, **129**, 111–133.

[111] J. Dean and N. Lange, *Lange's Handbook of chemistry*, fifteenth edition, McGraw-Hill, 1999.

[112] C. Housecroft and A. Sharpe, *Inorganic Chemistry*, second edition, Pearson Prentice Hall, 2005.

Some images were generated using CrystalMaker®: a crystal and molecular modelling program for Mac and Windows. CrystalMaker Software Ltd, Oxford, UK (www.crystalmaker.com).